DISSERTATION

POST-FIRE IMPACTS ON MICROCLIMATE AND CONVECTIVE PRECIPITATION

Submitted by

Elizabeth Mulvihill Page

Department of Atmospheric Science

In partial fulfillment of the requirements

For the Degree of Doctor of Philosophy

Colorado State University

Fort Collins, CO 80523

Spring 2007

Reproduced with permission of the copyright owner. Further reproduction prohibited without permission.

UMI Number: 3266344

INFORMATION TO USERS

The quality of this reproduction is dependent upon the quality of the copy submitted. Broken or indistinct print, colored or poor quality illustrations and photographs, print bleed-through, substandard margins, and improper alignment can adversely affect reproduction.

In the unlikely event that the author did not send a complete manuscript and there are missing pages, these will be noted. Also, if unauthorized copyright material had to be removed, a note will indicate the deletion.

UMI®

UMI Microform 3266344

Copyright 2007 by ProQuest Information and Learning Company.

All rights reserved. This microform edition is protected against unauthorized copying under Title 17, United States Code.

ProQuest Information and Learning Company
300 North Zeeb Road
P.O. Box 1346
Ann Arbor, MI 48106-1346

Reproduced with permission of the copyright owner. Further reproduction prohibited without permission.

COLORADO STATE UNIVERSITY

March, 20 2007

WE HEREBY RECOMMEND THAT THE DISSERTATION PREPARED UNDER OUR SUPERVISION BY ELIZABETH MULVIHILL PAGE ENTITLED POST-FIRE IMPACTS ON MICROCLIMATE AND CONVECTIVE PRECIPITATION BE ACCEPTED AS FULFILLING INPART REQUIREMENTS FOR THE DEGREE OF DOCTOR OF PHILOSOPHY.

Committee on Graduate Work

Dr. Roger A. Pielke, Sr.

Dr. A. Scott Denning

Dr. Paul W. Mielke, Jr.

Dr. William R. Cotton, **Adviser**

Dr. Richard H. Johnson, **Department Head**

Reproduced with permission of the copyright owner. Further reproduction prohibited without permission.

ABSTRACT OF DISSERTATION

POST-FIRE IMPACTS ON MICROCLIMATE AND CONVECTIVE PRECIPITATION

Changes in the landscape by fire have been measured and documented during several field projects. In this study the effects of landscape changes on the microclimate of a burn scar are examined and the potential changes in precipitation amount and microphysical characteristics of storms over and near the burn area are investigated.

The Colorado State University Regional Atmospheric Modeling System was used to simulate the physical processes at work in the burn scar environment. The model was initialized with an atmospheric sounding from a flash flood event to investigate the effects of the burn scar on the development of precipitation in an atmosphere associated with the development of heavy precipitation. Burn scar regions are more vulnerable to flooding and erosion, and a major goal of this study is to explore whether these already flood-susceptible regions are also regions of enhanced precipitation, therefore increasing the potential for flooding over the burn scar.

The results show that the burn scar significantly affected both the microclimate of the environment and the amount of precipitation produced by convection over the burn scar. The increased sensible heat flux and temperatures over the burn scar resulted in convective development and cloud formation. Effects were also seen in externally forced convection in stronger updrafts and greater precipitation. Microphysical changes in the forced convective clouds showed increased number concentration of graupel thus

Reproduced with permission of the copyright owner. Further reproduction prohibited without permission.

implying greater electrification of these clouds. Sensitivity tests revealed some effects of soil moisture changes in the burn scar while distinct differences were seen with a stronger initialization wind field.

The findings of this study suggest that burn scar regions are not only more susceptible to flooding due to increased runoff with changes in surface characteristics, but may also be preferred regions of convective development, increased precipitation, and greater lightning activity.

Elizabeth Mulvihill Page
Department of Atmospheric Science
Colorado State University
Fort Collins, CO 80523
Spring 2007

Reproduced with permission of the copyright owner. Further reproduction prohibited without permission.

ACKNOWLEDGEMENTS

I thank my committee for their support throughout my time in this program. My adviser, Prof. Bill Cotton helped me develop my research topic and provided his unique form of encouragement to inspire me. My other committee members, Prof. Roger Pielke, Prof. Scott Denning, Prof. Tom McKee, and Prof. Paul Mielke are thanked for their contributions to my research efforts.

My coursework was supported by NOAA's National Weather Service, initially as part of their University Assignment Program, and later as professional development activities. I thank my supervisor during that time, LeRoy Spayd, for his encouragement and flexibility as I adjusted my schedule to accommodate classes. I am also grateful to Dr. Tim Spangler and Dr. Greg Byrd with the COMET Program for their words of encouragement. I thank Matt Kelsch of COMET for providing suggestions and background information for the flood case used to initialize the model runs, and Chris Rozoff for his help in defining a new LEAF-2 class. I also thank Brenda Thompson for her help in assembling this manuscript and organizing my committee meetings, and Jen Weingardt for helping me work with the graduate school.

My friends have helped me rise to the many challenges of this program and overcome obstacles. I thank Dr. Tracy Clement, Dr. Mari Ochiai Holcomb, and Prof. Phil DeLeon for sharing their own graduate experiences with me. Susan Jesuroga coached me through the hardest part of the dissertation process, starting it. My colleagues in the NWS

Reproduced with permission of the copyright owner. Further reproduction prohibited without permission.

and the COMET Program have been enormously supportive and an important part of my motivation to complete this process. A wonderful addition to this experience has been meeting and working with Dr. Sue van den Heever. She has helped me through every step of this process, and I thank her for her assistance with setting up and running RAMS and analyzing the output, and most importantly, for her friendship.

I am especially grateful for the support I received from my family throughout this endeavor. My father, Prof. Michael Mulvihill, played my constant motivator and reviewed each chapter of this manuscript along the way with enthusiasm and gentle suggestions. My mother, Ann Mulvihill, makes me believe I can do anything, and gives me unending support and encouragement. My daughter Bailey has been very patient with this process and has helped me look at the world in new ways. Most of all, I thank my husband, Dan Page, for helping me through the tough times and celebrating my successes.

Reproduced with permission of the copyright owner. Further reproduction prohibited without permission.

TABLE OF CONTENTS

Reproduced with permission of the copyright owner. Further reproduction prohibited without permission.

Reproduced with permission of the copyright owner. Further reproduction prohibited without permission.

Chapter 1
Introduction

Wildfires burn thousands of acres of land every year, and regions subjected to severe fire behavior experience significant changes in landscape characteristics. Wildfire burn scars show decreased vegetation through burning, and darkening of the soil surface and drying of sub surface soil layers. This study explores the changes to the microclimate and local heat budget of the region as a result of these environmental changes.

Changes in vegetation and soil properties leave burn scars more susceptible to flooding and erosion (Cannon et al. 2001). Many post-fire floods have caused loss of life and extensive property damage (Chen et al. 2001). The timing of the fire and subsequent precipitation events help define the potential and severity of resulting flooding. Precipitation events that occur closer to the fire event, when the environment is recently disturbed and has had less time to recover, can result in severe flooding and erosion. Examples of such post-fire floods include the Buffalo Creek flood in Colorado in 1996.

Because of the changes in soil characteristics, less rainfall is necessary to produce a flood than would occur over an undisturbed environment (DeBano 2000). The potential flash flood danger has been recognized by NOAA's National Weather Service and guidance has been modified with the help of land management agencies to better alert the public of possible flood hazards.

Reproduced with permission of the copyright owner. Further reproduction prohibited without permission.

This study explores the effects of landscape changes on the microclimate of the burn scar and extends those effects to investigate the potential changes in precipitation patterns and microphysical characteristics of storms over and near the burn area. Any changes induced by the burn scar could affect the flooding potential of an environment already more vulnerable to flooding and erosion.

Chapter 2 reviews previous work investigating effects of fire on the environment, differential heating induced by heating of heterogeneous surfaces, the development of nonclassical or physiographically-forced mesoscale circulations, and the effects of surface heterogeneity in the development of convective rainfall. In addition, specific studies of burn scars are summarized in terms of effects on local wind flow, precipitation development, and hydrologic response.

Chapter 3 covers the methodology used in this study. The Colorado State University Regional Atmospheric Modeling System was used to run simulations of an environment that included a burn scar. The purpose was to examine the effects of changes in the microclimate and developing precipitation by investigating the physical processes at work in terms of effects on cloud dynamics and microphysics. By examining the cloud processes, effects of the fire scar on precipitation efficiency and potential for cloud electrification and lightning initiation were inferred.

The results of the initial experiments are presented in Chapter 4, and related sensitivity tests are covered in Chapter 5. A detailed discussion of the findings from all of the experiments is in Chapter 6, while conclusions of the study and suggestions for future work are offered in Chapter 7. Research referenced in this study is listed in Chapter 8.

Reproduced with permission of the copyright owner. Further reproduction prohibited without permission.

Chapter 2

Background

2.1 Introduction

Wildfire causes a variety of changes to the environment in which it occurs. The post-fire region is often called the burn area, burn scar, or fire scar, and all terms will be used interchangeably in this study. Burning of vegetation by wildfire alters the surface roughness, evapotranspiration, surface albedo, soil moisture, and soil characteristics. (Chambers et al., 2003; Amiro et al., 1999; Ulery and Graham, 1993)

The differences in surface and soil characteristics within a burn scar compared to surrounding regions not affected by the fire arise because of contrasting responses to incident solar radiation (Chambers et al., 2005; Amiro et al., 1999). Thus, surface heterogeneity between the burn scar and the surrounding area provides a scenario where differential surface heating can occur altering the post-fire surface energy budget (Chambers 2005). Differential surface heating has been shown to trigger the development of mesoscale circulations (Segal and Arritt, 1992). While the land/sea breeze has been described as the classic type of this circulation, other contrasts in landscape can initiate mesoscale circulations. Such contrasts include variations in soil moisture, snow and cloud cover, as well as others. Mesoscale circulations provide a mechanism for lift and can enhance and trigger the development of convective precipitation. Marshall et al. (2004)

Reproduced with permission of the copyright owner. Further reproduction prohibited without permission.

found that the convective precipitation associated with a sea breeze depended on both the strength and the location of the circulation that helped produce it. Pielke (2001) associated changes in surface energy budget and development of mesoscale circulations due to land cover changes with increased thunderstorm potential and intensity. Previous numerical studies of the effects of fire scars on local wind fields and precipitation patterns have indicated that a burn scar is capable of developing a mesoscale circulation and affecting not only the track of convective storms, but the intensity as well (Chen et al., 2001; Knowles, 1993).

Surface and soil modifications caused by wildfire also affect the hydrologic response of the watersheds enclosing the burn scar. Reduced surface vegetation results in less interception of rainfall. Post-fire soils exhibit hydrophobic properties that inhibit infiltration into the soil. The result of both of these changes is to increase the amount of surface runoff and potential for flooding and erosion (DeBano, 2000). Chen et al. (2001) found that their simulations of a specific burn scar influenced both the track and intensity of convective precipitation over a burn scar that experienced a flash flood. The present study explores the effects burn scars have on development, track, and characteristics of convection over a region already more susceptible to flooding.

2.2 Effects of fire on surface and soil features

2.2.1 Surface albedo changes

Amiro et al. (1999) reported surface albedo decreased immediately after fires due to the blackened surface of the fire scar. In previous numerical simulations of fire scars, albedo values of 0.05 and 0.07 were used for the fire scar areas to model the blackened

Reproduced with permission of the copyright owner. Further reproduction prohibited without permission.

surface due to scorching of the soil and vegetation by the wildfire (Knowles, 1993; Chen et al., 2001).

2.2.2 Vegetation changes

Fire plays and important role in ecosystems and the life cycle of vegetation (Chandler et al., 1983), but in this study we focus on the resulting effects observed just after the fire is extinguished, before vegetation has regenerated.

Fire severity has been classified based on the effects on the environment, and correlated to surfaces temperatures during the fire (Chandler et al., 1983). Low intensity fires have surface temperatures of 100-250°C and result in light burning of vegetation with scorched areas and remaining live vegetation. Moderate intensity fires are associated with surface temperatures of 300-400°C during which extensive burning of organic material uncovers the mineral soil. High intensity fires are associated with surface temperatures that exceed 500°C, during which even large fuels are completely burned and soil characteristics are modified.

Fire reduces the amount of dead fuels (pine needles, timber litter, and other dead vegetation) on the ground surface and damages live vegetation. The net result is a decrease in surface roughness and transpiration from the vegetation that remains.

2.2.3 Soil changes

Fire can affect soil characteristics both at and beneath the surface. Ulery and Graham (1993) examined soil samples affected by varying burn severity and noted changes in the color as well as the texture of the soil. Severely burned soil, estimated to

Reproduced with permission of the copyright owner. Further reproduction prohibited without permission.

make up 1 to 2% of the total land area, had light gray ash on the soil surface, reddened soil in the upper few centimeters of the soil, and a blackened layer beneath that layer. In these soil samples, 80-100% of the organic carbon had been removed by the fire. The reddened soil also showed a larger proportion of sand-size particles than unburned soil in the same region. Using polarized light microscopy, they found sand-sized aggregates of smaller soil particles and concluded these particles had formed during heating by the fire and were responsible for a shift from clay-sized to sand-sized particles in the soil particle size distributions. They estimated that the portions of the burn scar with reddened soil had reached temperatures near 400°C or greater. This severely burned soil was found under burned logs and was thus subjected to high temperatures for prolonged periods of time. One soil sample examined did not show the same shift in particle size distribution, but rather a greater fraction of silt with lower fractions of both sand and clay than the unburned sample. Ulery and Graham asserted that this soil was subjected to even higher temperatures during the fire (≥500°C), and the additional heating caused a breakdown in the sand-sized aggregates.

The temperature reached in the soil during the fire and duration of that temperature both influence resulting effects on soil characteristics (Certini, 2005). While the temperature reached in the soil during the fire governs the changes that occur in the soil, the duration of those conditions dictates the extent of the alteration of the soil. Soil moisture moderates soil temperature changes during the fire in that the temperature will not exceed 95°C until the water in the soil has vaporized (Campbell et al. 1995).

2.3 Differential Heating Over Heterogeneous Surfaces

Reproduced with permission of the copyright owner. Further reproduction prohibited without permission.

The Earth's surface heats due to incident solar radiation during daylight hours. This radiation absorbed by the ground acts to heat the atmosphere above it. Heat is then mixed in the boundary layer by turbulence. Depending on the stability of the atmosphere, such turbulence can act to develop convective clouds and precipitation (Oke, 1987, Stull, 1988, and Pielke, 2002).

With burn scars, during the diurnal cycle, adjacent land areas react to surface forcing in a different manner. This was demonstrated by measurements taken during field experiments which detected a difference in surface temperature over land areas with dissimilar characteristics, namely burned and unburned regions (Chambers et al., 2003; Amiro et al., 1999). For example, a burn scar shortly after a wildfire has drier soil, less vegetation, and darker surfaces. The response to solar heating will be to put more energy into the sensible heat flux and soil heat storage than in the latent heat terms of the heat budget. In addition, the lower albedo of the surface will allow more incident solar radiation to be absorbed because less is being reflected.

2.3.1 Surface heat budget

Pielke (2001) stated that changes to components of the surface heat and moisture budgets due to land use change would affect thunderstorm potential and intensity. The surface heat budget can be represented by

$$R_N = Q_G + H + L(E + T) \tag{2.1}$$

Where R_N is the net radiative flux, Q_G is the soil heat flux, H is sensible heat flux, and the term $L(E + T)$ gives the latent heat flux with L being the latent heat of vaporization, E is evaporation and T is transpiration.

Reproduced with permission of the copyright owner. Further reproduction prohibited without permission.

Net radiation combines the incoming solar radiation that is not reflected at the surface with the net loss of longwave radiation leaving the surface and can be represented by

$$R_N = Q_S(1-A) + Q_{LW}^{\downarrow} - Q_{LW}^{\uparrow}$$

where Q_s is the insolation, A is the albedo, $Q_{LW}^{\downarrow} - Q_{LW}^{\uparrow}$ is the net longwave radiation. The decrease in albedo over the burn scar due to charring of vegetation and the soil surface results in an increase of shortwave radiation absorbed at the surface (Amiro et al., 1999). This increase would act to increase the net radiation, but there is some balance to this increase by the outgoing longwave radiation, $Q_{LW}^{\uparrow}$ which is given by

$$Q_{LW}^{\uparrow} = (1-\varepsilon)Q_{LW}^{\downarrow} + \varepsilon T_s^4$$

where ε is the surface emissivity, $Q_{LW}^{\downarrow}$ is the incoming longwave radiation, and T_s is the surface temperature (Pielke, 2001). Since T_s will increase with greater absorption of solar radiation, the outgoing longwave radiation will increase as well.

Observations over burn scars by Amiro et al. (1999) and Chambers et al. (2005) showed that lower albedo did not necessarily result in increased net radiation. Amiro et al. (1999) evaluated data over the Canadian boreal forest, and found little change in net radiation over regions affected by wildfire. Chambers et al. (2005) found a 12% increase in net radiation over the western Alaska tundra site studied and a 10% decrease in net radiation over the central Alaska black spruce forested region, both affected by wildfire. Of greater significance, however, is how the net radiation was partitioned between the other terms in the energy balance equation.

Reproduced with permission of the copyright owner. Further reproduction prohibited without permission.

Net radiation, following equation 2.1, is balanced by the terms Q_G, H, E, and T. Because fire acts to damage or even destroy vegetation (Chandler et al., 1983), it is unlikely that transpiration would increase in the post-fire environment. Likewise, the upper portions of the soil are often dried and the surface layer of organic matter burned, which would decrease the amount of evaporation taking place at the surface (Certini, 2005). Therefore, the latent heat flux term $L(E + T)$ on the right hand side of equation 2.1 would decrease over the burn scar, and the soil heat flux Q_G, and sensible heat flux H, would balance both the change in net radiation and the decrease in latent heat flux.

Field observations over fire scars by Amiro et al. (1999) and Chambers et al. (2005), collected data that showed a greater amount of net radiation put into the sensible heat flux term. Amiro et al. (1999) evaluated data collected during the BOREAS experiments for fire areas greater than 200 ha where the entire area within the fire perimeter was assumed to be burned. They found that surface radiometric temperatures were 6°C warmer over burn scars than over surrounding areas. Increases of 10-20% in sensible heat flux were observed over the first few years after the fire, although little effect was seen in net radiation. Latent heat flux decreased and resulted in an increase in the Bowen ratio of approximately 50%, with effects lasting for seven years after the fire due to the decreased vegetation and thus decreased transpiration.

2.4 Nonclassical Mesoscale Circulations

The term nonclassical mesoscale circulation is a subset of physiographically-forced circulations and is used to describe thermally induced circulations due to heterogeneities in surface sensible heat flux on mesoscale spatial scales. Segal and Arritt

Reproduced with permission of the copyright owner. Further reproduction prohibited without permission.

(1992) provided a survey of specific types of these circulations induced by a variety of surface heterogeneities. These circulations are compared to what is considered a classic mesoscale circulation, the sea breeze. The mesoscale area of consideration includes a "perturbed area" in which surface sensible heat flux is significantly lower or higher than the surrounding region. The physical reasons for these differences were attributed to spatial heterogeneity in surface evapotranspiration, solar irradiance reflection and/or absorption, and sub-surface thermal storage. The research surveyed included both observational studies and numerical simulations.

Burn scars show differences in soil moisture, vegetation, and albedo changes, and the effects of each have been studied separately. First, the effects of surface evapotranspiration heterogeneities include studies based on differences in soil wetness and studies on differences in vegetation across a mesoscale domain. Numerical study of variations in soil moisture by Ookouchi, et al. (1984) showed that an extreme case of saturated soil compared to very dry soil, induced a surface flow similar to that of a sea breeze with a surface temperature contrast of approximately 18 K and a maximum surface wind due to the induced nonclassical mesoscale circulations of approximately 5 m s-1. In contrast, reducing the soil moisture contrast to a less extreme case resulted in a weaker wind speed of approximately 2 m s^{-1} and a surface temperature contrast of approximately 5 K.

In addition, surface soil texture heterogeneities resulted in contrast in surface evaporation with homogeneous soil moisture and as a result, differences in sensible heat flux which could possibly support generation of nonclassical mesoscale circulations (Mahfouf et al., 1987).

Reproduced with permission of the copyright owner. Further reproduction prohibited without permission.

Vegetation contrasts across a mesoscale domain provided forcing for nonclassical mesoscale circulations. Although observational studies did not find indications of thermally-induced flow, temperature gradients were observed (Anthes 1984, Segal et al. 1988). Simulations included an ideal contrast of vegetation that compared dry land to dense, widespread vegetation. These simulations showed the development of nonclassical mesoscale circulations of intensity similar to a sea breeze. Anthes (1984) also explored the scale of heterogeneities necessary to induce mesoscale circulations. He found that vegetative swaths on the order of 100 km could induce vertical circulations on the order of 10 cm s^{-1} up to 1 km above the surface.

Surface albedo contrasts have also been investigated as possible mechanisms for nonclassical mesoscale circulations development. Noted by Segal et al. (1986), the value of sensible heat over land is approximately linearly proportional to the solar irradiance absorbed at the surface. Generally, variations in albedo yielded weak nonclassical mesoscale circulations as found by Mahrer and Pielke (1978).

Segal and Arritt (1992) concluded that the observational studies supported less intense nonclassical mesoscale circulations than found by numerical simulations. Specifically, the observed circulations were weaker and more similar to lake breezes than sea breezes. They attributed these differences to assumptions made in the numerical simulations, such as perturbed areas being smaller in observed studies than in model simulations. Observed perturbed areas are not as uniform as those modeled, and observed circulations can be obstructed by background synoptic and mesoscale flow in that it is difficult to isolate mesoscale effects just due to the perturbed area. An important deficiency of numerical simulations is the assumption of uniform surface features in the

Reproduced with permission of the copyright owner. Further reproduction prohibited without permission.

perturbed area rather than real-world conditions, which are patchy rather than uniform and would have a reduced contrast with the surrounding area and result in reduced circulation intensity (Segal et al. 1988).

As summarized in Pielke (2001) and Pielke et al. (2006), land cover changes have a diverse but potentially large impact on the development of deep cumulus convection. Local wind convergence associated with the development mesoscale circulations can help initiate and focus the development deep convection.

2.5 Effects of surface heterogeneity on convective rainfall

The previous discussion describes how the heat balance equation terms are modified over a burn scar compared to the surrounding region. The burned area can be described as a 'perturbed area' described in Segal and Arritt (1992), and thus could induce local circulations due to the horizontal variations in sensible heat flux due to the presence of the burn scar. Flux terms differ between the perturbed area and the surrounding region. The burn scar causes dryer, warmer conditions compared to the surrounding region covered in vegetation with a larger albedo.

Differential heating has also been proposed as a mechanism for developing mesoscale boundary layer convergence zones. Wilson and Schreiber (1986) identified lines of convergence associated with the development of thunderstorms. Schreiber (1986) provided case study examples of boundary layer convergence lines identified on Doppler radar triggering deep convection.

Reproduced with permission of the copyright owner. Further reproduction prohibited without permission.

Changes in surface roughness over the fire scar would affect the direction and speed of wind flow over the domain with the development of localized areas of convergence and divergence. It is assumed that the surface roughness will decrease compared to the surrounding area due to the consumption of vegetation during the wildfire.

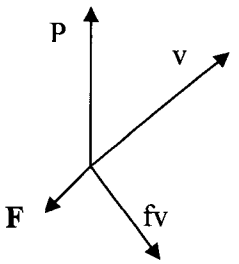

Figure 2.1 Vector diagram of effect of friction on wind direction (adapted from Holton, 1992).

As described by Oke (1987), the gradient wind slows with increasing friction. As a result, the Coriolis force (fv, where f is the Coriolis parameter and v is the wind speed) decreases in response to the decrease in wind speed. Since the Coriolis force is balanced by the pressure gradient force, which is independent of wind speed, the winds start to turn toward the direction of the pressure gradient force as seen in Figure 2.1.

A change in the surface roughness will cause a change in both the wind speed and direction. The frictional force will decrease over the burn scar because of the decrease in surface roughness. The winds over this area will then veer and increase in speed. This will result in speed divergence on the upwind side of the scar, and speed convergence on the downwind side. Similarly, confluence will occur on the right side of the scar with

Reproduced with permission of the copyright owner. Further reproduction prohibited without permission.

respect to the wind flow, and difluence on the left side of the scar with respect to the wind flow.

2.6 Previous Studies of Burn Scars

Some work has been conducted on the effects of burn scars on precipitation. These studies focused on the effects of fire scars on the local wind fields and development, strength, and patterns of precipitation (Knowles, 1993; Chen et al., 2001).

2.6.1 Development of mesoscale circulations over burn areas

Knowles (1993) modeled burn scars of different sizes and their effect on local circulation and precipitation. He found increased values of sensible heat flux over the burn scar and the development of mesoscale circulations in response to the lowering of surface albedo over the burn scar. The associated vertical updrafts were over 3.5 m s^{-1}. Model simulations also produced clouds and precipitation in response to the circulation. Additionally, he hypothesized that the clouds generated by the circulation could produce lightning and thus feedback into a greater number of lightning generated fires.

Sensitivity tests by Knowles showed that increasing the burn size resulted in stronger mesoscale circulations. Also, introducing geostrophic winds of 2.5 m s^{-1} and stronger reduced the strength of the circulation. Tests on stability showed that a stably stratified atmosphere produced weaker circulations that an unstable atmosphere.

A more recent study by Mölders and Kramm (2007) also reported the development of mesoscale circulations associated with burn scars of greater than 600 km^2 in size in Interior Alaska. They described the vertical motion induced by the burn scar as

Reproduced with permission of the copyright owner. Further reproduction prohibited without permission.

that seen in the "upward branch" of a mesoscale circulation. Significant differences in vertical velocity were attributed to large burn scars

In addition, Mölders and Kramm (2007) analyzed near surface fluxes, which showed local changes in net radiation, sensible heat, latent heat and ground heat fluxes in the vicinity of the burn scars. Greater surface heating was seen over the burn scars with increases in sensible heat flux 5% to 25% over burn scars compared to the pre-fire simulation. Significant differences in sensible heat flux between their pre-fire and post burn simulations were seen in burn scars larger than 600 km^2. Changes to latent heat flux were considered significant for burn scars larger than 800 km^2 with an average decrease of 12 W m^{-2}. Resulting changes in vertical velocity over and to the lee of burn scars were found to be significant for burns larger than 1600 km^{-2}.

2.6.2 Effects of burn scars on precipitation development

Chen et al. (2001) simulated a flash flood case that occurred over a burn scar. On July 12, 1996 heavy rain fell over the Buffalo and Spring Creek watersheds which had been burned by wildfire in mid-May of that year. In their experiments, their burn scar was defined by reducing the albedo from 0.15 to 0.05, the vegetation coverage was reduced by changing the roughness length from 0.5 to 0.3 m and reducing the soil moisture content of all the layers from 0.3 to the wilting point within the fire area.

Simulations of the fire region showed that including the burn scar in the model environment resulted in a precipitation field more closely related to the observed precipitation values than seen in simulations using undisturbed vegetation. The track of the convection was forced by the prevailing flow, but followed the axis of a warm temperature anomaly that was set up by the contrast in landscape characteristics that

Reproduced with permission of the copyright owner. Further reproduction prohibited without permission.

included the burn scar. Surface temperatures were predicted to be 5°C warmer over the burn area. The result was a predicted storm track closer to the burn scar with enhanced convection and precipitation values predicted by the model that more closely followed those observed in the burn region.

The Buffalo Creek fire burned approximately 50 km^2 (Yates, et al. 2000). Chen et al. (2001) concluded because the higher surface temperature that developed over the burn scar occurred over a relatively small area, it was insufficient to develop a significant mesoscale circulation that could initiate convection. They did note that the warmer temperatures over the burn scar could provide greater instability to help focus convection or even be a preferred location of convective initiation.

Mölders and Kramm (2007) studied the effects of burn scars on microphysics microphysical characteristics and distribution of precipitation using the MM5 model. Their study in Interior Alaska showed unique characteristics, such as the production of precipitation in the case they selected was due to as the assumption that local recycling of water is locally recycled. They saw little change in precipitation averaged over their domain. However, the precipitation distribution did show local changes with local increases of more than 12% in precipitation rates. On the leeside of burn scars, precipitation was seen to increase, while farther downstream, decreases in precipitation were predicted.

In their analysis of model predictions of cloud microphysics, Mölders and Kramm (2007) found local areas of both enhanced and reduced amounts of liquid cloud water, rain water, and graupel mixing ratios in their simulation containing burn scars. They asserted that the presence of the burn scars in their simulation reduced and redistributed

Reproduced with permission of the copyright owner. Further reproduction prohibited without permission.

in time and space graupel mixing ratio values, could result in a reduction in lightning frequency over an extended period of time.

2.7 Effects of Burn Scars on Hydrologic Response of Watersheds

Fire scars have proved to be more susceptible to flooding and erosion than unburned areas. Changes in the landscape characteristics contribute to this increased flood and erosion potential (Cannon et al., 2001, Yates et al. 2001). Changes in vegetation and soil conditions alter the water balance equation and shift a greater volume of precipitation into runoff (Johansen et al., 2001, DeBano, 2000, Yates et al. 2001).

The surface water balance equation can be written as:

$$R = P - I - S - ET \tag{2.2}$$

Where R is the surface runoff, P is the amount of precipitation that reaches the surface, I represents infiltration of water into the soil, S is the storage of water by vegetation, and ET is the evapotranspiration from the soil surface and vegetation. Fire acts to decrease the infiltration, and due to a reduction in the amount of vegetation, the storage and evapotranspiration terms also decrease. The net result is an increase in the amount of runoff, and thus less rainfall is needed to produce flooding.

Along with increased runoff generated over burn scars, the conditions of the watershed after burning make it more vulnerable to erosion. Johansen et al. (2001) studied the effects of reduced vegetation on sedimentation flow. In comparing the percentage of bare soil to the amount of sediment transported, they found that there was a sharp, non-linear increase in sediment flow for a watershed that had greater than approximately 60-70% of its surface exposed as bare soil as seen in Figure 2.2.

Reproduced with permission of the copyright owner. Further reproduction prohibited without permission.

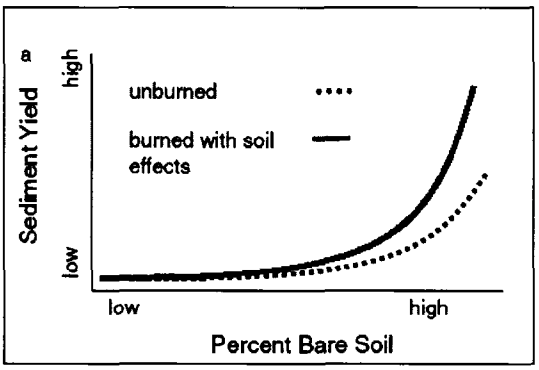

Figure 2.2 Conceptual model of resulting erosion as a function of the percentage of bare soil due to an unburned versus a burned watershed with altered soil characteristics. (From Johansen et al., 2001)

The infiltration rate of soil in fire scar regions is reduced due to chemical changes in the soil. Burning of organic matter at the surface and heating of the mineral soil beneath it results in a change of the chemical characteristics of the soil particles. These changes have been described as the "tin roof" effect (DeBano, 2000) in that the soil repels water during subsequent rain events and thus makes the burned area more susceptible to flooding and erosion as a greater percentage of the rainfall becomes runoff in the associated watershed.

The mechanism for the development of hydrophobic soil properties was described by DeBano (2000). Prior to wildfire occurrence, the surface collects organic matter and the soil can become water repellent due to drying out of the upper levels of the mineral soil and the organic matter. Other processes can contribute to water repellency in the soil such as fungal growth and release of hydrophobic substances during decomposition of vegetation.

Fire introduces a mechanism for both combustion and heating that acts to produce a temperature gradient at and into the soil surface. Depending on what is burning on and near the surface, temperatures above the surface in the fire can exceed 1100°C.

Reproduced with permission of the copyright owner. Further reproduction prohibited without permission.

Corresponding temperatures at the soil-organic matter interface can be as high as 850°C. However, dry soil is an effective insulator, so the temperature rapidly decreases beneath the surface to 150°C just 5 cm into the mineral soil DeBano (2000).

Combustion results in the vaporization of substances in the organic matter at the surface, which move along the temperature gradient into the mineral soil. Because of the steep temperature gradient within the upper levels of the soil, the vaporized hydrophobic substances move only a few centimeters into the soil before condensing onto soil particles. Thus, a hydrophobic layer develops below the soil surface and acts to reduce infiltration into the soil and increase the likelihood of erosion.

The sub-surface hydrophobic layer is covered by a wettable soil surface. This surface layer will allow infiltration during a rain event, but water movement will be impeded at the hydrophobic layer interface. As this surface layer becomes saturated, the stability of the soil which begins to erode. This erosion leads to the development of rills and open channels (DeBano, 2000).

2.8 Longevity of Burn Scar Influences

The duration of effects on vegetation and soil properties induced by wildfire are governed by how quickly the environment can recover from the changes induced by the fire, which depend on the severity of the fire. DeBano, (2000) stated that water repellency induced by low to moderately severe fires recovered faster than that induced by severe fires. Soil infiltration increased to that of soil not affected by fire after six years. Ulery and Graham (1993) found that changes in soil texture were observed to still be present three years after the fire.

Reproduced with permission of the copyright owner. Further reproduction prohibited without permission.

Albedo over the fire scars has been observed to increase and recover 5 years after the fire to even higher values than pre-fire conditions (Amiro et al., 1999). Re-growth of vegetation has a major influence on post-fire environments. Liu et al. (2005) looked at annual surface energy budgets over burn areas of various ages. They found that sensible heat flux was reduced over 3 year old and 15 year old burns compared to an 80 year old burn. These changes were attributed to the amount and type of vegetation at each site. The natural succession of vegetation in the post-fire environment governed the vegetative characteristics of the individual sites.

Amiro et al. (1999) reported increases in sensible heat of 10-20% persisted for the first few years after the fire, with little effect in net radiation. The decrease in latent heat flux resulted in a Bowen ratio increase near 50% that lasted for seven years after the fire primarily due to the decreased transpiration.

Thus, the effects of the fire on the surface and energy budget, and the hydrologic response of the watershed will depend on the amount of time between the fire and the developing precipitation event. Cases where flood producing rain events followed closely after the fire was extinguished have been severe (Yates et al., 2001, Underwood and Schultz, 2004).

2.9 Summary

Based on past studies, there is some indication that the presence of the burn scar may influence potential for and severity of convective precipitation over and in the vicinity of a burn scar. Changes in the surface energy budget and surface roughness over the burn scar and contrasts with the surrounding environment may be capable of modifying the local wind flow and possibly develop mesoscale circulations.

Reproduced with permission of the copyright owner. Further reproduction prohibited without permission.

The presence of burn scars have been shown to greatly alter the hydrologic response of a watershed. Decreased vegetation and soil property changes as a result of wildfire act to increase the amount of runoff from a precipitation event and increase the change of significant erosion. Both increase potential severity of floods.

The goal of the present study is to further examine how the presence of a burn scar affects the microclimate of the region and what results those effects have on the development and strength of convection and resulting precipitation. Details of the precipitation development include microphysical analysis of the developing clouds and the potential for the electrification and lightning development.

Reproduced with permission of the copyright owner. Further reproduction prohibited without permission.

Chapter 3

Methodology

3.1 Motivation for Study

The goal of this research is to explore the effects of a burn scar on the microclimate of a region and specifically on a precipitation event. The data used to initialize the model were taken from a flash flood event to test how the presence of a burn scar affects the development and track of precipitation in an environment capable of supporting heavy rain. The event was selected because the atmospheric environment supported development of flooding rain, and adding the presence of a burn scar would make the area more susceptible to serious flooding and erosion. A similar situation unfolded with the Buffalo Creek, CO flood in June, 1996 (Chen et al., 2001).

The effects of a burn scar were simulated and these experiments were evaluated to examine changes in wind field, surface heat fluxes, temperature, and precipitation patterns and characteristics induced by the burn scar.

Sensitivity tests were conducted to evaluate the effects of changing the characteristics of the burn scar and the wind profile in the initial environment.

3.2 Model Description and Configuration

This study utilized version 4.3 of the Regional Atmospheric Modeling System (RAMS) as described by Pielke et al. (1992) and Cotton et al. (2003). The non-

Reproduced with permission of the copyright owner. Further reproduction prohibited without permission.

hydrostatic model was run in three dimensions using Cartesian horizontal coordinates and a terrain-following vertical coordinate.

The domain selected lies within the Konza Prairie of Kansas. This portion of eastern Kansas is described on the Konza Prairie Long Term Ecological Research Program website maintained by Kansas State University (www.k-state.edu/konza/location.htm) and is characterized by native tall grass in silty clay loam soils. Fire plays an important role in the natural ecosystem of the region.

A single grid was employed centered at 39.1° N and 96.6° W and defined by 140 grid points in the x direction, 170 in the y direction and 35 vertical levels extending up to 23 km following the work of van den Heever (2001). A horizontal grid spacing of 1 km was used with a time step of 5 s. The time differencing scheme uses a hybrid combination of leap-frog and forward-in-time methods. Turbulence closure follows the Smagorinsky (1963) deformation-K closure scheme with modifications described by Lilly (1962) and Hill (1974).

To best study the effects on microphysical characteristics of developing convection, a two-moment bulk microphysics scheme described in Cotton et al. (2003) and Saleeby and Cotton (2004). In this scheme, a bin approach is emulated for collection and sedimentation. Convection was explicitly resolved. The Harrington (1997) radiation scheme was selected because it includes interaction of both long and shortwave radiation with the liquid and ice hydrometeor size-spectra.

To simulate land-surface interaction, the LEAF-2 soil and vegetation model (Walko et al., 2000) was used with background surface vegetation of tall grass and a silty clay loam soil type. This model was used to induce the surface energy budget changes

Reproduced with permission of the copyright owner. Further reproduction prohibited without permission.

associated with the burn scar. Eleven soil levels were used over a depth of 0.5 m. Soil moisture was initialized uniformly over the burn scar. Additionally, the surrounding region had uniform soil moisture. The soil moisture was uniformly defined over the domain with drier values in the upper three layers of the burn scar.

Upper boundary conditions include a rigid lid with a four-layer Rayleigh friction layer to dampen gravity waves. Lateral boundary conditions follow Klemp and Wilhelmson (1978) and allow disturbances to propagate across the boundaries while minimizing reflection. The Coriolis force was activated in the model.

To isolate the effects of a burn scar on the microclimate of the region, idealized three-dimensional simulations were conducted. Fire effects were first modeled as just surface and soil moisture changes in the burn scar region with changes in albedo, vegetative coverage, and surface roughness. Sensitivity tests were then conducted to look at effects of soil moisture, wind profile, and burn scar size.

After analyzing the changes in microclimate induced by the presence of the burn scar, simulations on the effects of the scar on the development and coverage of precipitation producing storms were explored.

3.3 Model Initialization

The model was horizontally homogeneously initialized with a modified version of the 12 UTC sounding taken in Topeka, Kansas on August 30, 2003. The environment on this day led to heavy rainfall and a subsequent flash flood near Emporia, KS. The sounding used is plotted in Figure 3.1. This sounding was selected to examine the effects of a burn scar on an environment already primed for heavy rainfall. Because the observed wind profile was so strong on this day, the actual winds were reduced by 75% of the

Reproduced with permission of the copyright owner. Further reproduction prohibited without permission.

observed values in the initial simulation. A sensitivity test with the actual wind profile was later run and discussed in Chapter 5.

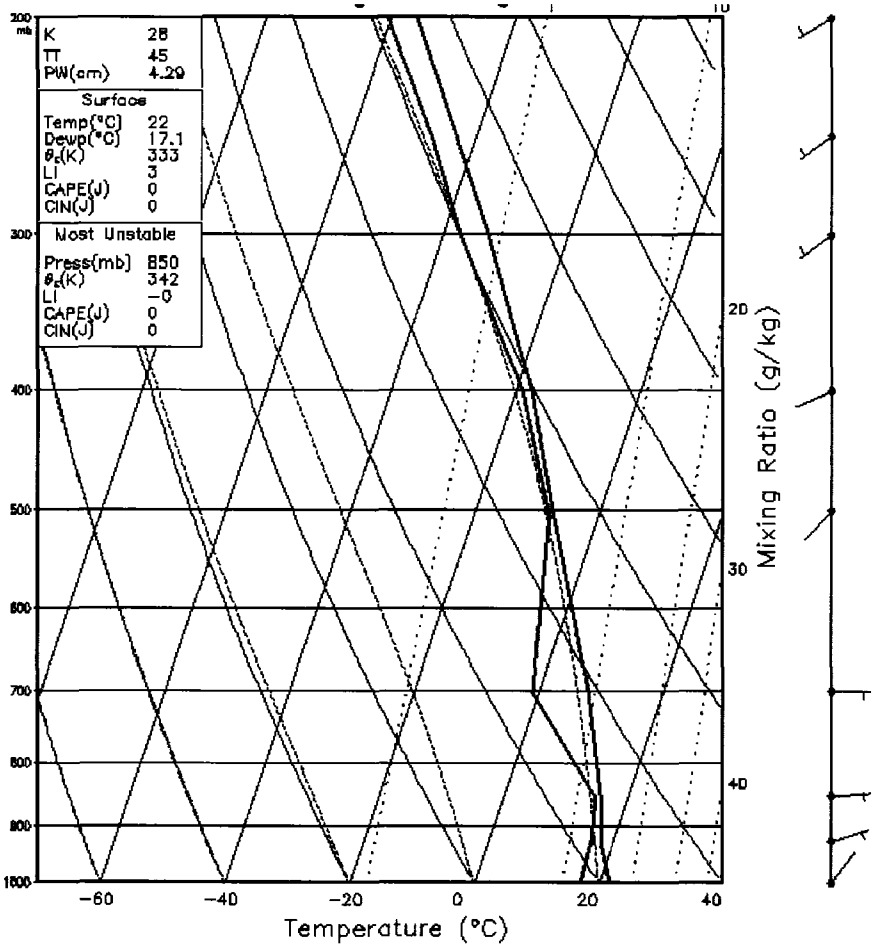

Figure 3.1 Atmospheric sounding taken in Topeka, KS at 12 UTC on August 30, 2003 with wind profile damped by 75%.

3.4 Burn Scar Initialization

A square burn scar was introduced into the domain to simulate the effect of a significant fire on the microclimate of the region. The pattern used follows work by Avissar and Liu (1996) in their numerical study of land surface forcing of convective

Reproduced with permission of the copyright owner. Further reproduction prohibited without permission.

clouds and precipitation. They found that an isolated square patch of dry land framed by a wet land region concentrated the development of mesoscale circulations and precipitation in the domain compared to configurations of alternating wet and dry land strips. This configuration also better represents a typical burn scar, which would tend to be an enclosed area rather than a strip of terrain. The location of the burn scar in the domain is shown in Figure 3.2.

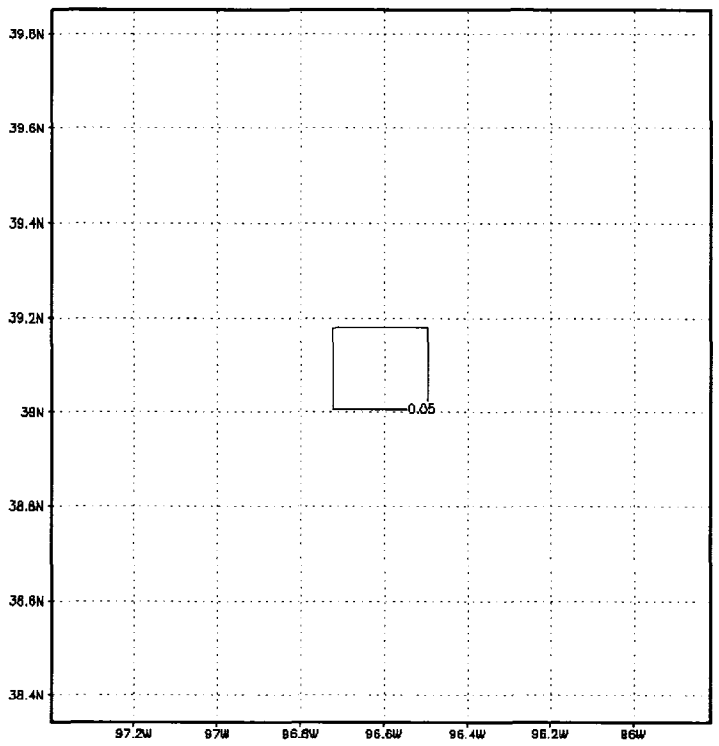

Figure 3.2 Burn scar outlined as 0.05 albedo value in model domain.

The burn scar in these experiments is located near the center of the domain as a 20 km by 20 km square, covering an area of 400 km^2 or roughly 99,000 acres. This size corresponds to a large, but realistic burn scar and was used by Knowles (1993) in an earlier study.

Reproduced with permission of the copyright owner. Further reproduction prohibited without permission.

The characteristics inside the burn scar are defined as homogeneous. The region surrounding the burn scar is also homogeneously defined with different characteristics. This configuration is designed to test the effects due to the modification of surface characteristics after a fire on the microclimate of the region. The burn scar characteristics are based on assumptions of a uniform fire of moderate intensity that reached surface temperatures between 300-400°C (Ulery and Graham, 1993) and completely burned the surface organic material, and blackened the soil surface.

The burn scar was defined in the model with a new land use class in the Leaf-2 scheme following the work by Rozoff (2002). LEAF-2 employs several physical parameters for each land-cover class that include albedo, Leaf Area Index (LAI), emissivity, roughness length, root depth, and fractional vegetation coverage. The "burnscar" land use class was adapted from the tall grass prairie class, which was the background vegetation used for the environment surrounding the burn scar in the domain.

Within the burn scar, albedo was set to 0.05, following Knowles (1993) and Chen et al. (2001), while a background albedo of 0.20 was used for the surrounding tall grass. The leaf area index (LAI) of 6.0 was used for the tall grass in the surrounding area and was reduced to 0.5 in the burn scar area. The emissivity was left unchanged for the burn scar. The roughness length was reduced from 0.1 to 0.01 m, due to the assumption that surface vegetation was nearly completely burned. The root depth was changed from 1.0 to 0.7 m for the burn scar to account for damage done to the surface vegetation by the fire. The fractional coverage of this land-use type was set to 0.9 to define the burned region. The particle characteristics of the soil were left unchanged, but the soil moisture was altered. The soil moisture is defined in the model relative to a saturation value of 1.0.

Reproduced with permission of the copyright owner. Further reproduction prohibited without permission.

The surrounding environment had soil moisture values of 0.40, 0.40, and 0.25 in the top three layers, which extend from the surface to 0.06 m below. In the burn scar area the values were reduced to 0.15 in these three soil layers to represent drying of the soil due to the fire. Such discontinuities in soil moisture have been associated with differential heating at the surface, and Avissar and Liu (1996) concluded that from previous experiments by Chen and Avissar (1994), such a discontinuity could increase precipitation amount.

3.5 Experiments

The primary simulations were initialized at 12 UTC and the model was run initially for ten hours, one with and one without the burn scar, to evaluate the effects of the burn scar on the atmospheric environment. Two additional experiments tested the effects of the scar on convective development by forcing convection at 1900 UTC. Convection was initiated in the model as an isolated warm bubble over the burn scar. Following the work of van den Heever (2001), a 9 by 9 km bubble was introduced by increasing the temperature by 3 K and moisture values by 20%. The bubble was placed over the region of maximum upward velocity induced by the burn scar. The second experiment placed the bubble in the same location in the domain without a burn scar.

Results were analyzed to determine the effects of the burn scar on the pattern and amount of precipitation forecast, and the microphysical characteristics of the storm. The results of these experiments are presented in Chapters 4.

3.6 Sensitivity Tests

Reproduced with permission of the copyright owner. Further reproduction prohibited without permission.

Several sensitivity tests were conducted to further evaluate the effects of fire on the microclimate of a region. These tests included variations of wind profile and soil moisture. The results of these tests are presented in Chapter 5.

3.6.1 No-burn test

The model was run without the burn scar to better evaluate the effects on convective development and precipitation patterns. The simulations were run for six hours starting at 1200 UTC as was done with the burn scar, and then convection was initiated with the warm bubble. This test showed how convection would be maintained and organized in an environment not affected by fire.

3.6.2 Soil moisture changes

In the original simulation with the burn scar, the soil moisture was reduced in the scar to simulate drying due to the fire. In this test, soil moisture was uniformly specified across the domain to investigate how much of the impact on the environment could be attributed to soil moisture differences.

3.6.3 Wind profile changes

The winds in the actual sounding that was adapted to initialize the model were very strong and depicted in Figure 3.3. A simulation using this original wind profile was run to see how strong winds modify the microclimate effects of the burn scar. Lighter winds were used in the first simulation to help isolate the burn scar forcing.

Reproduced with permission of the copyright owner. Further reproduction prohibited without permission.

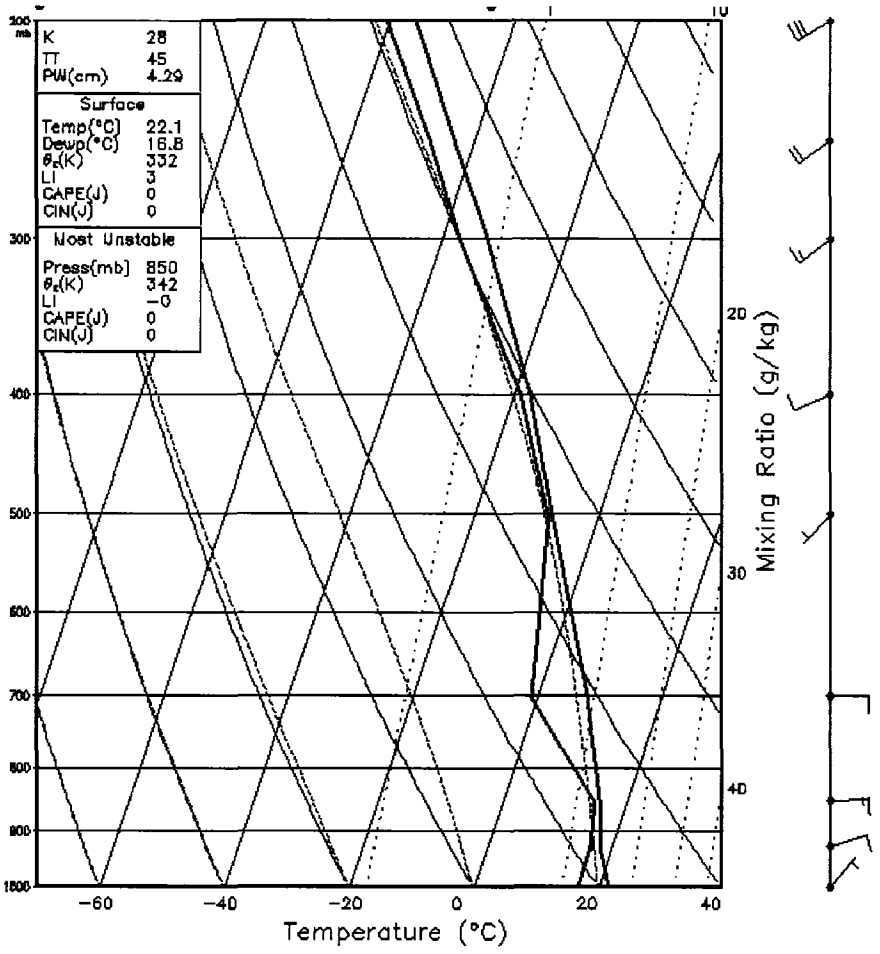

Figure 3.3. Atmospheric sounding taken in Topeka, KS at 12 UTC on August 30, 2003 with actual wind speed values.

The experiments conducted in this study were designed to investigate the effects of a burn scar resulting from a widespread, intense fire on the microclimate of the region and the resulting precipitation pattern and amount from a specific convective event. The results of the primary experiments are presented in Chapter 4, and the results of the sensitivity tests are presented in Chapter 5.

Reproduced with permission of the copyright owner. Further reproduction prohibited without permission.

Chapter 4

Results

4.1 Introduction

The results of simulations of effects of a burn scar on microclimate are presented in this chapter. Detailed evaluations of changes to surface and atmospheric parameters are conducted over the burn scar and the surrounding environment. The focus is on the interaction between conditions induced by the burn scar and those occurring over the surrounding environment, undisturbed by fire.

In these initial simulations, a 20 x 20 km burn scar was placed in the center of the 140 km by 170 km model domain. The surface and soil moisture characteristics were modified within the scar to model those after a fire.

After evaluating the changes induced by the burn scar, effects of these changes were investigated by adding a convective cell and tracking the effect of the scar on its intensity and resulting precipitation pattern. The convective cell was simulated by adding a warm, moist bubble of air over the scar and tracking how the induced system evolved with time. This simulation was later compared to a separate simulation of a warm bubble over the undisturbed environment

The convective cells in both simulations were analyzed in terms of the dynamics and microphysics of the clouds induced. Fields evaluated include vertical velocity, cloud water, rain water, graupel, and pristine ice. Details of the cloud microphysics were related

Reproduced with permission of the copyright owner. Further reproduction prohibited without permission.

to the amount of precipitation that fell in the simulations and the potential for electrification of the cloud and production of lightning.

4.2 Effects of burn scar on microclimate

Several parameters were examined to explore the change in microclimate over and around the burn scar. Large impacts were seen near the surface of the burn scar and impacts extended to a lesser degree farther above the ground. The effects of the burn scar were evaluated by first examining the surface temperature field changes due to reduced albedo and soil moisture. To further evaluate the heating effects, sensible heat flux and latent heat flux were assessed. The horizontal wind field was analyzed for changes due to the presence of the burn scar. The vertical velocity pattern was then examined to see whether upward motion was induced by the differential heating over the domain. Since upward motion was found over the burn scar, cloud water distribution was investigated to evaluate the cloud induced by the addition of the fire scar.

4.2.1 Surface air temperature

With the addition of the burn scar with lower albedo and soil moisture, increased surface heating results due to the greater amount of solar radiation absorbed by the surface. To see these effects, first the surface air temperature is examined. The simulation began at 12 UTC with the sounding described in Chapter 3 and depicted in Figure 3.2.

Reproduced with permission of the copyright owner. Further reproduction prohibited without permission.

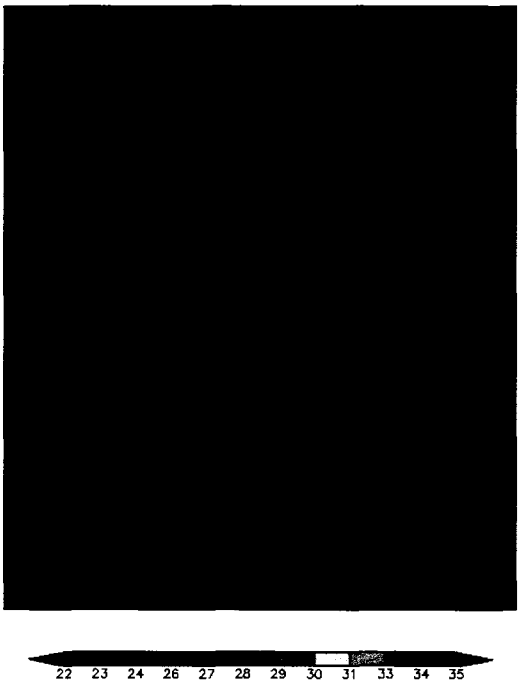

Figure 4.1 Surface temperature in degrees Celsius at 1500 UTC.

After three hours of heating, the surface air temperature field was evaluated at 1500 UTC. The effects of the burn scar, in the center of the domain, are visible in the 2-m temperature field, which is taken as the surface air temperature in this study and presented in Figure 4.1. The surface temperature differences between the burn scar and the surrounding area are 3°C. The surface temperature appears uniform in the burn scar with maximum values of 26°C, whereas a temperature of 23°C is seen over the surrounding environment. Consequently, a strong temperature gradient formed along all boundaries of the burn scar.

Reproduced with permission of the copyright owner. Further reproduction prohibited without permission.

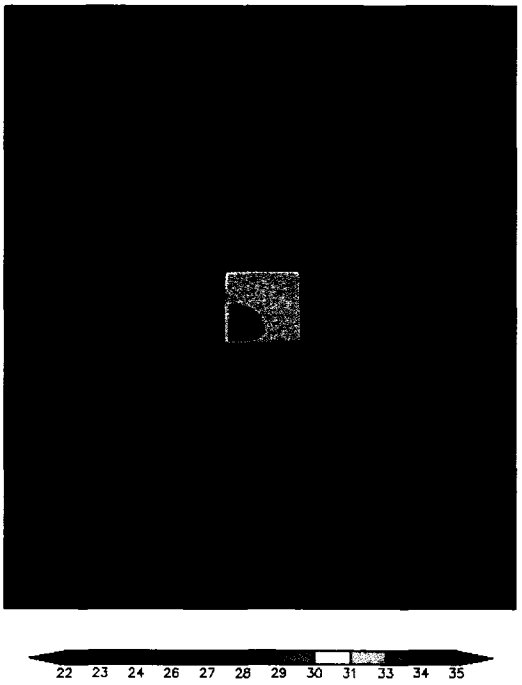

Figure 4.2 Surface temperature in degrees Celsius at 1800 UTC.

Figure 4.2 shows the surface air temperature plotted over the domain at 1800 UTC. As the simulation progressed, the temperature difference between the burn scar and the surrounding environment increased to 8°C by 1800 UTC as the ground surface heated due to solar radiation. Warmer temperatures were predicted in the southwestern corner of the fire scar and the influence of the scar extended to the southwest due to advection by the low level winds. The region of the burn scar is still clearly evident in the surface temperature pattern with the maximum values over 34°C within the highest contour in contrast to 26°C over the surrounding environment.

Reproduced with permission of the copyright owner. Further reproduction prohibited without permission.

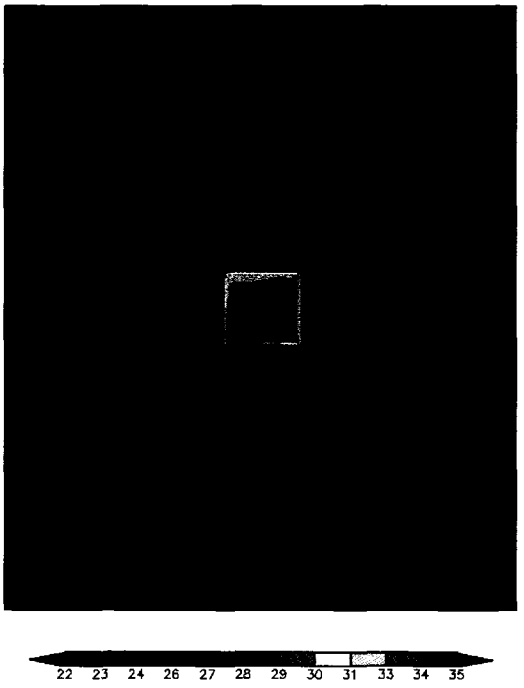

Figure 4.3 Surface temperature in degrees Celsius at 1900 UTC.

At 1900 UTC, the effects of advection are more obvious as surface heating continues and the difference between the surface temperatures over the fire scar and the surrounding environment rose to 10°C as seen in Figure 4.3. The maximum value has risen to 36°C and the surrounding environment has warmed slightly to 26°C. The highest values of surface temperature continue to be found in the southwestern part of the scar area. The northeasterly surface wind influenced the temperature distribution by concentrating the higher temperatures in the southwestern part of the scar and extending warmer temperatures into the surrounding environment.

Reproduced with permission of the copyright owner. Further reproduction prohibited without permission.

Figure 4.4 Surface temperature in degrees Celsius at 2000 UTC.

The surface temperature field shown in Figure 4.4 shows the effects of convection by 2000 UTC. The maximum temperature over the burn scar has shifted to the eastern corners as the surface was shaded by clouds that started to form at 1850 UTC due to surface heating. This phenomenon will be further discussed in section 4.2.6 on the cloud water field. Maximum values over the burn scar were predicted to be 34°C while the surrounding area was 27°C with some areas a few degrees cooler. The complex distribution of the surface temperature field reflects the response of the atmosphere to the differential surface heating and is discussed as other atmospheric parameters are examined in the following sections.

Reproduced with permission of the copyright owner. Further reproduction prohibited without permission.

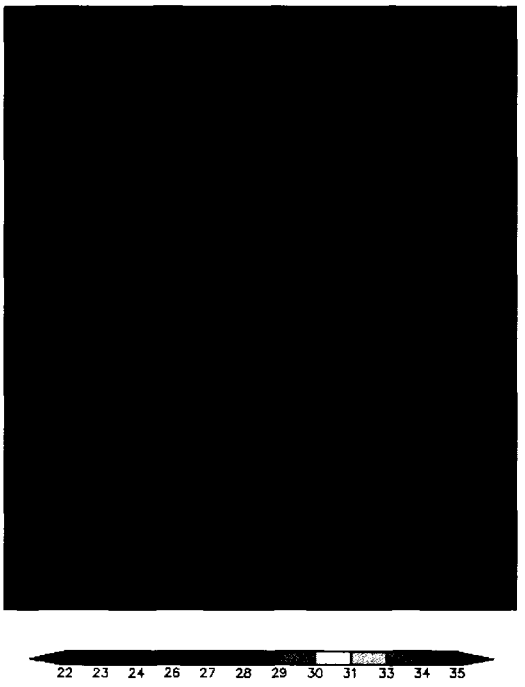

Figure 4.5 Surface temperature in degrees Celsius at 2100 UTC.

By 2100 UTC, as seen in Figure 4.5, the maximum surface temperature has cooled by 4°C to 30°C and remains in the eastern portion of the burn scar. A dramatic cooling signature is seen as widespread areas of temperatures as low as 25°C surrounding the burn scar. The effects of shading by the cloud field are more evident at this time, although the burn scar maintains significantly warmer surface temperatures than the surrounding environment.

4.2.2 Low-level wind flow

The wind field was examined at 10 m to determine the effects of the burn scar in the surface wind pattern. Although the physical surface characteristics over the scar differ with the surrounding environment, all changes in the 10 m wind field are assumed to be due to thermodynamic rather than frictional differences between the burn scar and the

Reproduced with permission of the copyright owner. Further reproduction prohibited without permission.

surrounding environment because the effects in the surface temperature field were seen immediately after the start of the simulation.

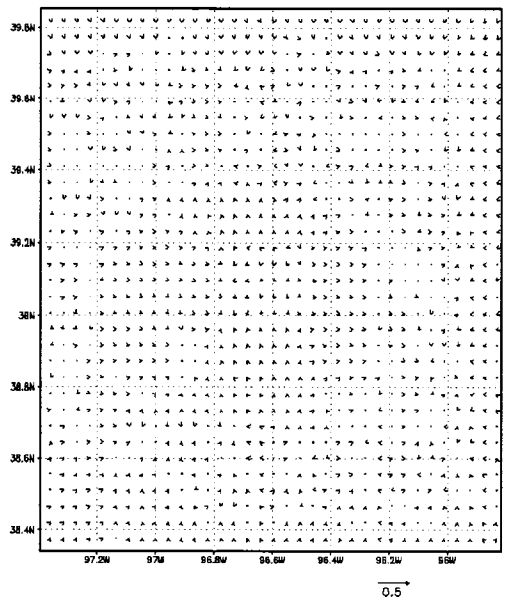

Figure 4.6 Wind anomaly vectors at 10 m at 1500 UTC.

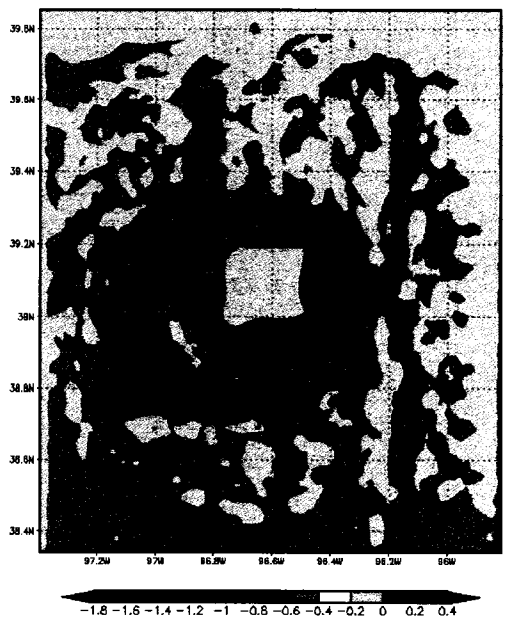

Figure 4.7 Surface divergence in s^{-1} (x 1000) at 1500 UTC.

Figure 4.6 shows the plot of the wind anomaly vectors which show the wind with the average flow removed at 30m above the surface at 1500 UTC. Little disturbance can be seen in the wind vectors at this time. Plotting surface divergence at 1500 UTC in Figure 4.7 shows broad divergence over the burn scar area, although the magnitude is small, on the order of $1 \cdot 10^{-4}\ s^{-1}$.

Reproduced with permission of the copyright owner. Further reproduction prohibited without permission.

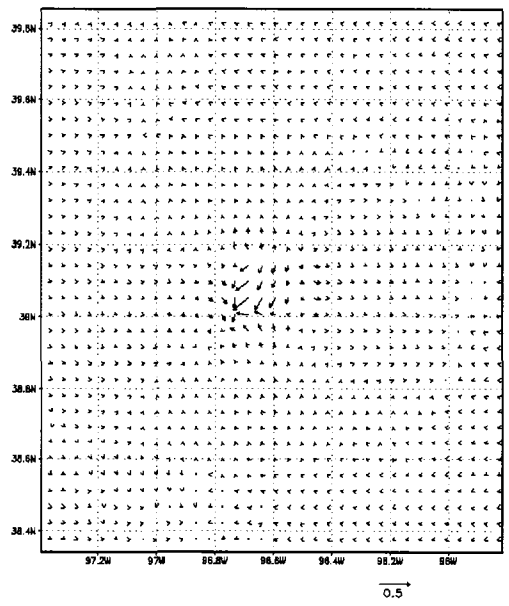

Figure 4.8 Wind anomaly vectors at 10 m at 1800 UTC.

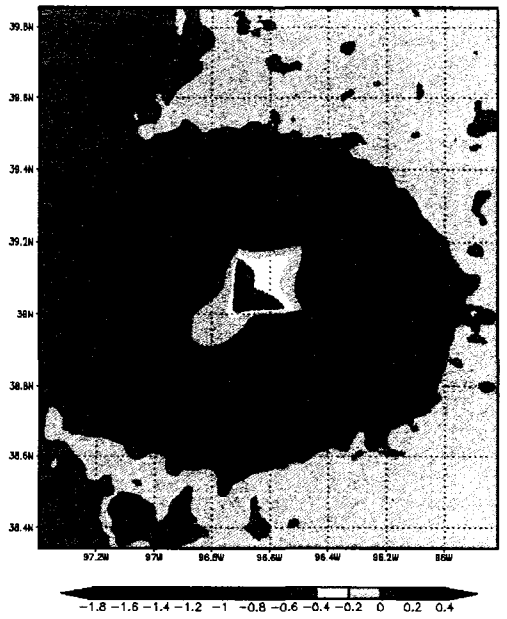

Figure 4.9 Surface divergence (x 1000) in s^{-1} at 1800 UTC.

At 1800 UTC, the wind anomaly vectors are plotted in Figure 4.8. The effects of the burn scar can be seen in the convergence in the southwestern corner of the scar and the stronger flow into the region. Figure 4.9 shows the surface divergence field has strengthened with the convergence in the southwestern section of the burn scar increasing to $1.8 \cdot 10^{-3}$ s^{-1} while the divergence field has only increased slightly to $3 \cdot 10^{-4}$ s^{-1}. Convergence is more concentrated while the surface divergence field is spread out and diffuse.

Reproduced with permission of the copyright owner. Further reproduction prohibited without permission.

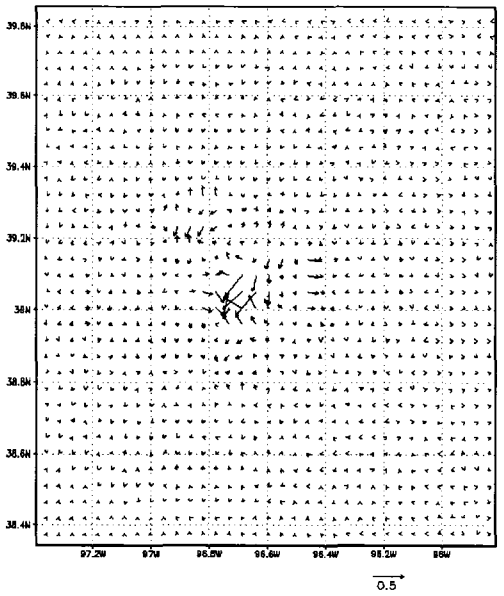

Figure 4.10 Wind anomaly vectors at 10 m at 2000 UTC.

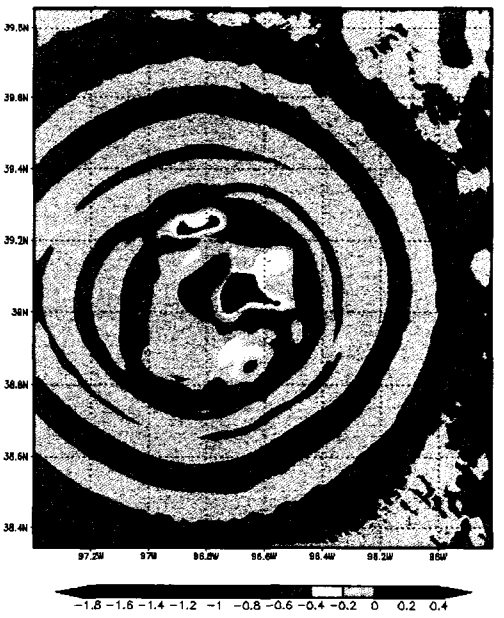

Figure 4.11 Surface divergence in s^{-1} (x 1000) at 2000 UTC.

At 2000 UTC, the effects of the burn scar are more pronounced in the wind anomaly vector pattern shown in Figure 4.10. Away from the burn scar, the flow field has been perturbed showing the widespread effect of the differential heating of the surface. Looking at the surface divergence pattern in Figure 4.11, the strength of the divergence and convergence continued to increase, and the convergence continues to be more concentrated and centered near the southwestern corner of the burn scar. The effects of the burn scar radiate outward over the surrounding environment and can be seen both in the wind field and the surface divergence field.

4.2.3 Sensible heat flux

Reproduced with permission of the copyright owner. Further reproduction prohibited without permission.

To further analyze the effects of the burn scar on the microclimate of the region, the sensible heat flux field is examined. This field will show the direct effects of the modification of the burn scar region on the surface energy budget.

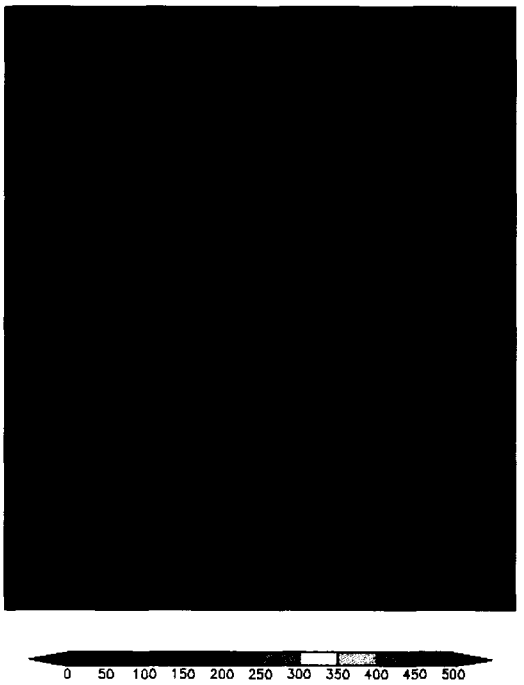

Figure 4.12 Sensible heat flux in $W \cdot m^{-2}$ at 1500 UTC.

The sensible heat flux over the domain at 1500 UTC is plotted in Figure 4.12. As with the temperature field, the effects of the burn scar are distinct. The highest values of sensible heat flux occur in the corners of the burn scar with values of 100 $W \cdot m^{-2}$.

Reproduced with permission of the copyright owner. Further reproduction prohibited without permission.

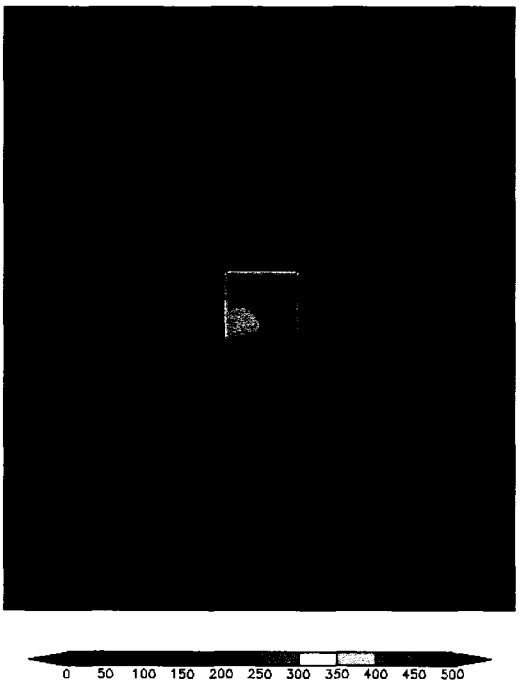

Figure 4.13 Sensible heat flux in $W \cdot m^{-2}$ at 1800 UTC.

At 1800 UTC, with increased daytime heating, the magnitude of sensible heat flux has increased over the domain, and the difference between the fire scar and the surrounding environment has increased substantially. Figure 4.13 shows the sensible heat flux plotted over the domain at 1800 UTC. Over the fire scar, values as high as 420 $W \cdot m^{-2}$ were predicted, while over the surrounding area, sensible heat flux is 100-150 $W \cdot m^{-2}$. The flux is greater over the northern and eastern portions of the scar. Lower values are seen over the surrounding environment extending over the southern and western boundaries of the fire scar.

Reproduced with permission of the copyright owner. Further reproduction prohibited without permission.

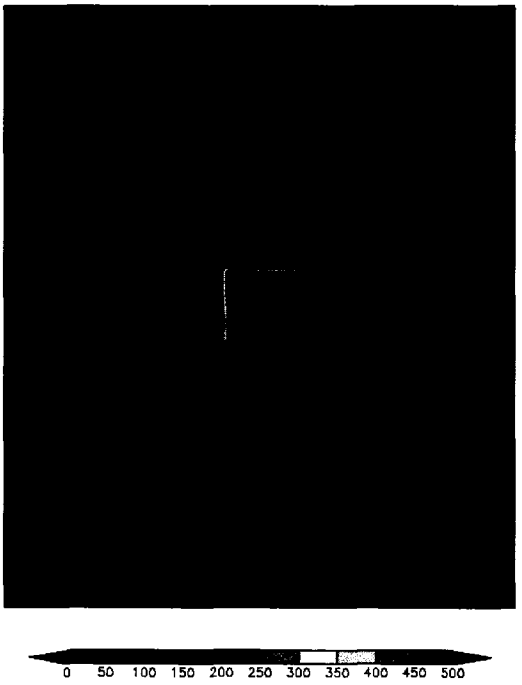

Figure 4.14 Sensible heat flux in W·m^{-2} at 1900 UTC.

By 1900 UTC, the sensible heat flux field plotted in Figure 4.14 is more uniform over the burn scar with increasing higher values in line with the greater surface heating by this time. The highest values over the scar are 495 W·m^{-2} and the surrounding environment has values of 100-150 W·m^{-2} with lower values seen downwind from the scar in the surrounding environment.

Reproduced with permission of the copyright owner. Further reproduction prohibited without permission.

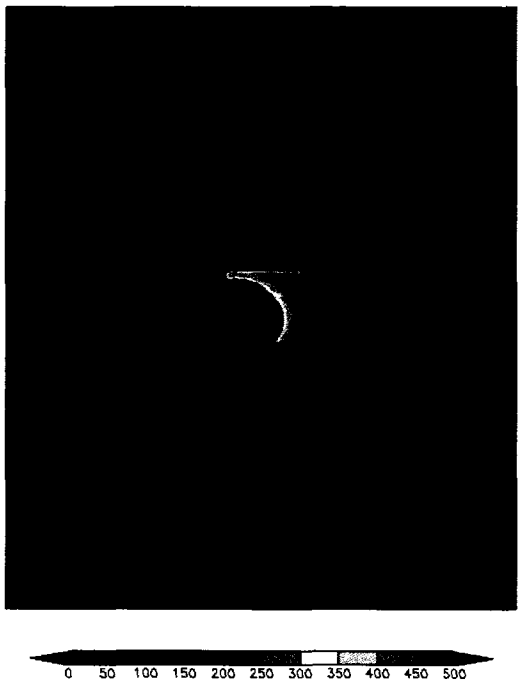

Figure 4.15 Sensible heat flux in $W \cdot m^{-2}$ at 2000 UTC.

At 2000 UTC, the sensible heat flux field shows the complexity of the disturbance induced by the differential heating of the surface as seen in Figure 4.15. The highest values of sensible heat flux are still seen in the northeastern portion of the burn scar with values as high as 490 $W \cdot m^{-2}$. Lower values of sensible heat flux can be seen immediately to the west of the scar as low as 0 $W \cdot m^{-2}$ and extending further west.

Reproduced with permission of the copyright owner. Further reproduction prohibited without permission.

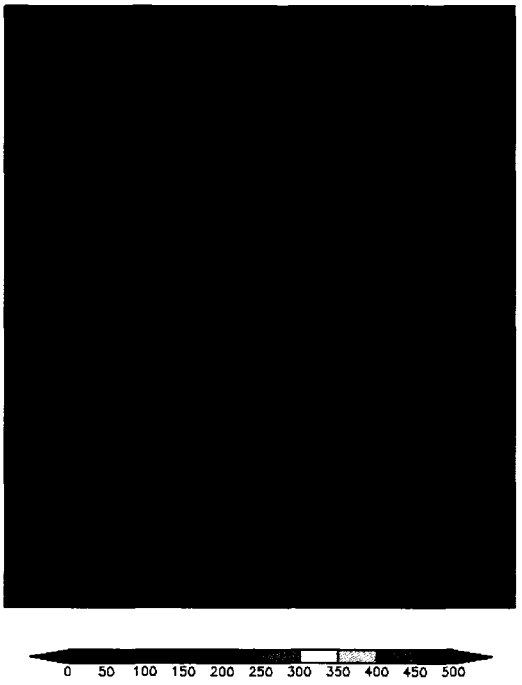

Figure 4.16 Sensible heat flux in W·m^{-2} at 2100 UTC.

By 2100 UTC, as seen in Figure 4.16, the values of sensible heat flux have decreased significantly as daytime heating decreases. Also, the effects of the disturbance induced by the differential heating have expanded in all directions. Greater extent of the disturbance is seen on the west side of the scar which shows the effect of the middle level winds. The maximum values continue to be over the northeastern portion of the scar with a magnitude of 190 W·m^{-2}, and the area of low values surrounding the burn scar has greatly expanded. This large region of lower values will be discussed further in the cloud water section.

4.2.4 Latent heat flux

The dry soil and lack of vegetation over the burn scar affects the latent heat flux over the region. As mentioned in Chapter 3, the burn scar soil moisture values are 0.15 in the three soil levels closest to the surface. The surrounding environment had soil moisture

Reproduced with permission of the copyright owner. Further reproduction prohibited without permission.

values of 0.40, 0.40, and 0.25 in those same three layers, which extend from the surface to 0.06 m below. The vegetation amount in the burn scar was reduced using the leaf area index (LAI) and setting it to 0.5 in the fire scar area and 6.0 in the surrounding area covered by tall grass.

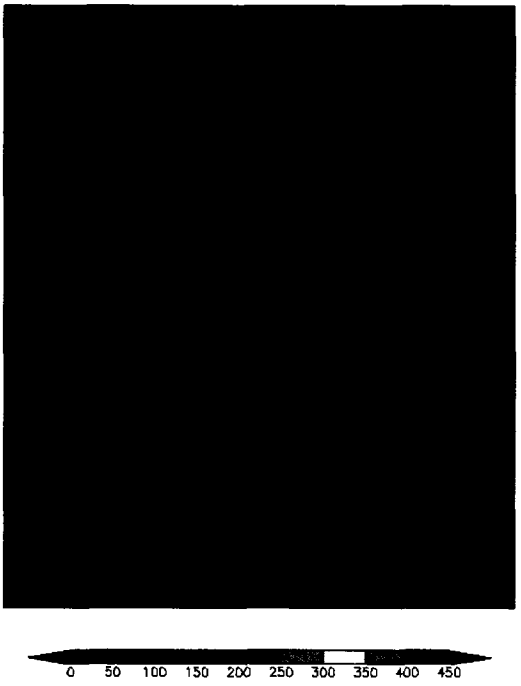

Figure 4.17 Latent heat flux at 1500 UTC.

As seen in Figure 4.17, at 1500 UTC, latent heat flux up to 130 $W \cdot m^{-2}$ is found over the area surrounding the burn scar, due to the greater amounts of vegetation and soil moisture. The burn scar region exhibits a latent heat flux between 30-50 $W \cdot m^{-2}$. The values over the surrounding area are significantly higher than seen in the sensible heat flux plot for the same time as shown in Figure 4.12.

Reproduced with permission of the copyright owner. Further reproduction prohibited without permission.

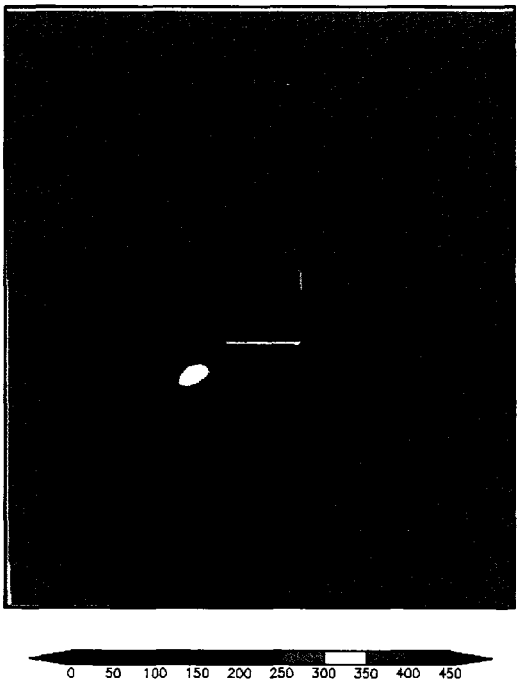

Figure 4.18 Latent heat flux at 1800 UTC.

At 1800 UTC, as seen in Figure 4.18, the latent heat flux over the burn scar is less than 50 $W \cdot m^{-2}$ compared to the surrounding area which now has a latent heat flux up to 390 $W \cdot m^{-2}$. While the magnitude of the flux over the burn scar has not changed significantly, the value over the surrounding area has almost tripled. This illustrates the effect of decreased transpiration due to the loss of vegetation. In addition there is a decrease in evaporation due to the lower soil moisture over the scar.

Reproduced with permission of the copyright owner. Further reproduction prohibited without permission.

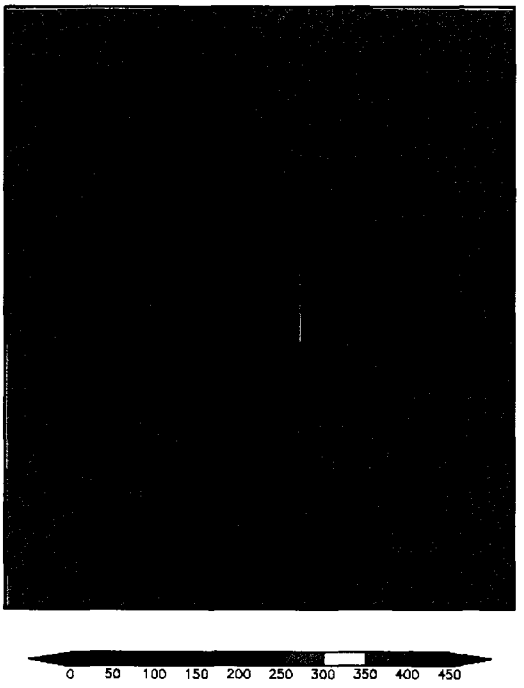

Figure 4.19 Latent heat flux at 1900 UTC.

Figure 4.19 shows the latent heat flux at 1900 UTC and similar values near 50 $W \cdot m^{-2}$ are predicted over the burn scar while values increased in the surrounding environment near the interface with the burn scar to 435 $W \cdot m^{-2}$. The amount of evapotranspiration occurring may have increased near the interface due to the stronger sensible heating over the burn scar.

Reproduced with permission of the copyright owner. Further reproduction prohibited without permission.

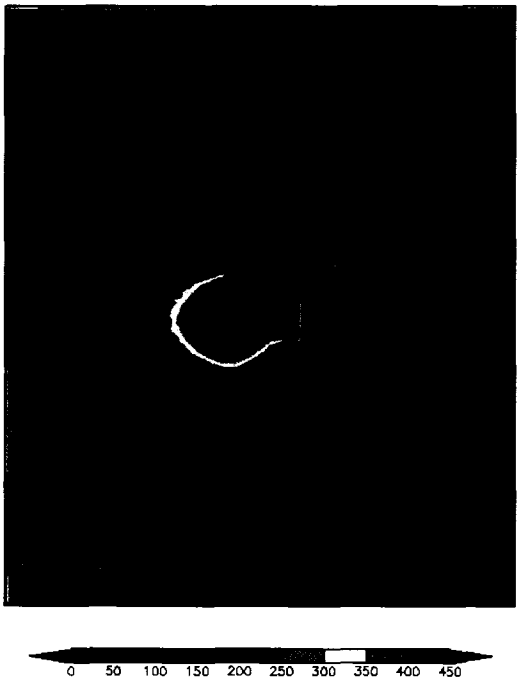

Figure 4.20 Latent heat flux at 2000 UTC.

By 2000 UTC, latent heat flux has increased to 450 $W \cdot m^{-2}$ over much of the surrounding region, while remaining nearly constant over the burn scar as seen in Figure 4.20. The effects of the disturbance induced by differential heating can be seen in the areas of lower latent heat fluxes to the south and west of the scar in the surrounding environment.

Reproduced with permission of the copyright owner. Further reproduction prohibited without permission.

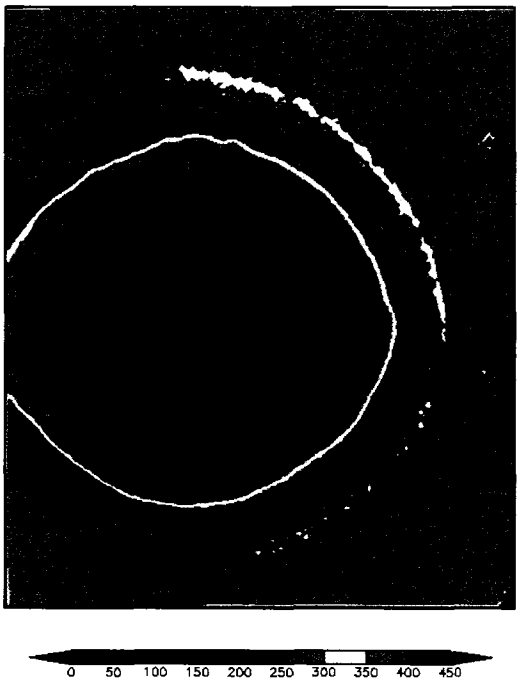

Figure 4.21 Latent heat flux at 2100 UTC.

Figure 4.21 shows latent heat flux at 2100 UTC, the effects of convection are widespread over the domain. While values over the burn scar have not changed significantly, the large region of lower values surrounding the burn scar can also be seen in the cloud water field at 2000 UTC in Figure 4.36. This correlation indicates the latent heat field is being affected by shading due to cloud cover. The higher values in the surrounding environment have also started to decrease to near 420 W·m-2.

4.2.5 Vertical velocity

A look at the vertical velocity field shows the effects of stronger heating over the burn scar. The field was evaluated by looking at the surface vertical velocity field and east-west cross sections taken through the burn scar.

Reproduced with permission of the copyright owner. Further reproduction prohibited without permission.

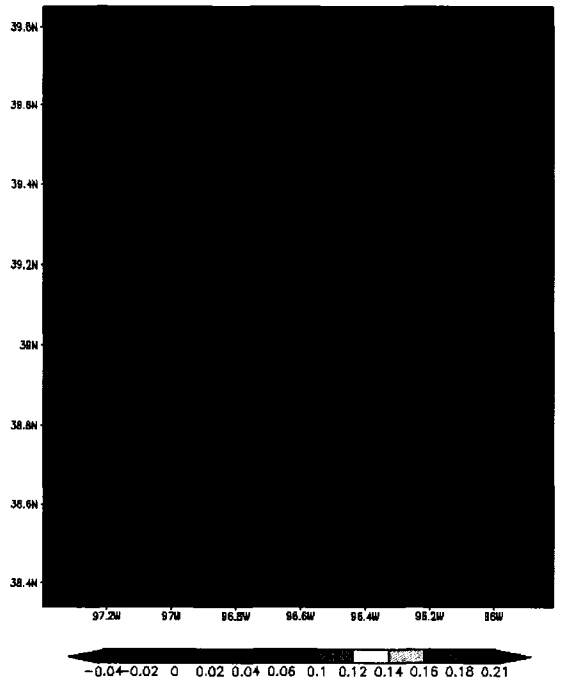

Figure 4.22 Vertical velocity at model level 1 (48 m) in $m \cdot s^{-1}$ at 1500 UTC.

Figure 4.22 shows that at 1500 UTC, weak upward and downward motion are visible. These values are on the order of a centimeter per second. Downward motion is stronger along the northern and eastern edges of the scar while upward motion is stronger along the southern and western edges. The highest upward vertical velocity of 0.018 $m \cdot s^{-1}$ occurs at the southwest corner of the scar with upward motion extending into the surrounding environment to the southwest of the scar.

Reproduced with permission of the copyright owner. Further reproduction prohibited without permission.

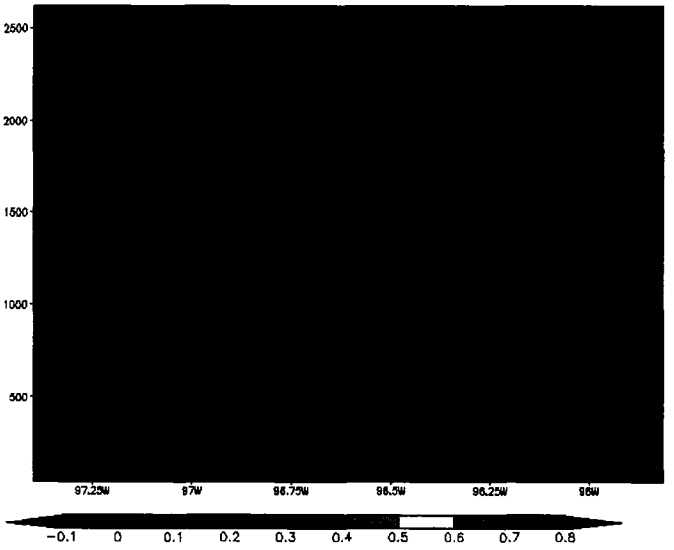

Figure 4.23 Cross section of vertical velocity in m·s^{-1} taken at 39.05°N at 1500 UTC.

Taking a west-east cross section through the burn scar at 1500 UTC, Figure 4.23 shows the vertical extent of the vertical velocity field. Although weak, values on the order of a few cm·s^{-1} have developed.

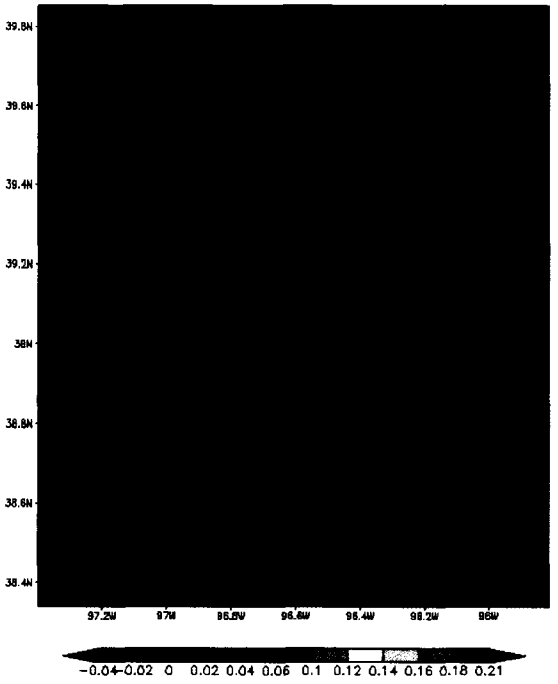

Figure 4.24 Vertical velocity at model level 1 (48 m) in m·s^{-1} at 1800 UTC.

Reproduced with permission of the copyright owner. Further reproduction prohibited without permission.

As the simulation continues, the strength of the vertical velocity associated with the burn scar increases to several centimeters per second and the spatial distribution continues to elongate toward the southwest. Figure 4.24 shows the vertical velocity field at the first model level (48 m) at 1800 UTC. Downward motion continues along the northern and eastern edges of the scar, and upward motion along the southern and western edges and over most of the burn scar region. The strongest upward motion continues to be anchored at the southwest corner of the scar with a maximum value of 0.1 $m \cdot s^{-1}$. The extension of the upward motion to the southwest follows the prevailing low-level wind field depicted in Figure 4.8.

The upward motion is stronger than the downward motion. The upward motion is more concentrated over the burn scar and slightly downwind while the downward motion is more widely distributed. This is better depicted in the east-west vertical cross section through the burn scar at 39.05°N. Figure 4.25 shows this cross section at 1800 UTC.

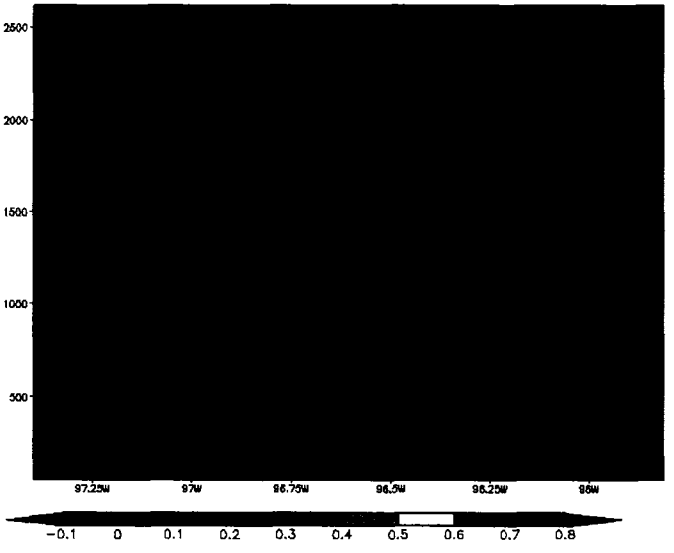

Figure 4.25 Cross section of vertical velocity in $m \cdot s^{-1}$ taken at 39.05°N at 1800 UTC.

Reproduced with permission of the copyright owner. Further reproduction prohibited without permission.

To examine how the vertical velocity field evolves with time, vertical cross sections are presented every ten minutes of simulation time in Figure 4.26. Between 1810 UTC and 1840 UTC, the region of upward motion expands slightly and increases in intensity. The area of strongest upward motion is seen near 400 m initially and then lifts to near 600 m.

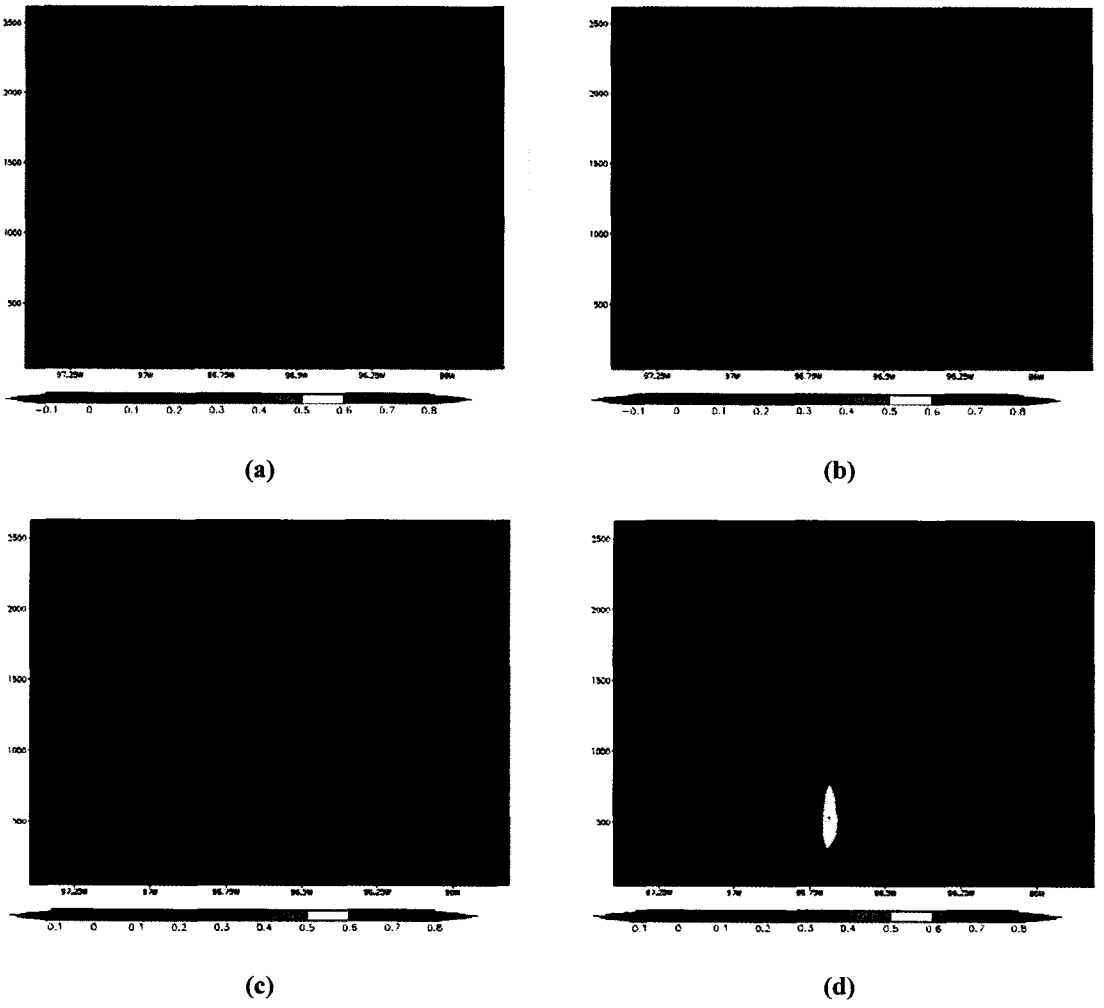

Figure 4.26 Cross section of vertical velocity in m s^{-1} taken at 39.05°N at (a) 1810, (b) 1820, (c) 1830, (d) 1840 UTC.

Reproduced with permission of the copyright owner. Further reproduction prohibited without permission.

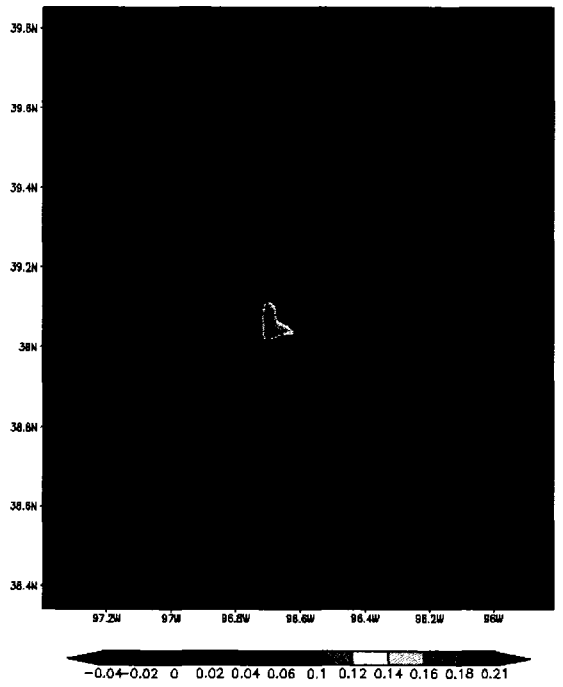

Figure 4.27 Vertical velocity at model level 1 (48 m) in m s^{-1} at 1900 UTC.

Figure 4.27 shows the vertical velocity distribution at 1900 UTC. The strongest upward velocity, 0.18 $m \cdot s^{-1}$, is in the southwestern portion of burn scar area. The corresponding downward velocity is much weaker with the strongest values being 0.05 $m \cdot s^{-1}$.

Reproduced with permission of the copyright owner. Further reproduction prohibited without permission.

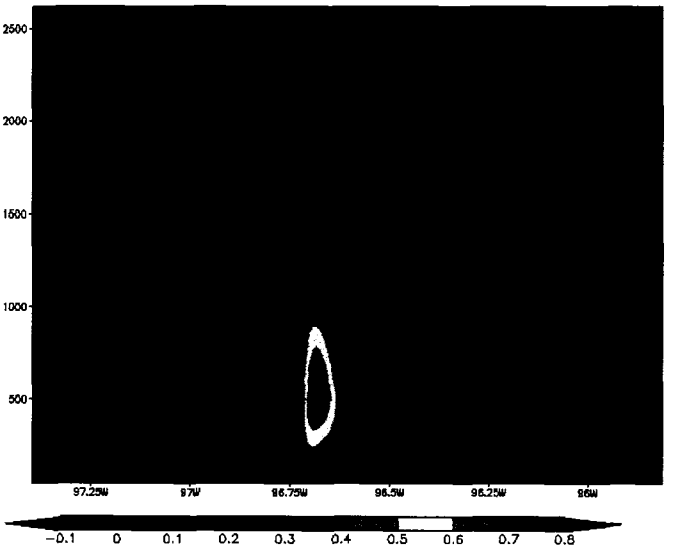

Figure 4.28 Cross section of vertical velocity in m s^{-1} taken at 39.05°N at 1900 UTC.

The cross section at 1900 UTC in Figure 4.28 shows the strongest upward velocity is centered near 600 m and is 0.7 $m \cdot s^{-1}$. The downward motion is much weaker, near 0.1 $m \cdot s^{-1}$, and more widespread than the upward motion.

Reproduced with permission of the copyright owner. Further reproduction prohibited without permission.

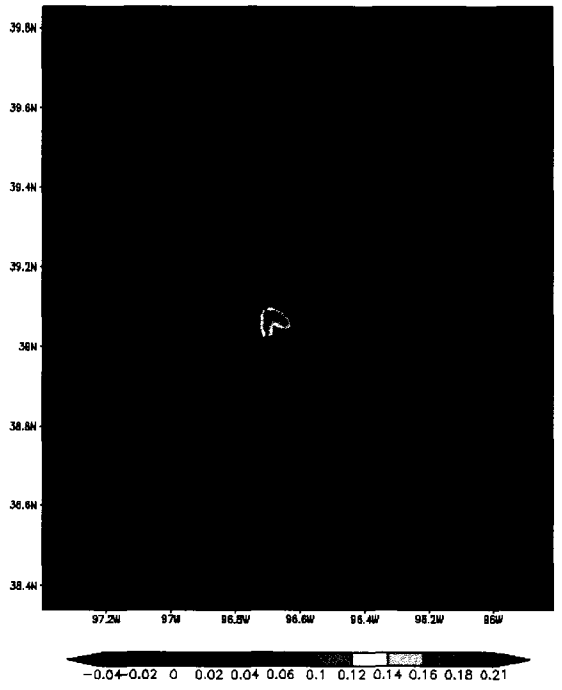

Figure 4.29 Vertical velocity at model level 1 (48 m) in m s^{-1} at 2000 UTC.

By 2000 UTC, the disturbance induced by the difference in surface characteristics is reflected in the vertical velocity field depicted in Figure 4.29. The strongest upward motion of 0.17 $m \cdot s^{-1}$ is still concentrated near the southwest corner of the burn scar. Flanking the burn scar are regions of stronger downward motion, although still substantially weaker with maximum values of 0.04 $m \cdot s^{-1}$. On the western edge of the burn scar, the region of downward motion has begun wrapping around the western edge of the area of strong upward motion. Radiating from this concentrated area are rings of alternating upward and downward motion.

Reproduced with permission of the copyright owner. Further reproduction prohibited without permission.

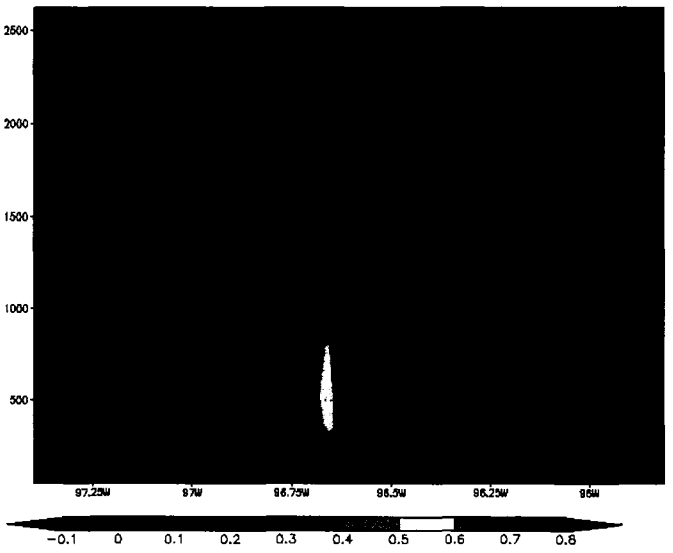

Figure 4.30 Cross section of vertical velocity in m s^{-1} taken at 39.05°N at 2000 UTC.

The vertical cross-section at 2000 UTC shows the maximum upward motion between 500 and 600 m of 0.5 $m \cdot s^{-1}$. Downward motion is seen flanking the upward cell and just above and to the west between 1000 m and 2500 m with values of 0.1 $m \cdot s^{-1}$. The rings of upward and downward motion are also seen across the slice.

4.2.6 Cloud Water

After almost seven hours into the simulation, two layers of clouds form over the region of highest upward velocity. This is in response to the heating over the burn scar.

Reproduced with permission of the copyright owner. Further reproduction prohibited without permission.

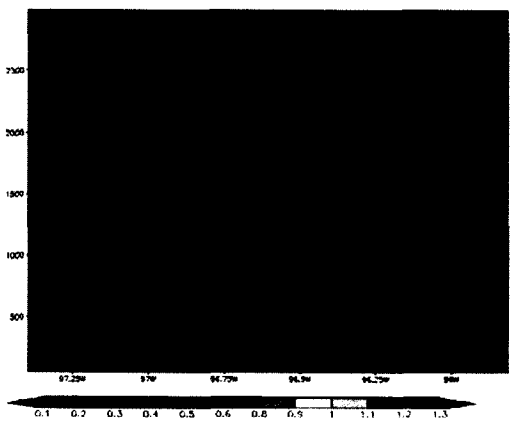

Figure 4.31 Vertical cross section of cloud water at 39.05 N in g·kg^{-1} at 1850 UTC.

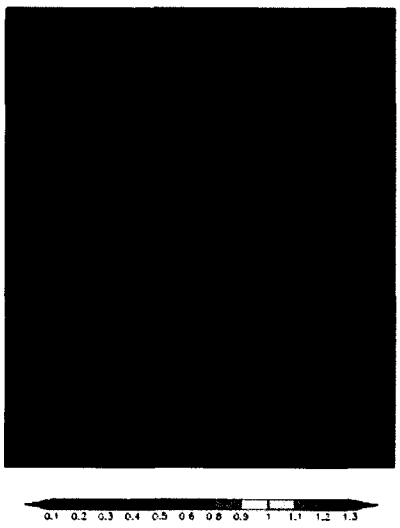

Figure 4.32 Cloud water at model level 13 (2292 m) in g·kg^{-1} at 1850 UTC.

At 1850 UTC, two levels of cloud can be seen in the cloud water distribution, in Figure 4.31. This vertical cross-section was taken along 39.05°N. The upper level is centered near 2000 m with values near 0.3 g·kg^{-1}, and the lower level near 1000 m with values over 0.35 g·kg^{-1}. The tops of the clouds are near 2500 m which shows the effects of the inversion seen near that level in the initialization sounding shown in Figure 3.2. The horizontal distribution of cloud water at model level 13 (2292 m) in Figure 4.32 shows a crescent shaped region near the western edge of the burn scar at 1850 UTC.

Reproduced with permission of the copyright owner. Further reproduction prohibited without permission.

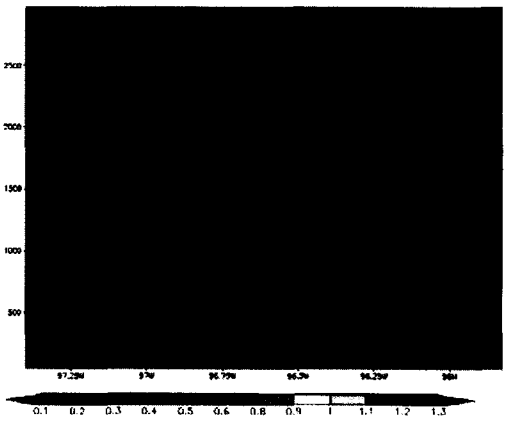

Figure 4.33 Vertical cross section of cloud water at 39.05 N in g·kg^{-1} at 1930 UTC.

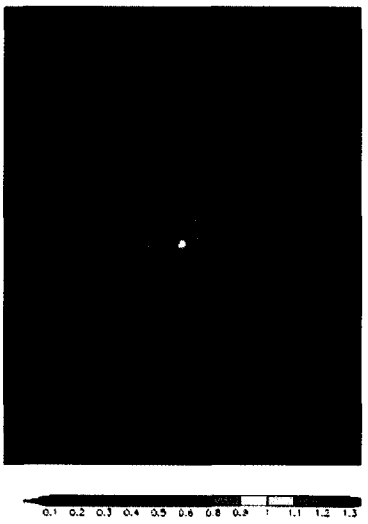

Figure 4.34 Cloud water at model level 13 (2292 m) in g·kg^{-1} at 1930 UTC. The burn scar location is outlined.

As the simulation continued, the cloud areas expanded horizontally. Figure 4.33 shows the vertical cross-section of cloud water plotted at 1930 UTC. The upper level shows greater expansion with values exceeding 0.8 g·kg^{-1} near 2300 m. The lower level of cloud has also expanded with values exceeding 0.6 g·kg^{-1}. The plan view at 1930 UTC of cloud water at model level 13 (2292 m) in Figure 4.34, shows the region of cloud water has expanded horizontally. The highest values of greater than 0.9 g·kg^{-1} are located over the burn scar and correspond to the area of strongest upward motion.

Reproduced with permission of the copyright owner. Further reproduction prohibited without permission.

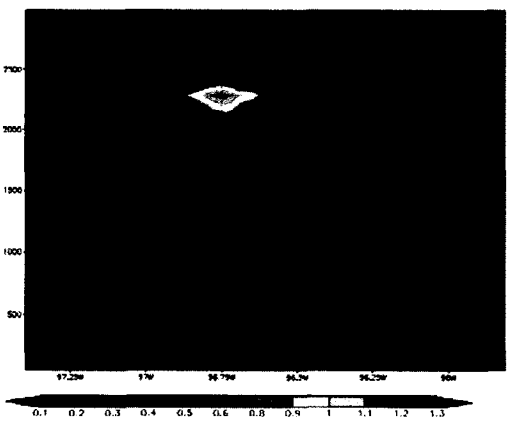

Figure 4.35 Vertical cross section of cloud water at 39.05 N in g·kg^{-1} at 2000 UTC.

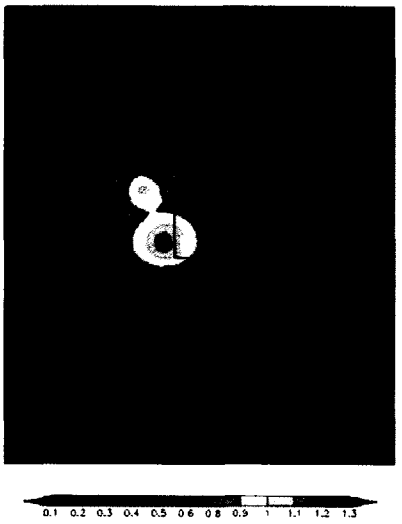

Figure 4.36 Cloud water at model level 13 (2292 m) in g·kg^{-1} at 2000 UTC.

At 2000 UTC, as seen in Figure 4.35, the cloud water field has continued to expand to most of the western portion of the domain with maximum values over 1.1 g·kg^{-1}. The largest values are near the burn scar. The lower cloud layer remains near 1000 m with cloud water values over 0.6 g·kg^{-1}.The cloud water field at 2000 UTC in Figure 4.36 shows a widespread area of cloud over the domain. The pattern matches the disturbance in the surface temperature and sensible heat fields at 2100 UTC showing the cooling effects of shading the region. The concentrated region of higher values, over 1.1 g·kg^{-1}, is linked to the burn scar area.

4.2.7 Soundings

Soundings were examined to evaluate changes in the atmosphere over the burn scar. Side by side comparisons were done with profiles taken over the burn scar in the region of greatest vertical motion and over the surrounding environment.

Reproduced with permission of the copyright owner. Further reproduction prohibited without permission.

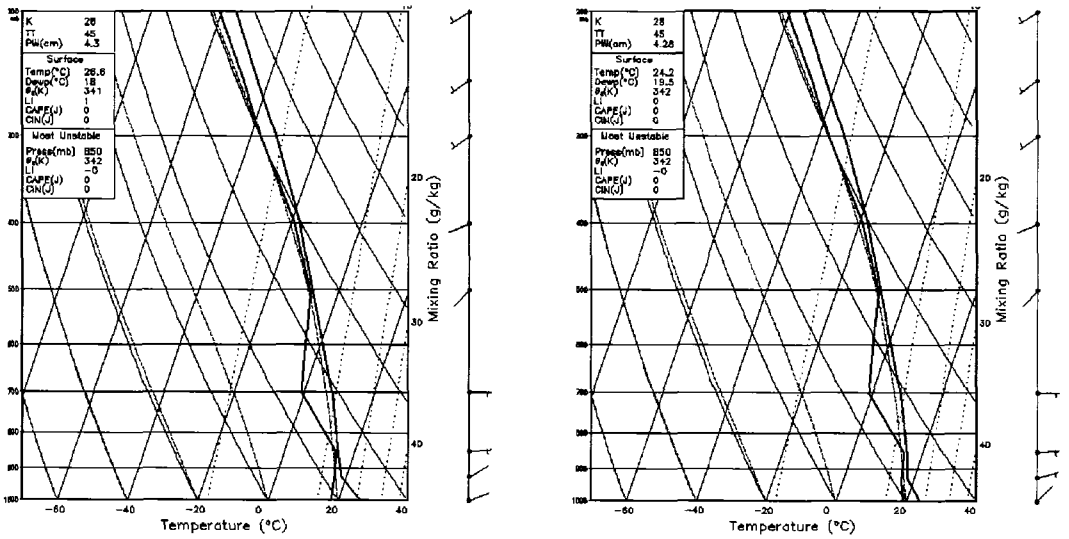

(a) (b)

Figure 4.37 Vertical sounding of the atmosphere taken at 1800 UTC over (a) the burn scar and (b) the surrounding environment.

At 1800 UTC, subtle differences can be seen in the two soundings depicted in Figure 4.37. The warmer and drier conditions are apparent at the surface, with a well mixed layer seen near the surface over the burn scar. The wind field shows some differences, but nothing of significance.

Reproduced with permission of the copyright owner. Further reproduction prohibited without permission.

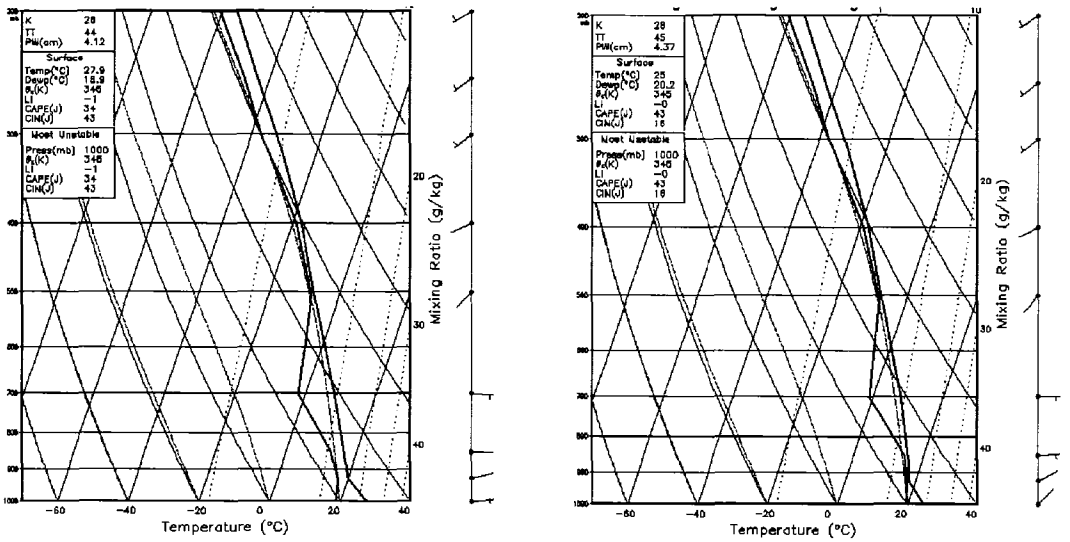

(a) (b)

Figure 4.38 Vertical sounding of the atmosphere taken at 1900 UTC over (a) the burn scar and (b) the surrounding environment.

By 1900 UTC, the surface characteristics over the burn scar continue to show warmer and drier conditions over the burn scar. However, the atmosphere over the entire domain continues to be very stable with CAPE values less than 50 $J \cdot kg^{-1}$. The CAPE and CIN values show greater differences with time, with the area over the surrounding environment appearing more convectively unstable.

Reproduced with permission of the copyright owner. Further reproduction prohibited without permission.

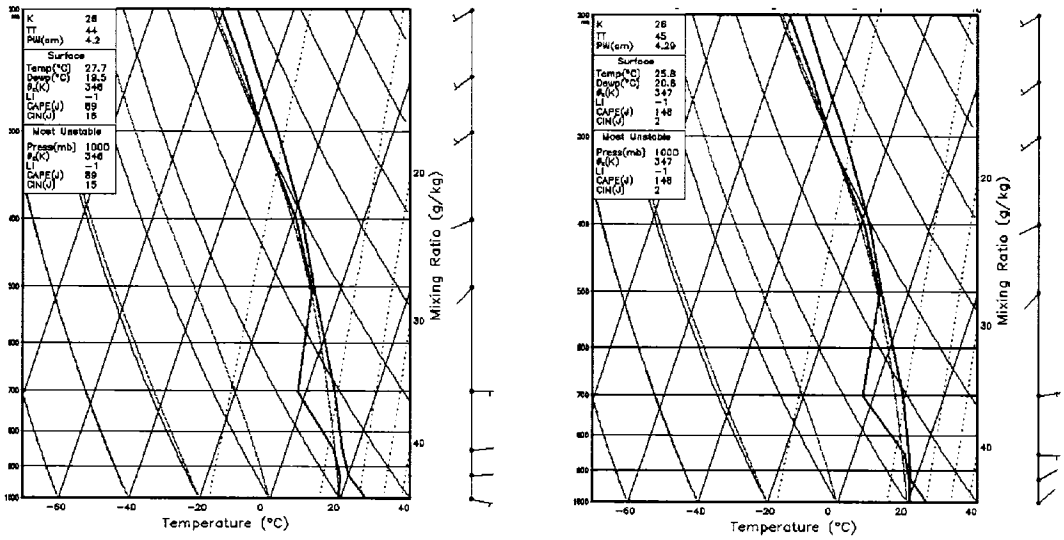

(a) (b)

Figure 4.39 Vertical sounding of the atmosphere taken at 2000 UTC over (a) the burn scar and (b) the surrounding environment.

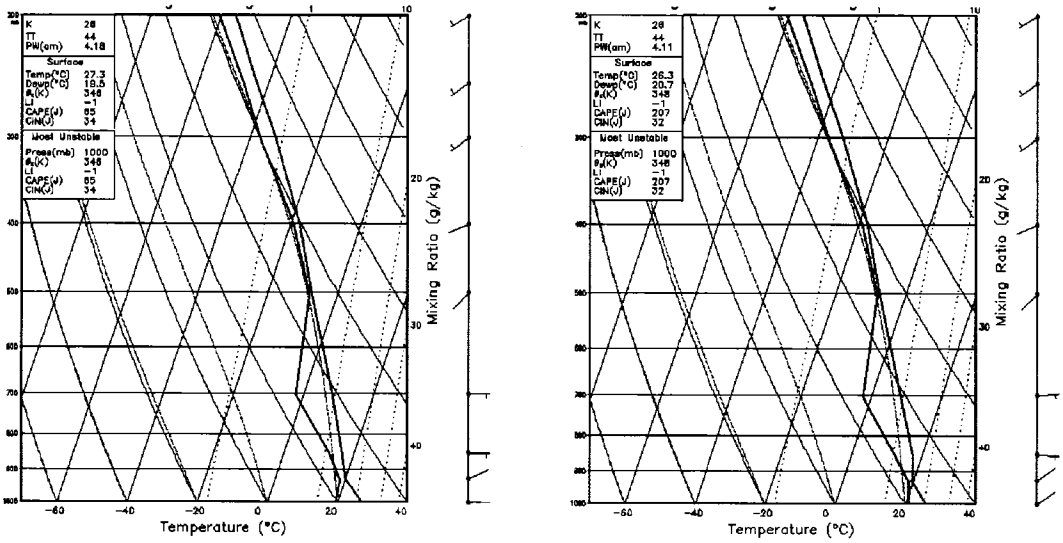

(a) (b)

Figure 4.40 Vertical sounding of the atmosphere taken at 2100 UTC over (a) the burn scar and (b) the surrounding environment.

Reproduced with permission of the copyright owner. Further reproduction prohibited without permission.

4.3 Warm Bubble Experiment

The next step is to look at the effect of the burn scar on pre-existing convection. This simulation is an extension of the previous experiment and is designed to analyze the effects of the modified environment on pre-existing convection. To model pre-existing convection, a warm bubble was introduced in the domain at 1900 UTC. The evolution of the storm is then examined. To further investigate the effects, the same convective cell was placed in an environment without the burn scar.

4.3.1 Warm Bubble Experiment over Burn Scar

To test the effects of the burn scar on development of convection, the warm, moist bubble was placed in the southwest corner of the burn scar near the region of strongest updraft implied in Figure 4.27 which shows the vertical velocity at 1900 UTC.

Reproduced with permission of the copyright owner. Further reproduction prohibited without permission.

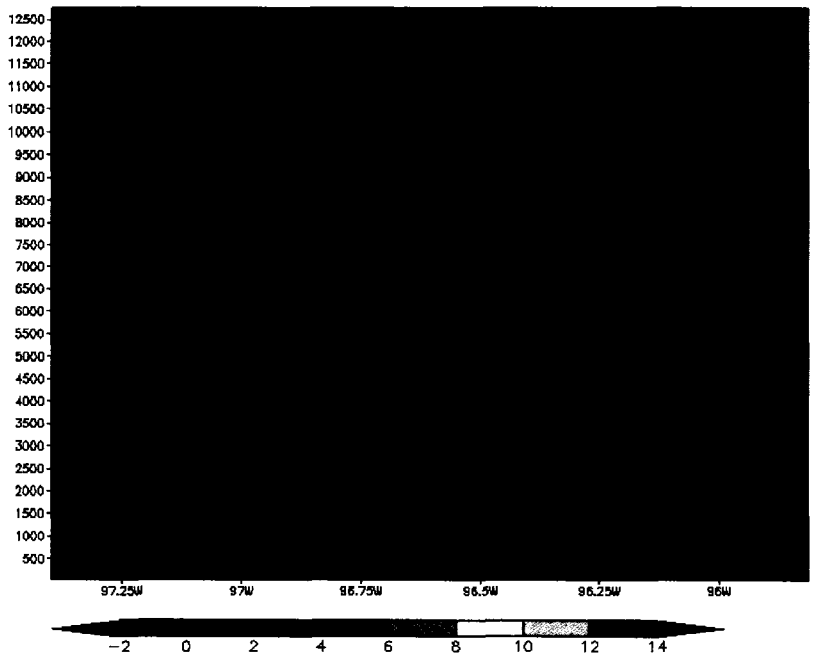

Figure 4.41 Vertical Cross-section of vertical velocity at 39.05 N at 1905 UTC for the warm bubble experiment over the southwestern portion of the burn scar.

The vertical velocity at 1905 UTC, five minutes after the bubble was released, is presented in Figure 4.41 as a cross-section through the center of the bubble at latitude of 39.05 N. This can be compared to the vertical velocity induced by the burn scar alone at 1900 UTC shown in Figure 4.28. The magnitude of the vertical velocity is substantially stronger and extends to a higher level in the atmosphere in the bubble experiment than in the simulation with just the burn scar. The perturbation introduced by the bubble extends up to the vertical model level 15 (2980 m).

Reproduced with permission of the copyright owner. Further reproduction prohibited without permission.

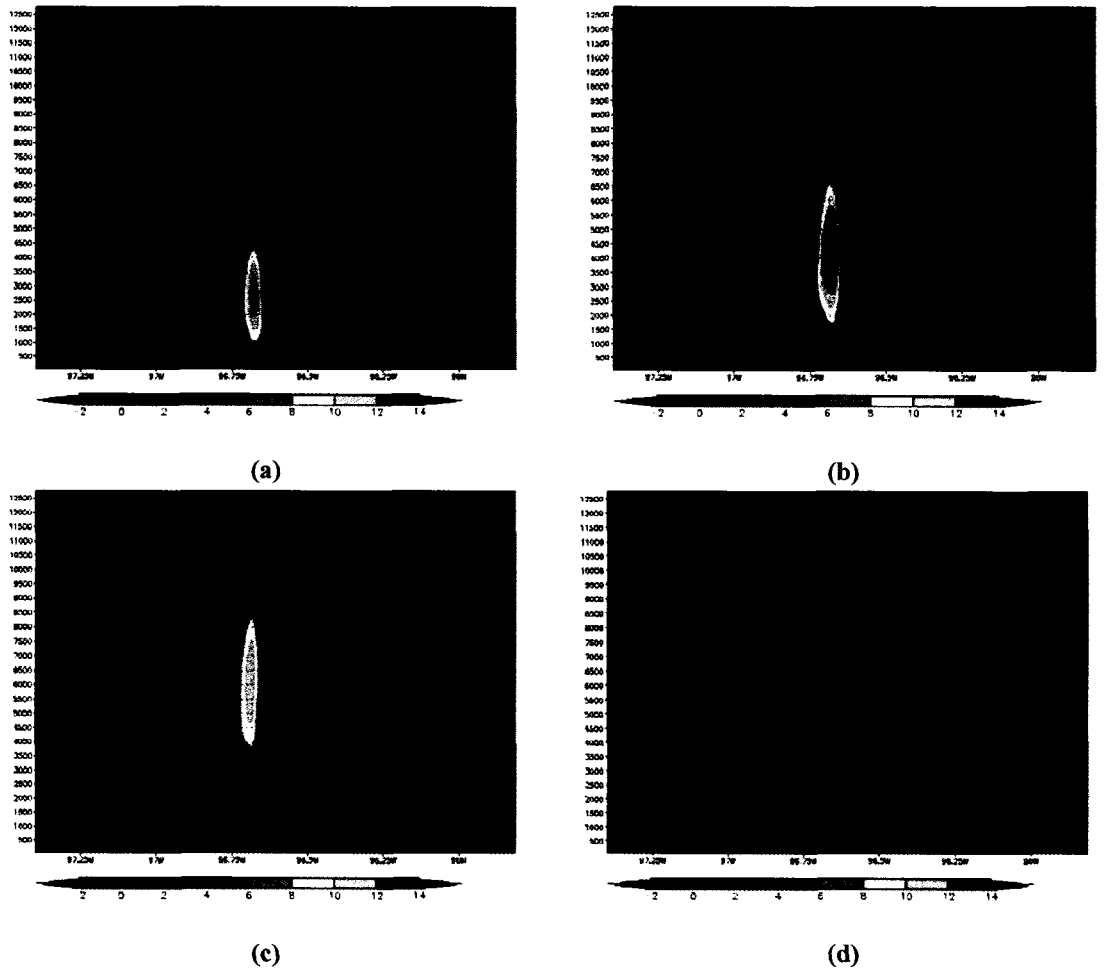

Figure 4.42 Vertical Cross-section of vertical velocity at 39.05 N at (a) 1910 UTC, (b) 1915 UTC, (c) 1920 UTC, (d) 1925 UTC for the warm bubble experiment over the southwestern portion of the burn scar.

The evolution of the bubble in the vertical velocity field is shown in Figure 4.42 over the time period from 1910 UTC to 1925 UTC. The region of upward motion associated with the bubble increases in strength up to 1915 UTC (fifteen minutes after the bubble was released) and begins to elongate and lift higher in the atmosphere. By 1925 UTC, the upward motion has lifted to between 4000 m and 11000 m while weaker downward motion forms from the surface up to 4000 m.

Reproduced with permission of the copyright owner. Further reproduction prohibited without permission.

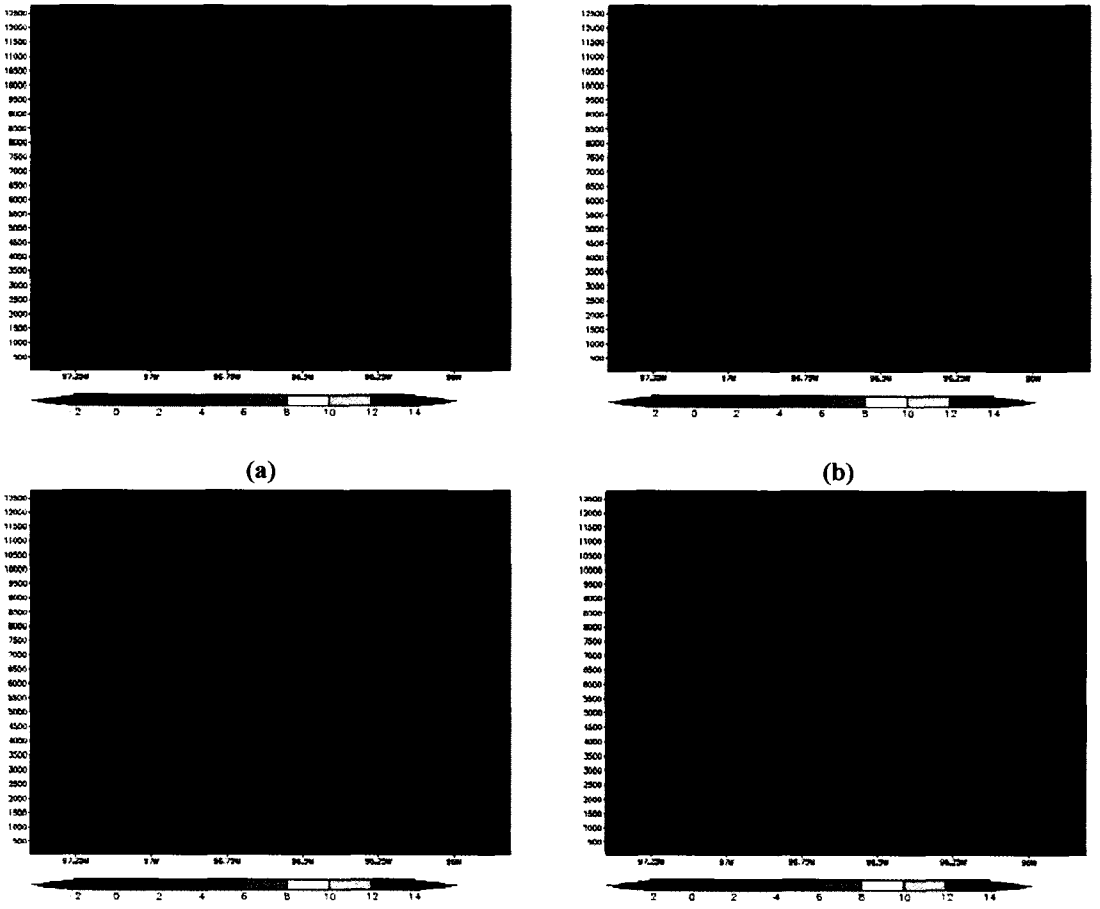

(a) (b)

(c) (d)

Figure 4.43

Figure 4.44 Vertical Cross-section of vertical velocity at 39.05 N at (a) 1930 UTC, (b) 1935 UTC, (c) 1940 UTC, (d) 1945 UTC for the warm bubble experiment over the southwestern portion of the burn scar.

Figure 4.44 shows the continuing evolution of the vertical velocity field from 1930 UTC to 1945 UTC. The lifting of the region of upward motion induced by the bubble ends as the strength of the lift weakens. The downward motion below this area also weakens.

Reproduced with permission of the copyright owner. Further reproduction prohibited without permission.

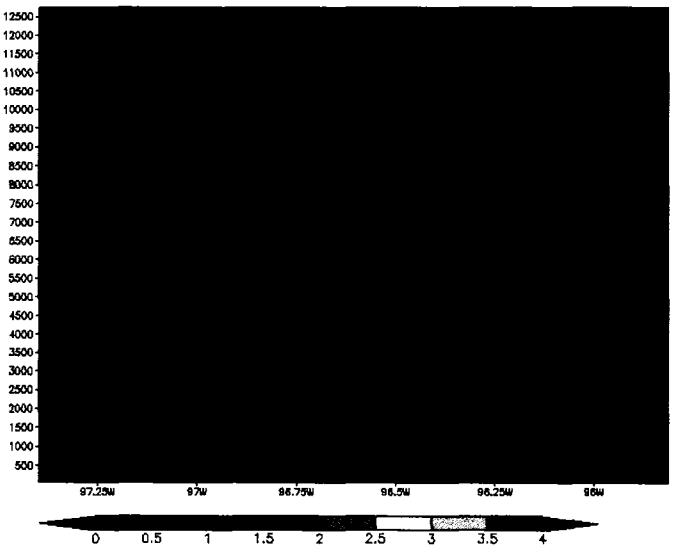

Figure 4.45 Vertical Cross-section of cloud water at 39.05 N at 1905 UTC for the warm bubble experiment over the southwestern portion of the burn scar.

The effect of the upward motion associated with the burn scar is seen in Figure 4.45, which shows a vertical cross-section in the cloud water field, and can be compared to that induced by the burn scar and presented in Figure 4.31, which shows the cloud field at 1850 UTC induced by the burn scar alone, at the time that it was first observed.

Reproduced with permission of the copyright owner. Further reproduction prohibited without permission.

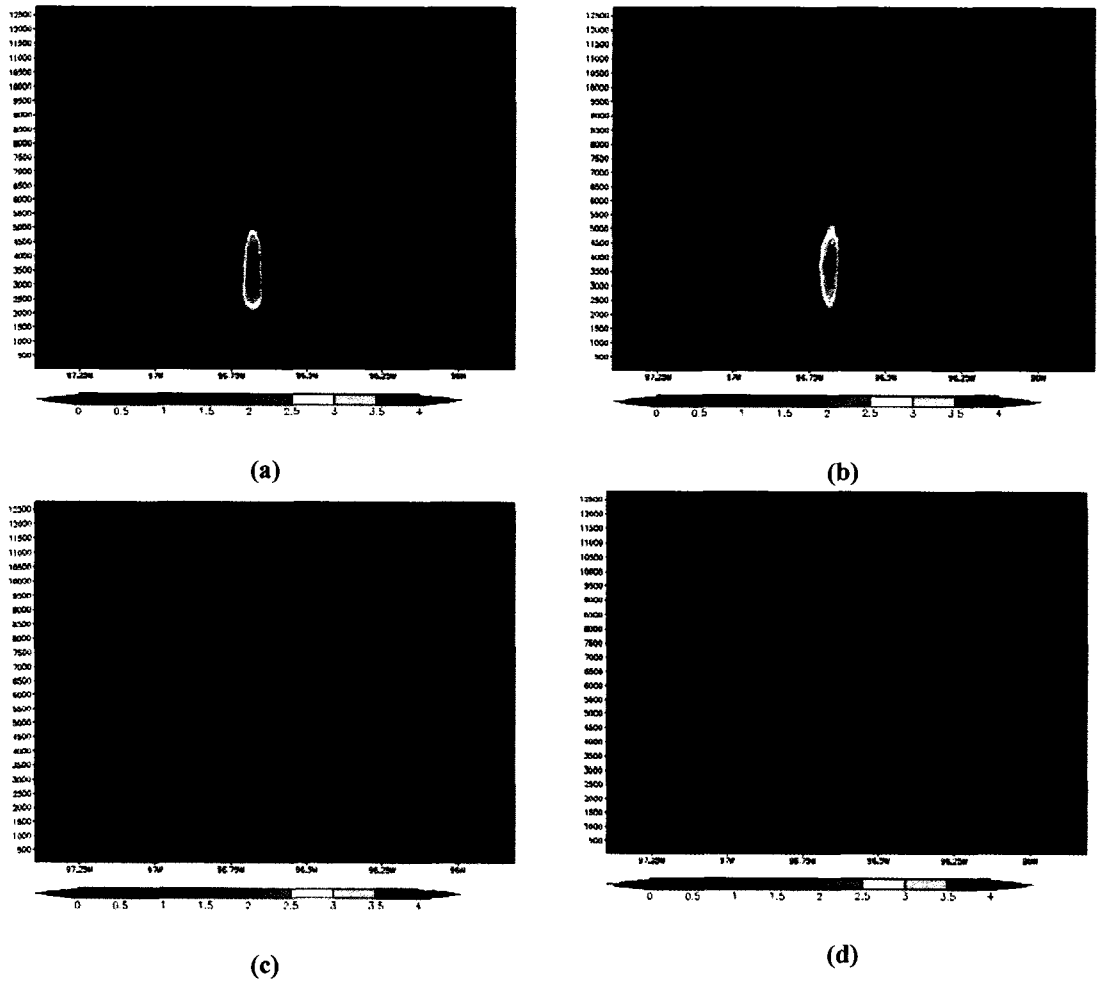

Figure 4.46 Vertical Cross-section of cloud water at 39.05 N at (a) 1910 UTC, (b) 1915 UTC, (c) 1920 UTC, (d) 1925 UTC for the warm bubble experiment over the southwestern portion of the burn scar.

The evolution of the cloud field due to the bubble is shown in Figure 4.46. The cloud field shows a deep, but narrow region of cloud at 1910 UTC extending from 1000 m to 5500 m. The maximum value of 4 $g \cdot kg^{-1}$ is seen between 3000 m and 4000 m. By 1915 UTC, the cloud field extends up to 7000 m with the region of 4 $g \cdot kg^{-1}$ values decreasing in size. By 1920 UTC, cloud begins to form between 2000 m and 2500 m as the upper region of cloud begins to dissipate. At 1925 UTC the effects of the downward motion below 3000 m are seen in the cloud field.

Reproduced with permission of the copyright owner. Further reproduction prohibited without permission.

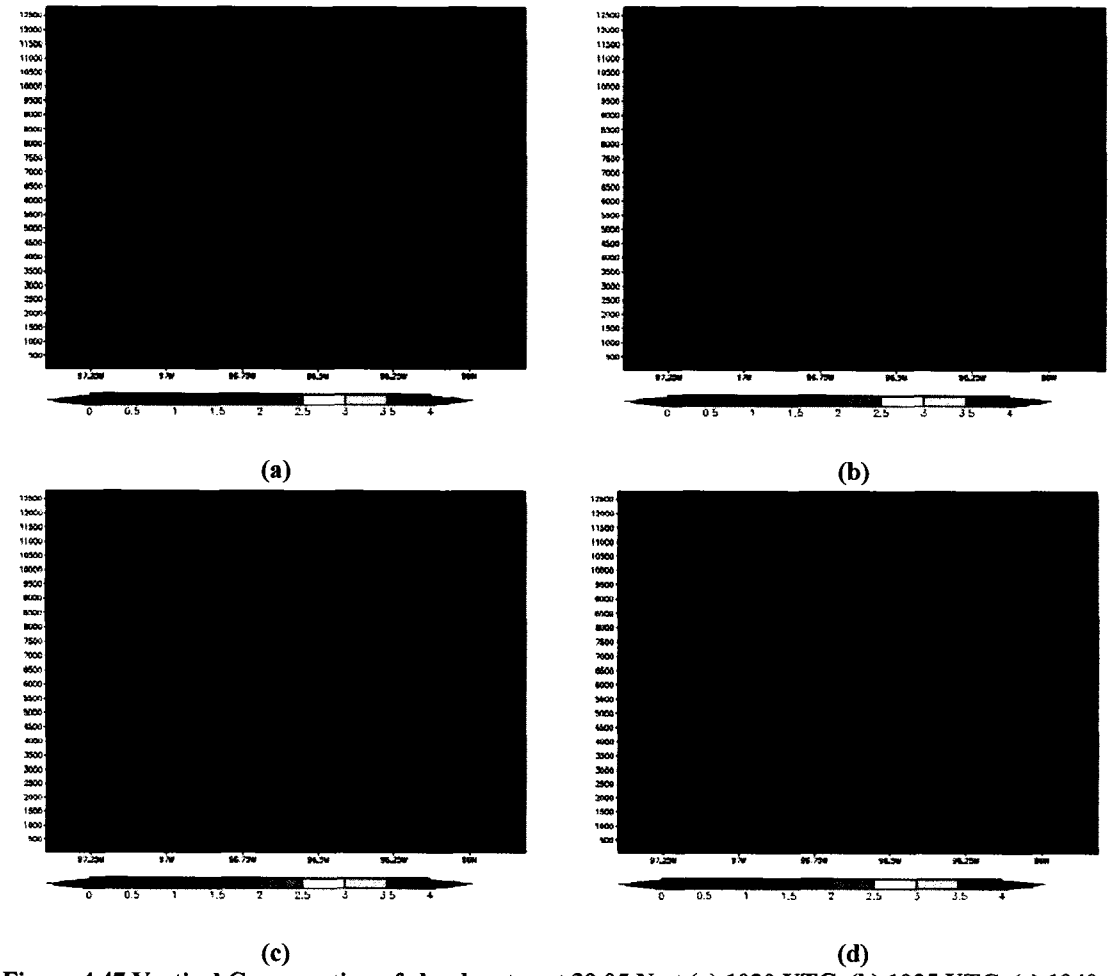

Figure 4.47 Vertical Cross-section of cloud water at 39.05 N at (a) 1930 UTC, (b) 1935 UTC, (c) 1940 UTC, (d) 1945 UTC for the warm bubble experiment over the southwestern portion of the burn scar.

Remnants of the bubble induced cloud are seen through the next 15 minutes of simulation time, while the cloud between 2000 m and 2500 m continues to spread to cover a greater portion of the domain. The continued downward motion between 2000m and 4000 m keeps that region cloud-free through 1945 UTC. Comparing the cloud water cross-section in Figure 4.47(a) to the simulation without the bubble in Figure 4.33, shows cloud still occurred in the same location in the bubble experiment as in the original experiment. In the bubble experiment, a clear region in the two cloud layers where the bubble was released, and a third region of cloud developed between 4000 m and 4500 m.

Reproduced with permission of the copyright owner. Further reproduction prohibited without permission.

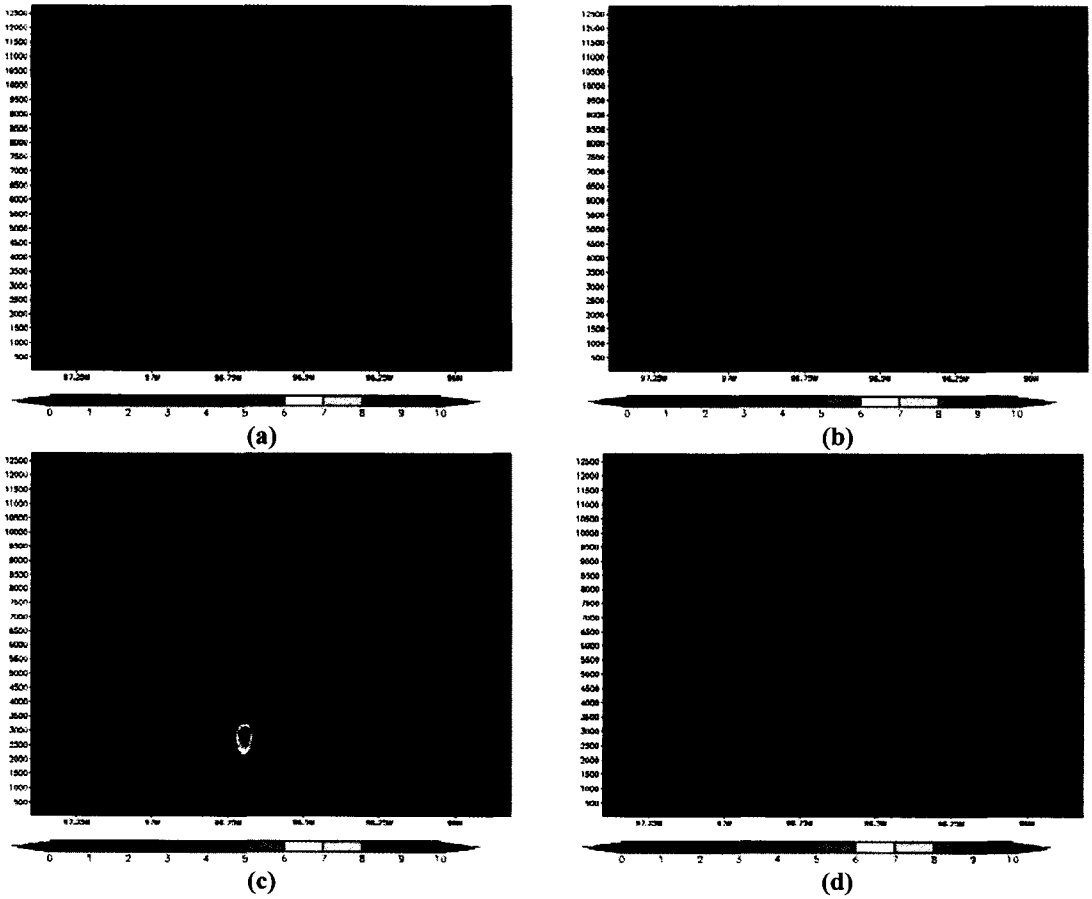

Figure 4.48 Vertical Cross-section of rain water at 39.05 N at (a) 1910 UTC, (b) 1915 UTC, (c) 1920 UTC, (d) 1925 UTC for the warm bubble experiment over the southwestern portion of the burn scar.

The next field examined was rain water induced in the bubble. At 1910 UTC, values of rain water in the bubble region between 1500 m and 5200 m were near 0.2 $g \cdot kg^{-1}$. By 1915 UTC, the rain water area lifted to between 3000 m and 6200 m, and the values within the area have increased substantially to 3.5 $g \cdot kg^{-1}$. Five minutes later, at 1920 UTC, the region of rain water has now dropped in elevation to between 1000 m and 4000 m with ever higher values up to a maximum of 10 $g \cdot kg^{-1}$. By 1925 UTC, the rain area begins to decrease in concentration and expands in vertical extent from 3500 m to the surface. Values have decreased to 5.5 $g \cdot kg^{-1}$.

Reproduced with permission of the copyright owner. Further reproduction prohibited without permission.

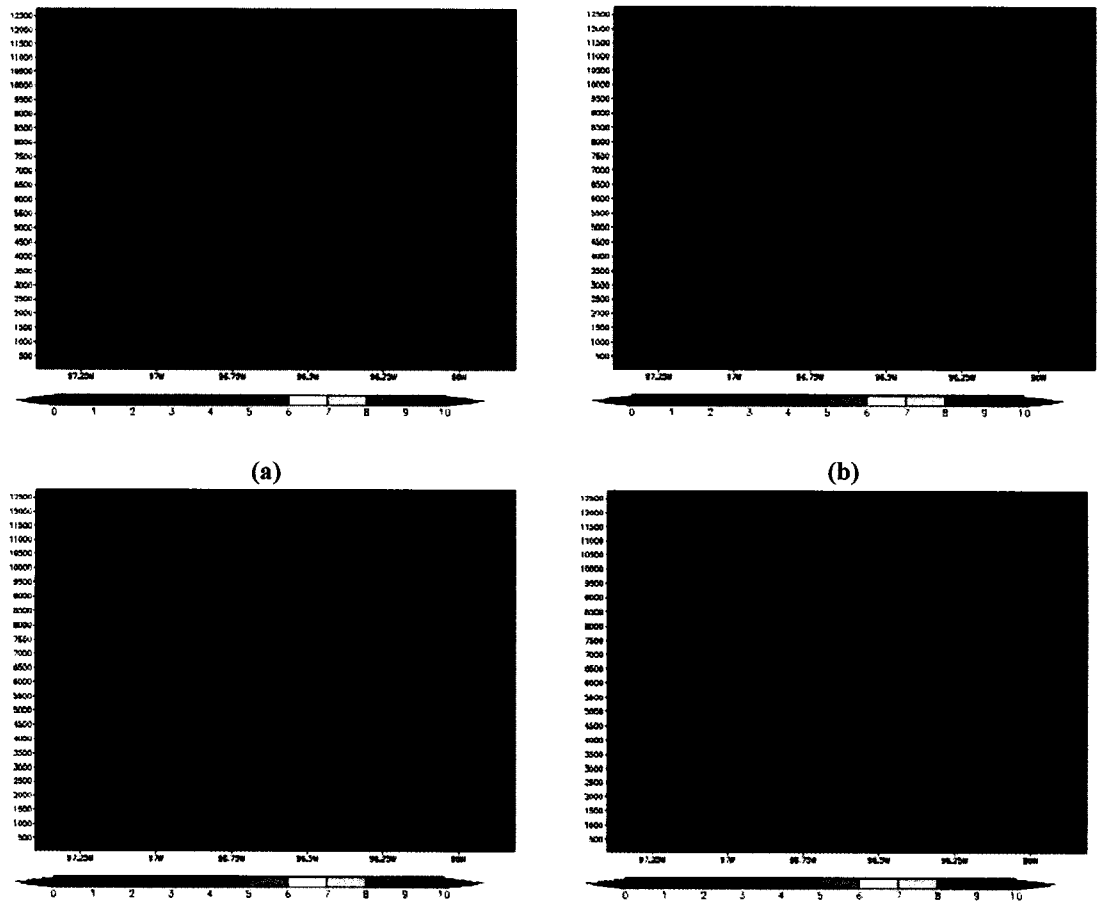

(a) (b)

(c) (d)

Figure 4.49 Vertical Cross-section of rain water at 39.05 N at (a) 1930 UTC, (b) 1935 UTC, (c) 1940 UTC, (d) 1945 UTC for the warm bubble experiment over the southwestern portion of the burn scar.

Figure 4.49 shows the cross-section of rain water between 1930 UTC and 1945 UTC. By 1930 UTC, as seen in part (a), the rain water is below 3300 m and the concentration has decreased values below 2.4 $g \cdot kg^{-1}$. Five minutes later, at 1935 UTC, the rain water region resurges up to 3800 m with values as high as 0.6 $g \cdot kg^{-1}$ as seen in part (b). The area again decreases in concentration at 1940 UTC as seen in part (c) and continues to decrease by 1945 UTC as seen in part (d).

Reproduced with permission of the copyright owner. Further reproduction prohibited without permission.

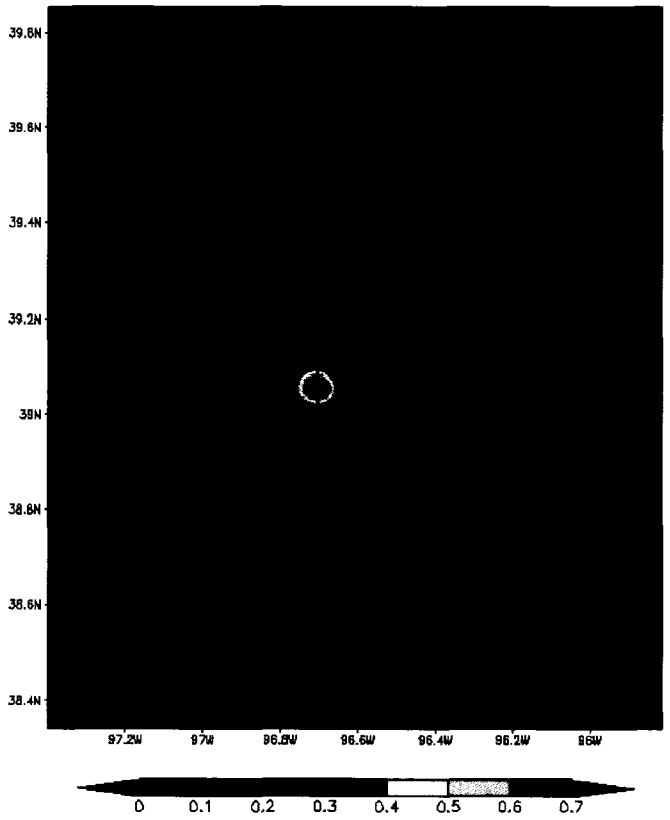

Figure 4.50 Total precipitation predicted at the surface in inches at 2000 UTC.

Total precipitation predicted by 2000 UTC is shown in Figure 4.50 with the outline of the burn scar indicated. By that time the precipitation had stopped and the maximum value predicted was 0.75 inches. The precipitation area covers a region along the southwestern border of the burn scar.

Reproduced with permission of the copyright owner. Further reproduction prohibited without permission.

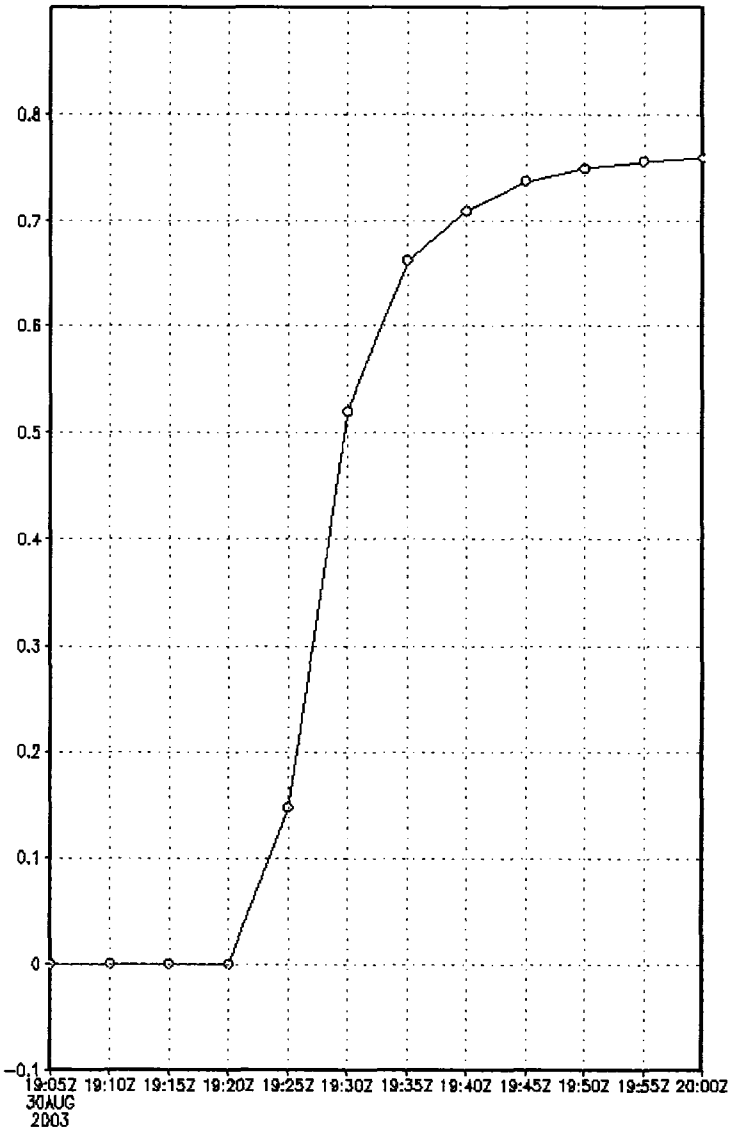

Figure 4.51 Total precipitation as a function of time for the bubble release over the burn scar experiment from 1905 UTC to 2000 UTC 30 August 2003.

To see the evolution of precipitation with time, the amount of precipitation at the ground was plotted (Figure 4.51) for the grid point over which the heaviest rain fell. This location was along the edge of the burn scar, near 96.71 W and 39.05 N, as can be seen in Figure 4.50. Rain was predicted at the surface by 1920 UTC, 20 minutes after the bubble was released. The heaviest rates were seen between 1920 UTC and 1935 UTC. A steady

Reproduced with permission of the copyright owner. Further reproduction prohibited without permission.

drop in precipitation occurring from 1935 to 2000 UTC, after which the amount of precipitation over that grid point was negligible.

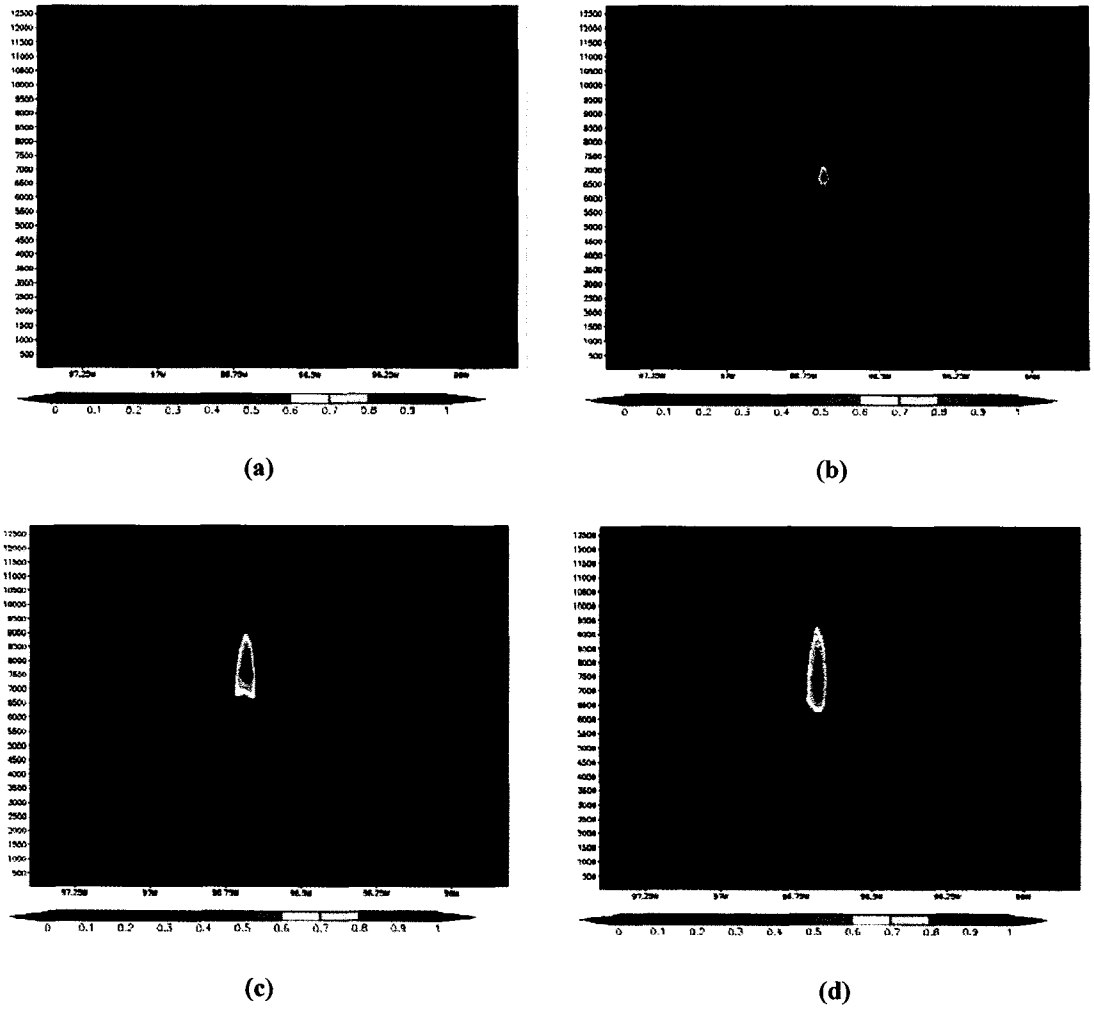

Figure 4.52 Vertical Cross-section of graupel mixing ratio in g·kg^{-1}at 39.05 N at (a) 1910 UTC, (b) 1915 UTC, (c) 1920 UTC, (d) 1925 UTC for the warm bubble experiment over the southwestern portion of the burn scar.

Figure 4.52 shows the mixing ratio of graupel in g·kg^{-1} through the bubble released over the burn scar from 1910 UTC to 1925 UTC. As seen in sections (a) and (b), significant amounts of graupel develop in the bubble region with values up to 0.9 g·kg^{-1}.

Reproduced with permission of the copyright owner. Further reproduction prohibited without permission.

The region continues to expand and lift by 1920 UTC (c) with similar concentrations, and the region of largest concentrations increases by 1925 UTC (d). This field will be analyzed as an indicator of electrification of the cloud and lightning producing potential.

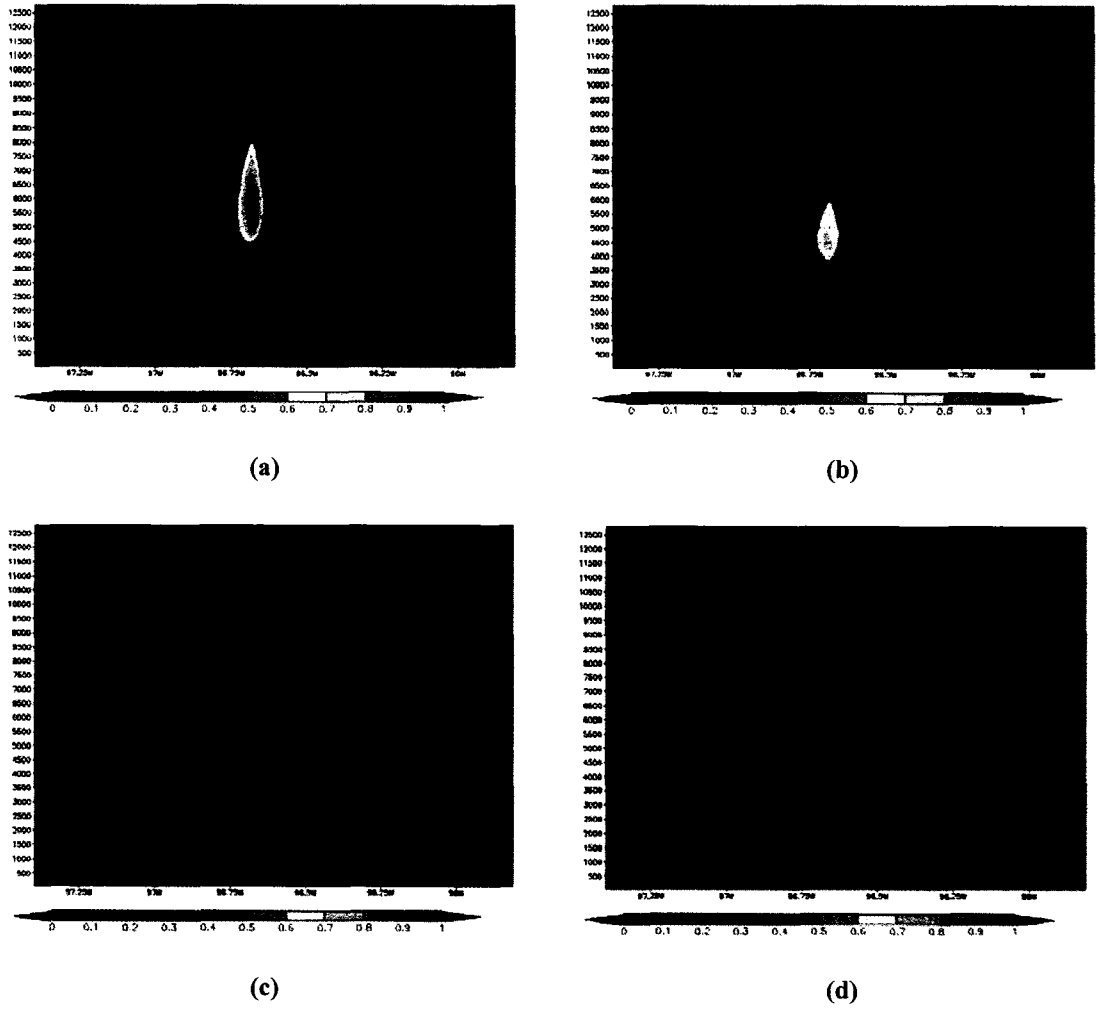

Figure 4.53 Vertical Cross-section of graupel mixing ratio in g·kg^{-1}at 39.05 N at (a) 1930 UTC, (b) 1935 UTC, (c) 1940 UTC, (d) 1945 UTC for the warm bubble experiment over the southwestern portion of the burn scar.

Continuing analysis of the graupel field, Figure 4.53 shows the vertical cross-sections from 1930 UTC to 1945 UTC. While maintaining concentrations seen in the previous figure, the graupel region induced by the bubble has begun to lower, as seen in

Reproduced with permission of the copyright owner. Further reproduction prohibited without permission.

Figure 4.53(a). By 1935 UTC in Figure 4.53(b), the graupel region continues to lower and now decreases in concentration. Since the surface is well above freezing, the graupel melts as it descends through the atmosphere. The lowest altitude at which graupel is predicted is 3000 m. Over the next 10 minutes, concentration of graupel decreases and begins to spread horizontally as seen at 1940 UTC in Figure 4.53(c) and at 1945 UTC in Figure 4.53(d).

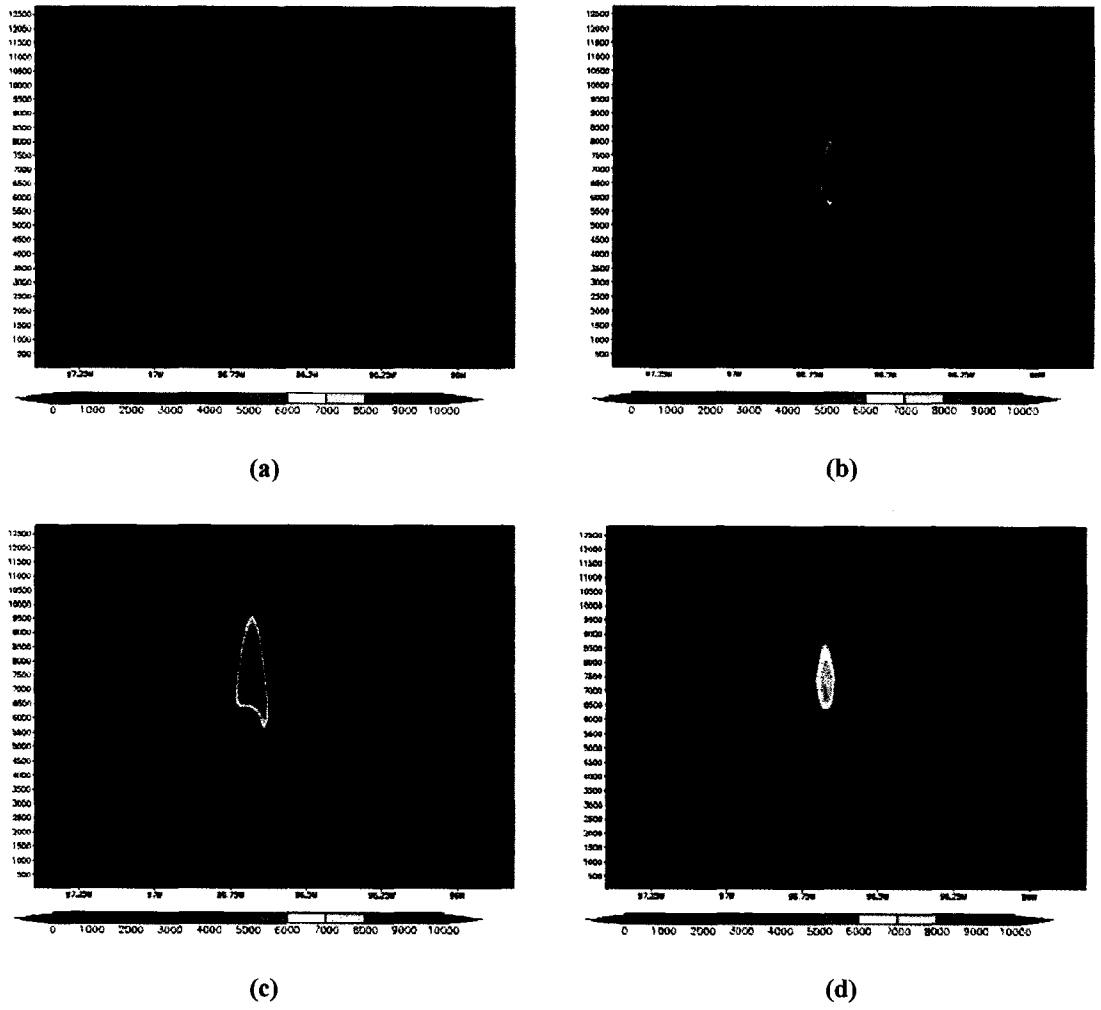

Figure 4.54 Graupel number concentration in m^{-3} for the burn scar simulation with the warm bubble release at (a) 1910 UTC, (b) 1915 UTC, (c) 1920 UTC and (d) 1925 UTC.

Reproduced with permission of the copyright owner. Further reproduction prohibited without permission.

Graupel number concentration in m^{-3} is plotted in Figure 4.54 for the bubble experiment with the burn scar from 1910 UTC to 1925 UTC. The patterns follow those seen in mixing ratio plots in Figure 4.52. This field is used to judge the potential for lightning development in these clouds induced by the release of the warm, moist bubble. Takahashi et al. (1999) found that graupel must be present in clouds in concentrations of at least 1 L^{-1} (or 1000 m^{-3}). By 1915 UTC, a small but concentrated area of graupel is predicted with magnitudes as high as 160,000 m^{-3} or 160 L^{-1} in Figure 4.54(b). Figure 4.54(c) and (d) show a decrease in graupel number concentration with time, but values remain above the 1 L^{-1} threshold and the area of vertical and horizontal coverage continues to increase with time.

Reproduced with permission of the copyright owner. Further reproduction prohibited without permission.

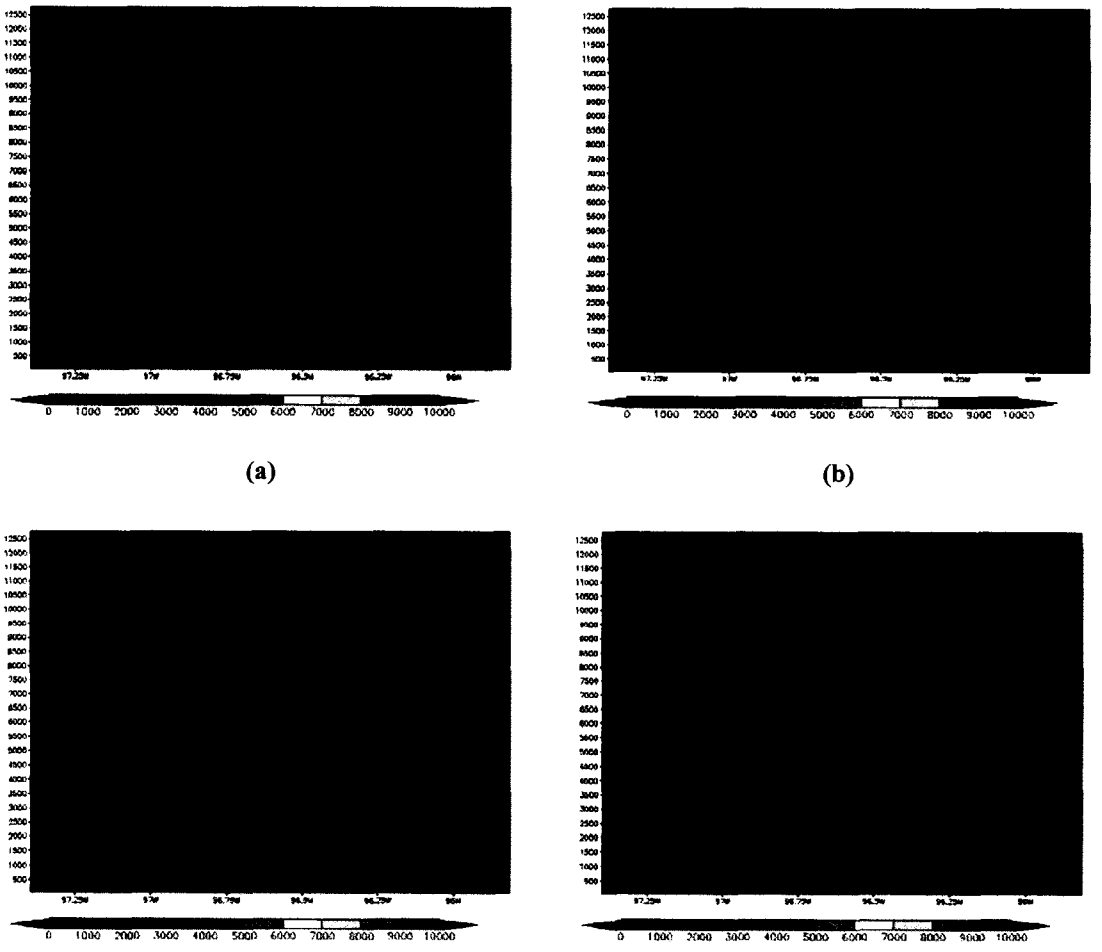

Figure 4.55 Graupel number concentration in m^{-3} for the burn scar simulation with the warm bubble release at (a) 1930 UTC, (b) 1935 UTC, (c) 1940 UTC and (d) 1945 UTC.

Figure 4.55 shows how the number concentration of graupel continues to evolve within the cloud induced by the warm, moist bubble. The region of graupel expands and lowers to near 3000 m by 1935 UTC as seen in Figure 4.55(b), with the number concentrations continuing to decrease, but with values as high as 3500 m^{-3}. By 1940 UTC, the column of graupel is beginning to shrink as seen in Figure 4.55(c). A few minutes later, at 1945 UTC, the highest number concentration of graupel was predicted to be lower than 1 L^{-1} as the graupel column continued to shrink.

Reproduced with permission of the copyright owner. Further reproduction prohibited without permission.

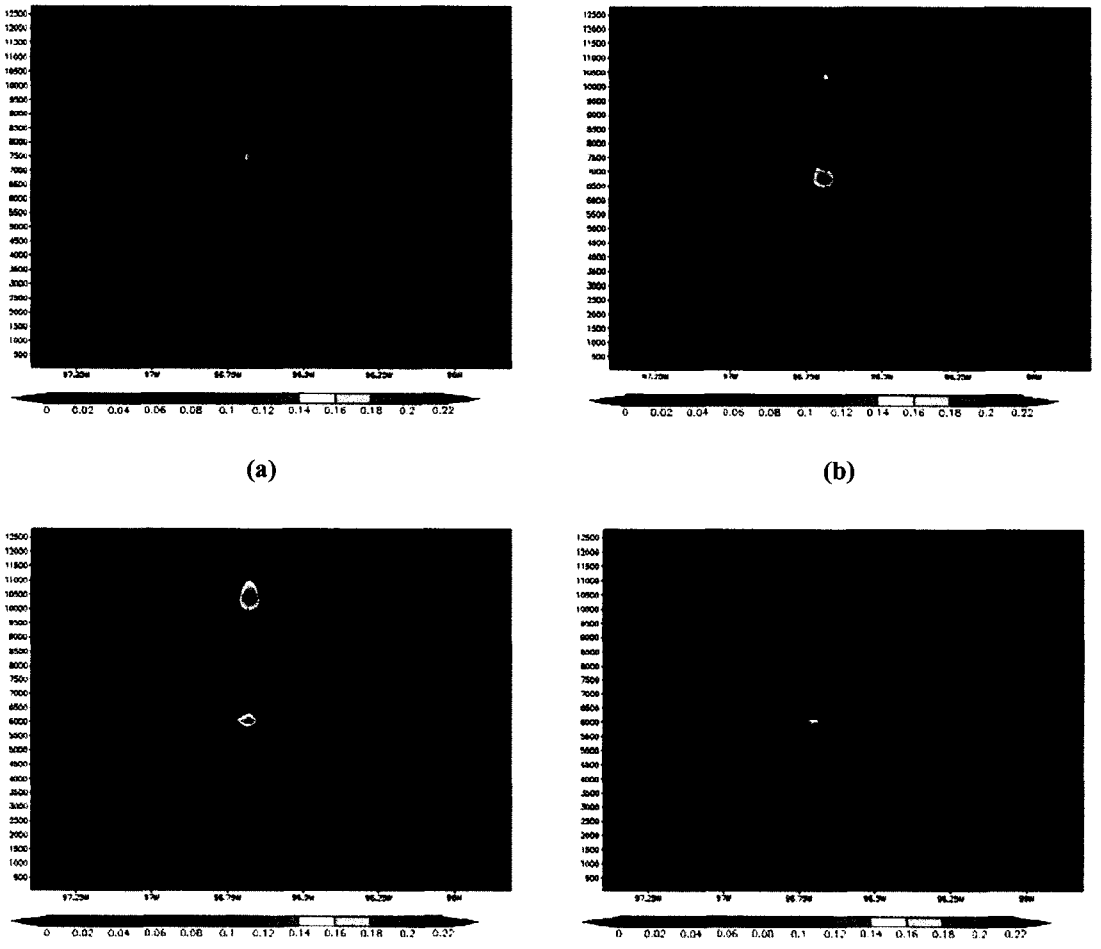

Figure 4.56 Vertical Cross-section of pristine ice at 39.05 N at (a) 1915 UTC, (b) 1920 UTC, (c) 1925 UTC, (d) 1930 UTC for the warm bubble experiment over the southwestern portion of the burn scar.

The pristine ice concentrations seen in Figure 4.56 show values on the order of 0.1-0.2 $g \cdot kg^{-1}$ occurring above 5000 m with an initial elongated distribution in the area of the bubble. The cloud ice settles into two circular regions stacked above where the bubble was released.

4.3.2 Warm Bubble Experiment without Burn Scar

Reproduced with permission of the copyright owner. Further reproduction prohibited without permission.

To see the impact of the presence of the burn scar on the development of convection and the related cloud, a bubble simulation was run over a uniform environment undisturbed by fire. The entire domain had uniform characteristics of the environment surrounding the burn scar in the previous simulation. The same warm, moist bubble was released at the same time, 1900 UTC or seven hours after the simulation was initialized, in the same location in the domain. The following figures and discussion directly compare the results of the simulations in which a bubble was released over the burn scar and over the uniform environment. Both the dynamics of the flow and microphysics of the clouds induced by the bubble are examined.

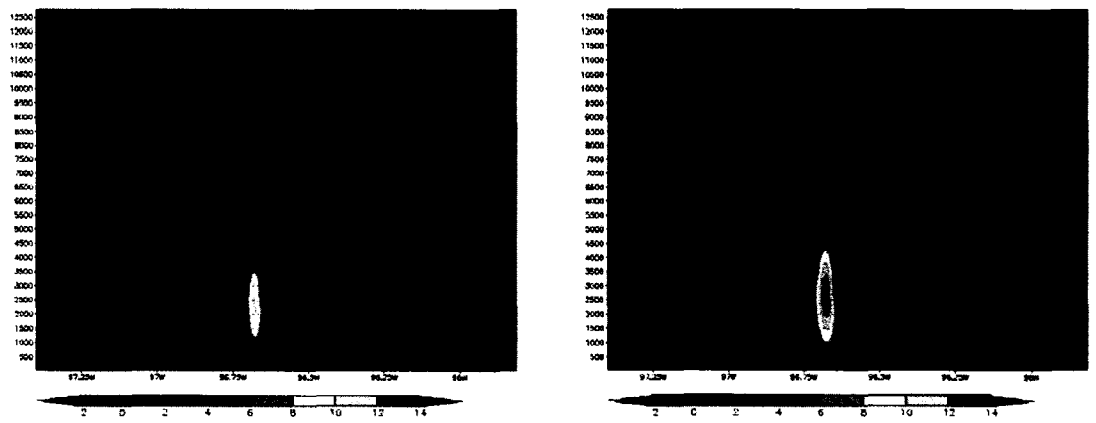

(a) (b)

Figure 4.57 Vertical Cross-section of vertical velocity at 39.05 N at 1910 UTC for the southwestern bubble experiments for (a) no burn environment (b) with the burn scar.

Figure 4.57 shows the vertical cross-section of vertical velocity at 1910 UTC, taken through the bubble at 39.05 N, ten minutes after the bubble was released. The upward motion induced by the warm, moist bubble is much stronger over the burn scar than over the undisturbed environment with the region of 12 $m \cdot s^{-1}$ and greater between 2000 m and 3500 m. In contrast, for the undisturbed environment, the maximum region

Reproduced with permission of the copyright owner. Further reproduction prohibited without permission.

of 9 $m \cdot s^{-1}$ and greater was between 1500 m and 3000 m. The updraft induced by the bubble extended slightly higher and was significantly stronger over the burn scar than over the undisturbed region.

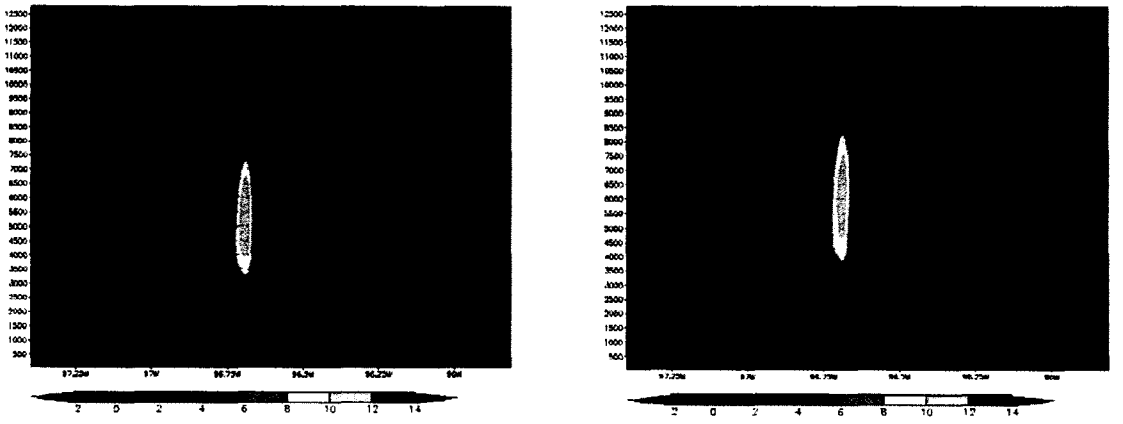

(a) (b)

Figure 4.58 Vertical Cross-section of vertical velocity at 39.05 N at 1920 UTC for the southwestern bubble experiments for (a) no burn environment (b) with the burn scar.

Moving forward to 1920 UTC, 20 minutes after the bubble was released and depicted in Figure 4.58, the updraft induced by the bubble is displaced higher in atmosphere over the burn scar with the maximum region of 10 $m \cdot s^{-1}$ and greater between 4700 m and 7500 m. Over the undisturbed environment, the updraft is similar in strength, but the region of 10 $m \cdot s^{-1}$ and greater occurred at a lower level in the atmosphere extending from 4000 m to 6800 m.

Reproduced with permission of the copyright owner. Further reproduction prohibited without permission.

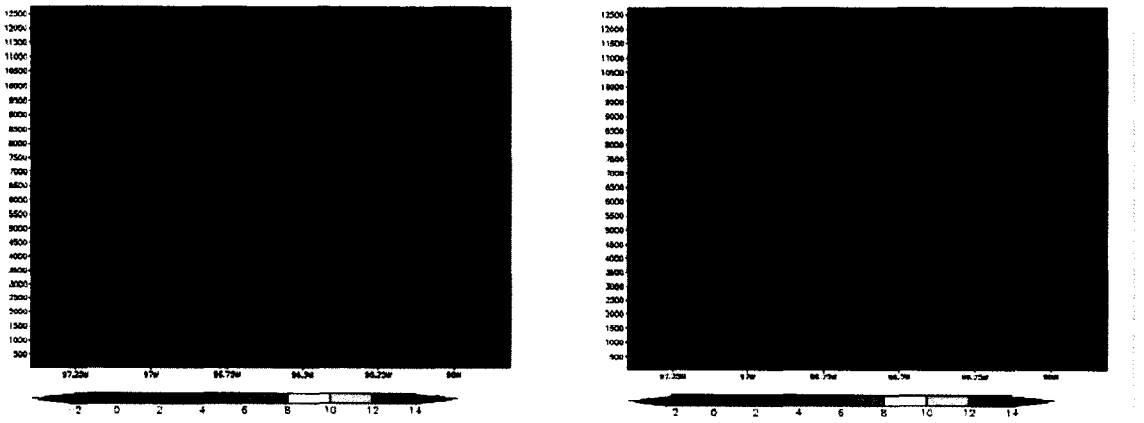

(a) (b)

Figure 4.59 Vertical Cross-section of vertical velocity at 39.05 N at 1930 UTC for the southwestern bubble experiments for (a) no burn environment (b) with the burn scar.

By 1930 UTC, the upward motion induced by the bubble has moved further up in the atmosphere, and downward motion has formed in the lower levels beneath the updraft as seen in Figure 4.59. Comparing the two experiments the updraft over the burn scar continues to be stronger, although only slightly stronger and higher in the atmosphere. The downdraft beneath the updraft is weaker than in the uniform environment, but covers a larger region over the cross-section.

Reproduced with permission of the copyright owner. Further reproduction prohibited without permission.

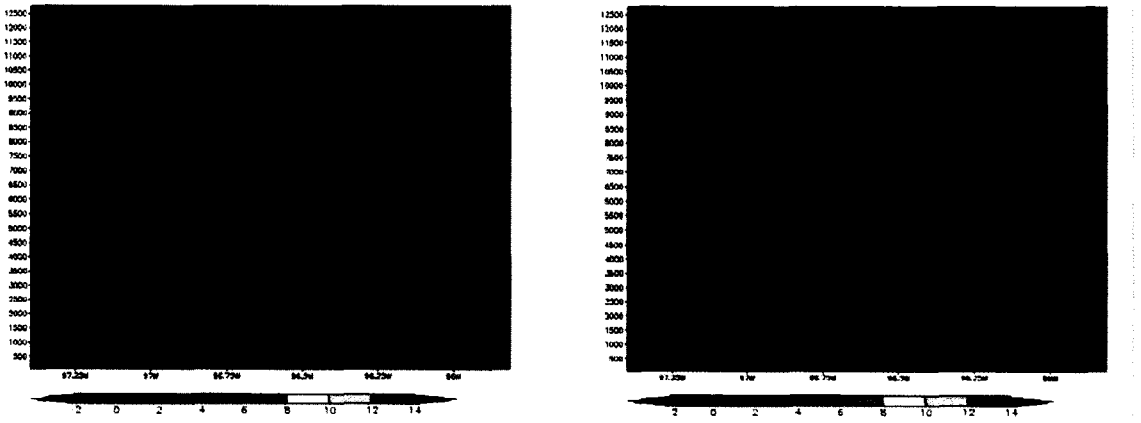

(a) (b)

Figure 4.60 Vertical Cross-section of vertical velocity at 39.05 N at 1940 UTC for the southwestern bubble experiments for (a) no burn environment (b) with the burn scar.

Figure 4.60 shows some remnants of the bubble as upward motion above 6000 m in both simulations at 1940 UTC. The motion region is slightly stronger for the burn scar simulation than the undisturbed surface. The downward motion is similar in magnitude for both simulations although the region of downward motion is more widespread for the burn scar simulation.

Reproduced with permission of the copyright owner. Further reproduction prohibited without permission.

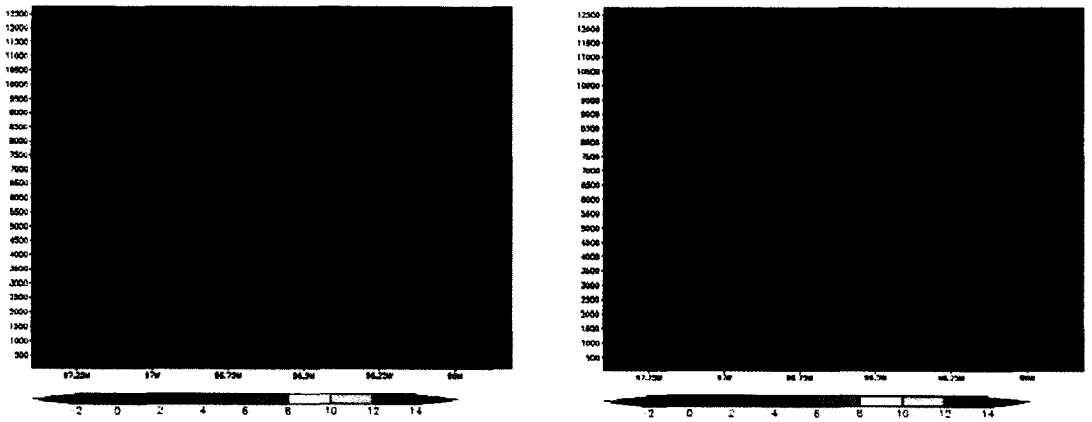

(a) (b)

Figure 4.61 Vertical Cross-section of vertical velocity at 39.05 N at 1950 UTC for the southwestern bubble experiments for (a) no burn environment (b) with the burn scar.

By 1950 UTC, the vertical velocity continued to decrease with a small concentrated area of upward motion near 5000 m. Magnitudes of vertical velocity are similar in both simulations with the burn scar experiment showing some regions of stronger motion.

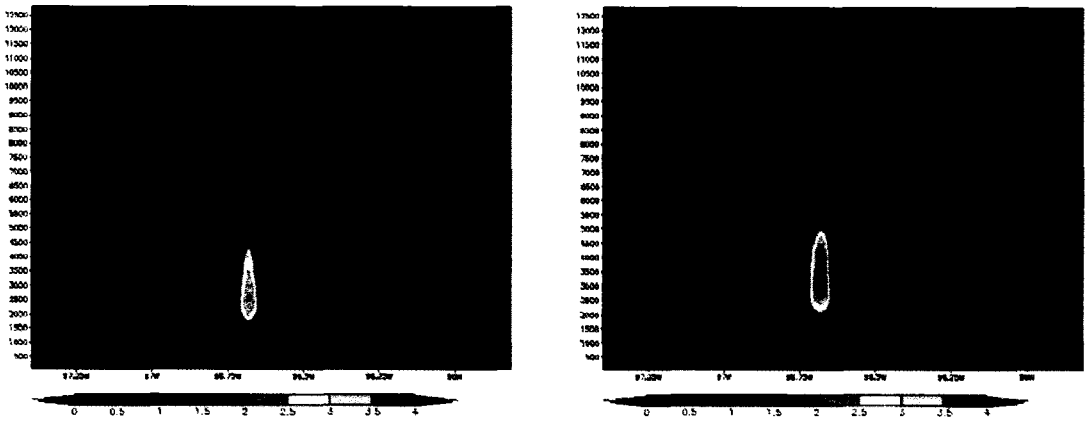

(a) (b)

Figure 4.62 Vertical Cross-section of cloud water at 39.05 N at 1910 UTC for the southwestern bubble experiments for (a) no burn environment (b) with the burn scar.

Reproduced with permission of the copyright owner. Further reproduction prohibited without permission.

The cloud water field shows the effect of the vertical velocity field on cloud development. Starting at 1910 UTC in Figure 4.62, ten minutes after the bubble was released, the region of cloud water over the burn scar includes an area of 4 $g \cdot kg^{-1}$ and greater from 3000 m to 4000 m as seen in (b). A much smaller area of 3.5 $g \cdot kg^{-1}$ and greater extends from 2500 m to 2700 m as shown in (a).

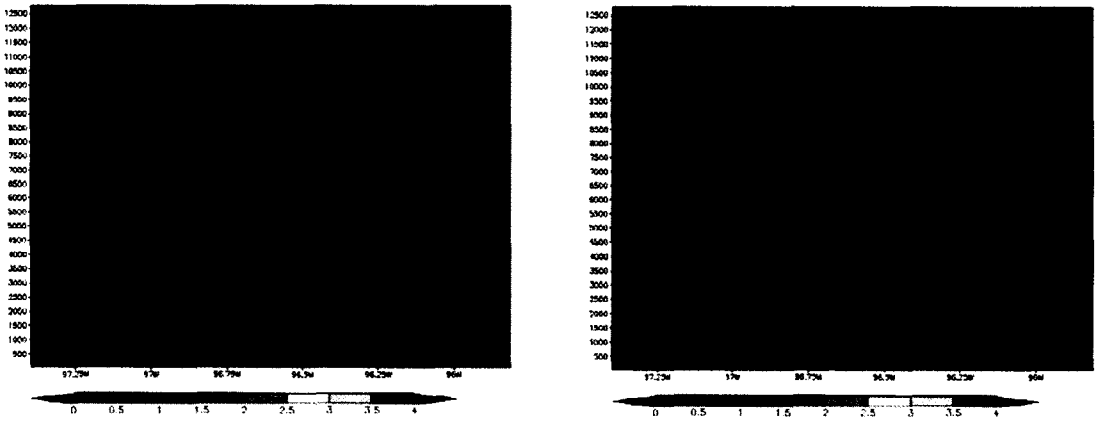

(a) (b)

Figure 4.63 Vertical Cross-section of cloud water at 39.05 N at 1920 UTC for the southwestern bubble experiments for (a) no burn environment (b) with the burn scar.

Figure 4.63 shows similar magnitudes of cloud water in both simulations at 1920 UTC. In the case of the burn scar simulation (b), cloud begins to form and spread out between 2000 m and 2500 m in addition to the cloud formed by the updraft induced by the bubble.

Reproduced with permission of the copyright owner. Further reproduction prohibited without permission.

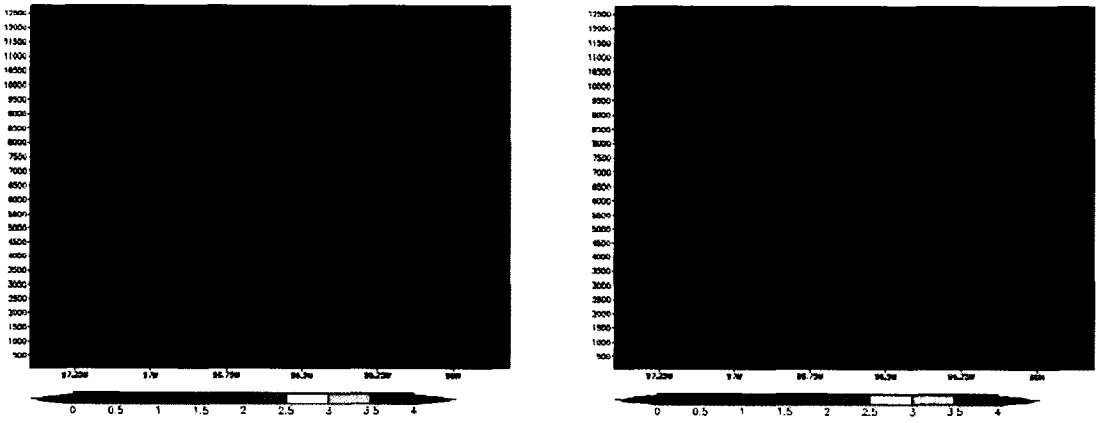

(a) (b)

Figure 4.64 Vertical Cross-section of cloud water at 39.05 N at 1930 UTC for the southwestern bubble experiments for (a) no burn environment (b) with the burn scar.

At 1930 UTC, the cloud water cross-section is depicted in Figure 4.64. The cloud induced by the main updraft shows greatly decreased concentrations of cloud water. The cloud layer between 2000 m and 2500 m shows similar concentrations, but the burn scar simulations shows greater coverage over the domain (b) than the undisturbed environment.

Reproduced with permission of the copyright owner. Further reproduction prohibited without permission.

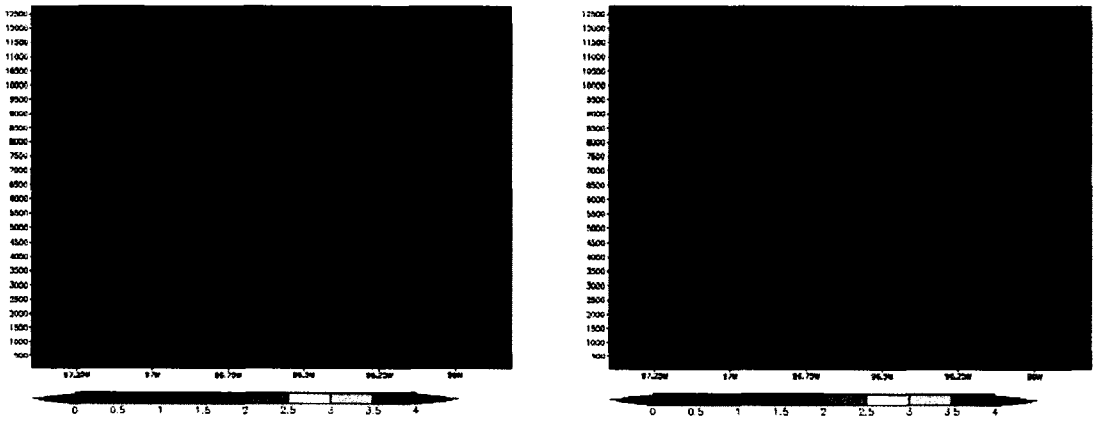

(a) (b)

Figure 4.65 Vertical Cross-section of cloud water at 39.05 N at 1940 UTC for the southwestern bubble experiments for (a) no burn environment (b) with the burn scar.

Figure 4.65 shows how the cloud water field has evolved by 1940 UTC. The cloud over the burn scar region (b) continues to expand horizontally compared to that for the undisturbed environment (a). The highest values of cloud water are seen between 2000 m and 2500 m and are similar in concentration (1 $g \cdot kg^{-1}$) with a more widespread area of cloud in this layer in the burn scar domain. In both simulations, a cloud-free area is seen in the region where the bubble was released associated with the downdraft that formed near 3000 m as seen in Figure 4.60.

Reproduced with permission of the copyright owner. Further reproduction prohibited without permission.

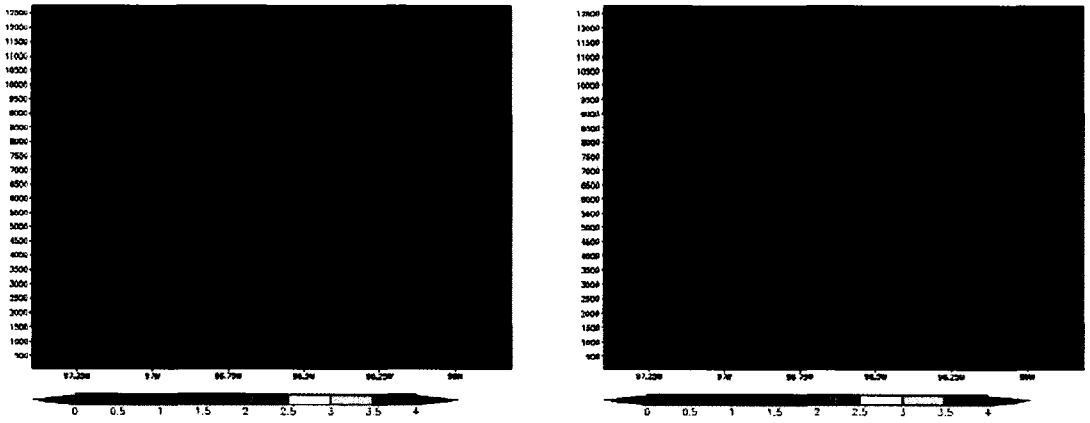

(a) (b)

Figure 4.66 Vertical Cross-section of cloud water at 39.05 N at 1950 UTC for the southwestern bubble experiments for (a) no burn environment (b) with the burn scar.

A final look of cloud water is done at 1950 UTC, shown in Figure 4.66. In both simulations, the cloud between 4000 m and 4500 m continued to decrease in concentration. Between 2000 m and 2500 m, the cloud layer continued to spread horizontally with the burn scar simulation showing a more widespread area while the undisturbed environment shows slightly higher concentrations. A third layer of cloud between 1000 m and 1500 m has expanded and increased in concentration with higher concentrations seen in the burn scar simulation.

Reproduced with permission of the copyright owner. Further reproduction prohibited without permission.

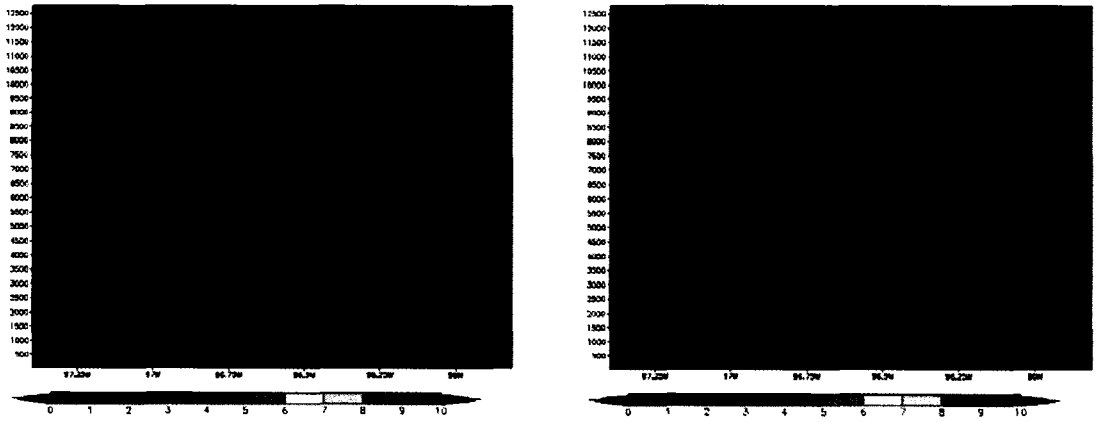

(a) (b)

Figure 4.67 Vertical Cross-section of rain water at 39.05 N at 1910 UTC for the southwestern bubble experiments for (a) no burn environment (b) with the burn scar.

Examining the rain water generated by the bubble in each simulation begins with Figure 4.67, which shows the cross-section through the bubble at 1910 UTC over the undisturbed environment (a) and the burn scar (b). Comparing the two results, the rain water concentration is greater and appeared higher in the atmosphere for the burn scar simulation. The maximum region of 0.2 $g \cdot kg^{-1}$ and greater was predicted between 3000 m and 3500 m in the burn scar simulation. Over the undisturbed environment, between 2300 m and 2700 m concentrations of 0.11 $g \cdot kg^{-1}$ and greater have formed.

Reproduced with permission of the copyright owner. Further reproduction prohibited without permission.

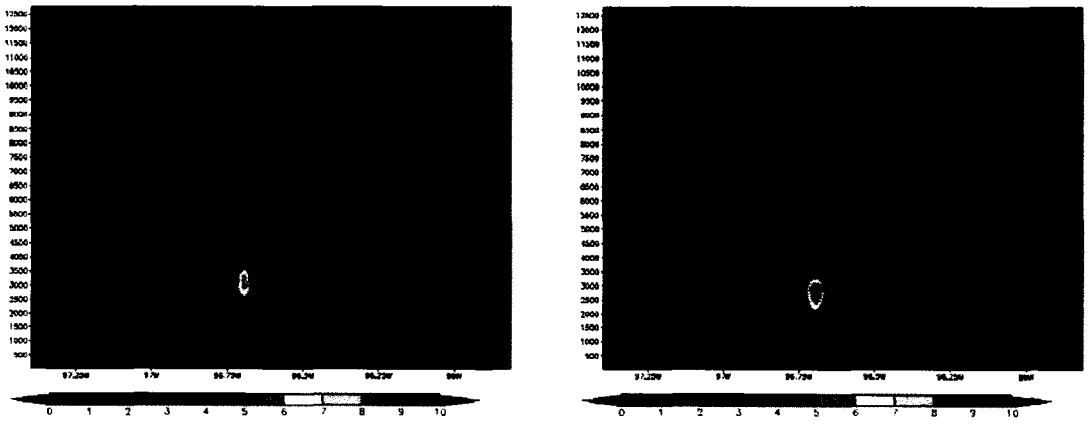

(a) (b)

Figure 4.68 Vertical Cross-section of rain water at 39.05 N at 1920 UTC for the southwestern bubble experiments for (a) no burn environment (b) with the burn scar.

Ten minutes later in the simulations at 1920 UTC, the rain water area has increased by fifty times and dropped to below 4000 m in the burn scar simulation as seen in Figure 4.68 (b). In the undisturbed simulation (a), the rain water area has lowered slightly with significant increases in concentration, but values lower than seen in the burn scar simulation.

Reproduced with permission of the copyright owner. Further reproduction prohibited without permission.

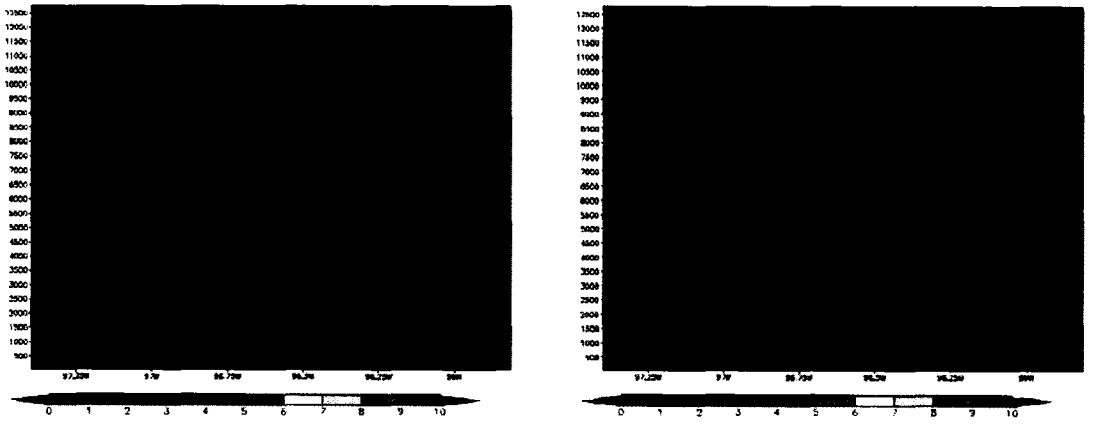

(a) (b)

Figure 4.69 Vertical Cross-section of rain at 39.05 N at 1930 UTC for the southwestern bubble experiments for (a) no burn environment (b) with the burn scar.

By 1930 UTC, as seen in Figure 4.69, both simulations show similar concentrations of rain water as the peak values have reached the surface. At this point it looks as if the cloud is beginning to rain itself out. This coincides with the downdraft that develops and was illustrated in Figure 4.59.

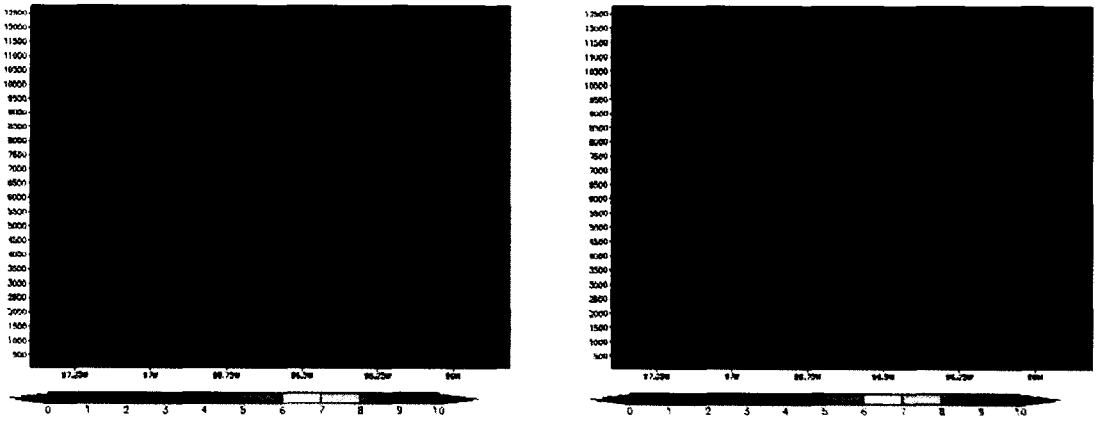

(a) (b)

Figure 4.70 Vertical Cross-section of rain at 39.05 N at 1940 UTC for the southwestern bubble experiments for (a) no burn environment (b) with the burn scar.

Reproduced with permission of the copyright owner. Further reproduction prohibited without permission.

Figure 4.70 shows the cross-sections of rain water at 1940 UTC. Both the simulation with the undisturbed environment (a) and with the burn scar (b) show similar patterns of rain water. Over the ten minutes between Figure 4.69 and Figure 4.70, the regions have elongated and expanded. During this time, the downdraft depicted in Figure 4.60 in the area where the bubble was released has lifted. The highest concentration of rain water in both simulations has decreased from 2.4 $g \cdot kg^{-1}$ in Figure 4.69 to 0.35 $g \cdot kg^{-1}$ in Figure 4.70.

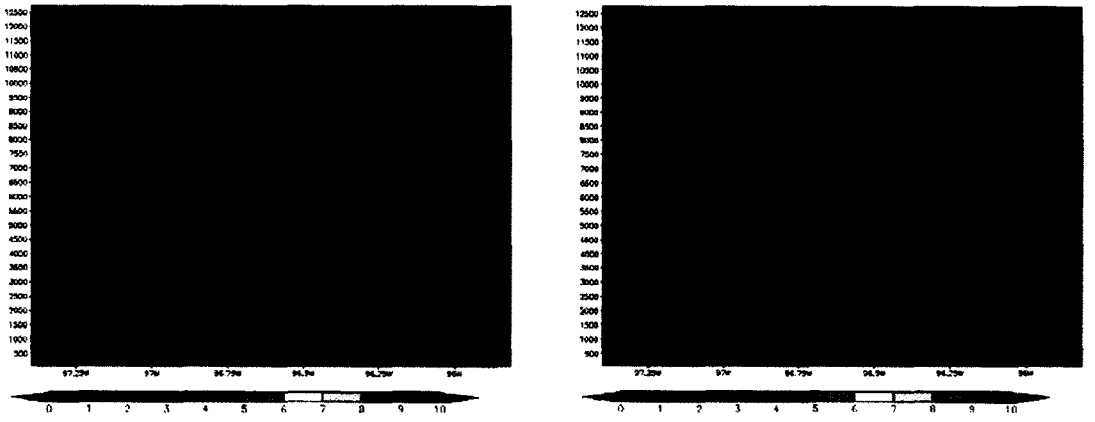

(a) (b)

Figure 4.71 Vertical Cross-section of rain at 39.05 N at 1950 UTC for the southwestern bubble experiments for (a) no burn environment (b) with the burn scar.

At 1950 UTC the rain water field is depicted in Figure 4.71. Concentrations have continued to decrease with the highest concentrations near the surface as rain settles to the ground and a secondary region of high concentrations near 3000 m.

Reproduced with permission of the copyright owner. Further reproduction prohibited without permission.

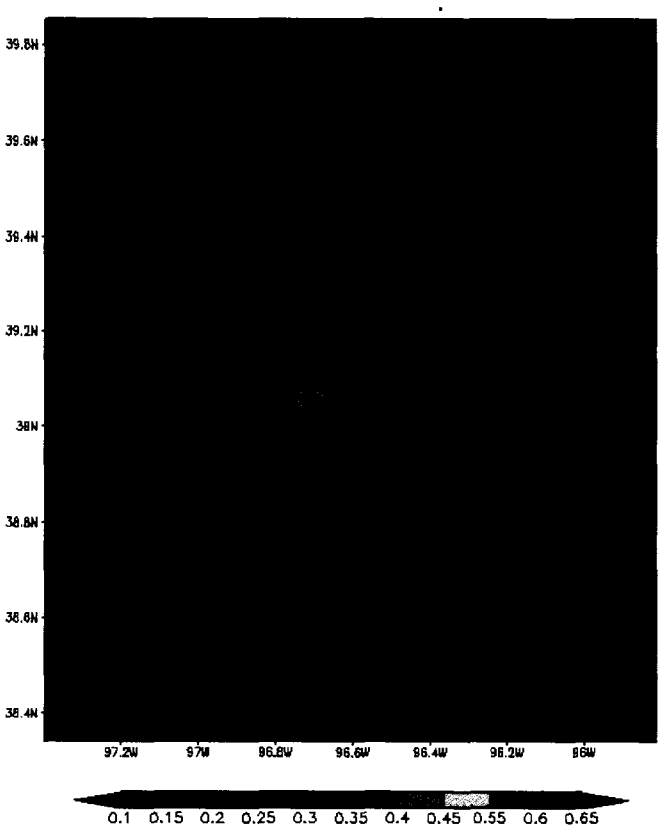

Figure 4.72 Total precipitation predicted at the surface in inches at 2000 UTC for the southwest bubble experiment without a burn scar.

By 2000 UTC, no additional precipitation was predicted in the simulation of the southwest bubble over the uniform environment. Precipitation was predicted over a smaller region with lower values that in the simulation with the burn scar. In this simulation, maximum rainfall amounts were predicted to be 0.65 inches. This means the burn scar simulation showed a 17% increase in precipitation due to the presence of the scar.

Reproduced with permission of the copyright owner. Further reproduction prohibited without permission.

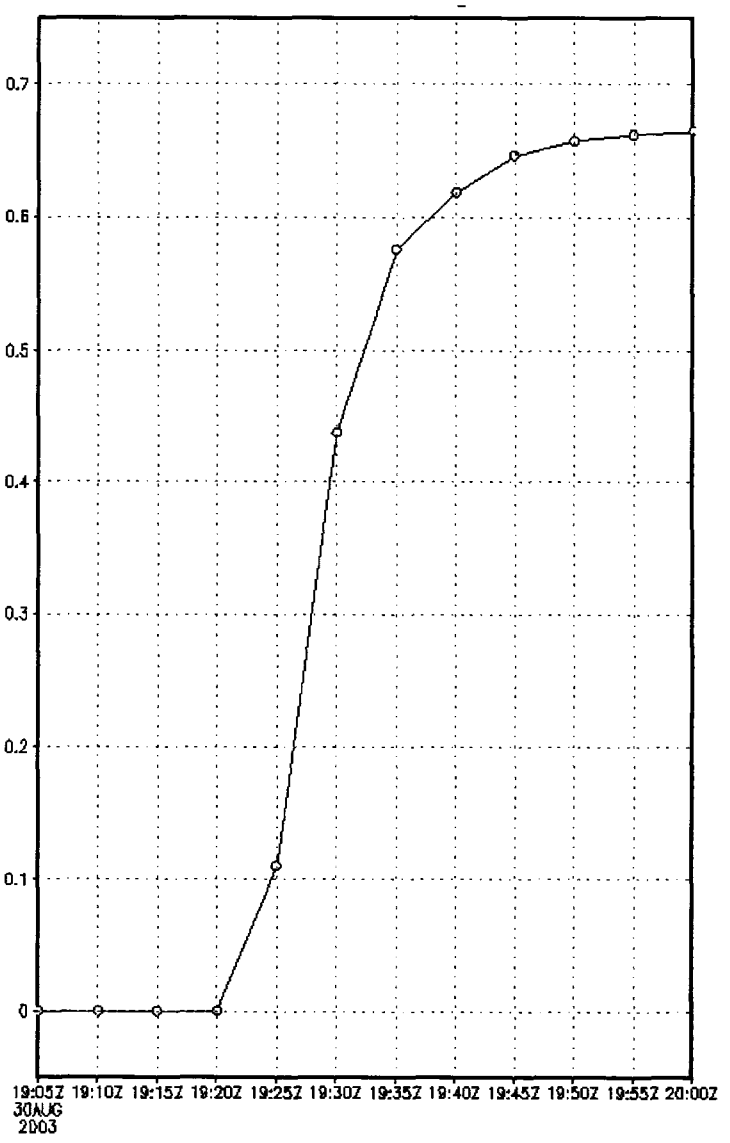

Figure 4.73 Total precipitation as a function of time for the bubble experiment over the undisturbed environment from 1810 UTC to 2000 UTC 30 August 2003.

Also, timing of the precipitation is similar, as can be seen by comparing Figure 4.73 for the undisturbed environment with Figure 4.51 for the burn scar. The slope of the line follows the same pattern over time with differing magnitudes. Since the amount of precipitation was greater with the burn scar experiment, the intensity of the shower over

Reproduced with permission of the copyright owner. Further reproduction prohibited without permission.

the burn scar was greater. This has implications for flooding potential over the scar which will be discussed in chapter 6.

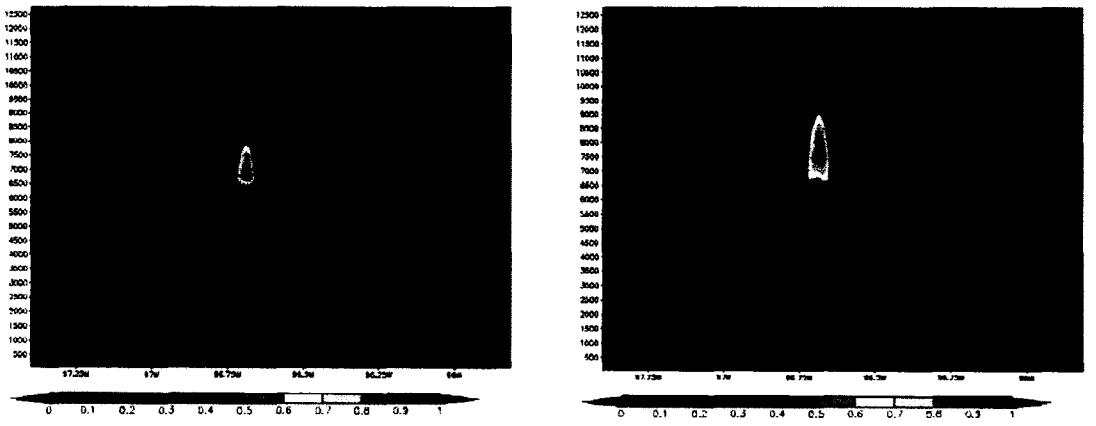

(a) (b)

Figure 4.74 Vertical Cross-section of graupel mixing ratio in g·kg^{-1} at 39.05 N at 1920 UTC for the southwestern bubble experiments for (a) no burn environment (b) with the burn scar.

Comparing the simulations with and without the burn scar, the graupel concentrations indicate a difference in the microphysics of the clouds generated by the bubble. Figure 4.74 shows the cross-section of the mixing ratio of graupel at 1920 UTC. Although the concentrations of graupel in both simulations are similar, the size of the graupel field is much larger in the burn scar simulation as seen in region (b).

Reproduced with permission of the copyright owner. Further reproduction prohibited without permission.

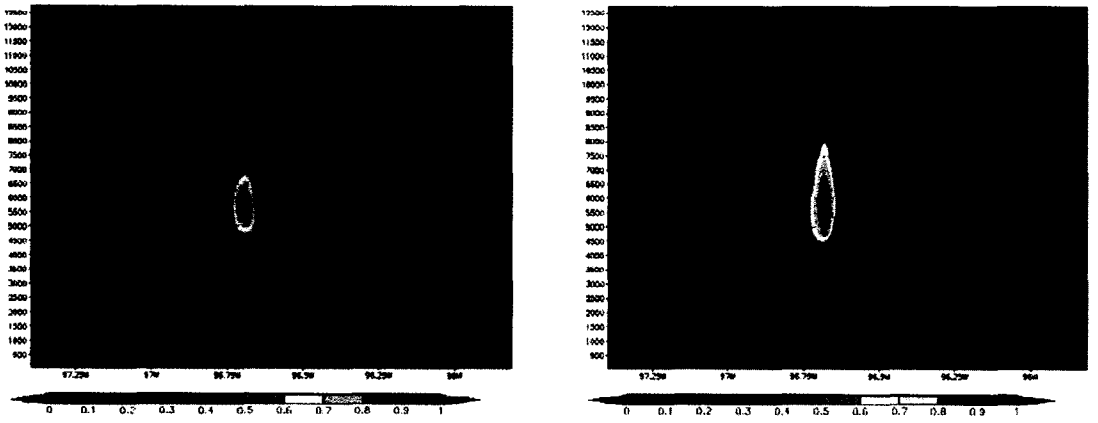

(a) (b)

Figure 4.75 Vertical Cross-section of graupel mixing ratio in g·kg^{-1}at 39.05 N at 1930 UTC for the southwestern bubble experiments for (a) no burn environment (b) with the burn scar.

By 1930 UTC, as seen in Figure 4.75, the simulation with the burn scar shows a much broader region of graupel than in the no burn run. The maximum concentrations of graupel are slightly larger in the no burn simulation (a).

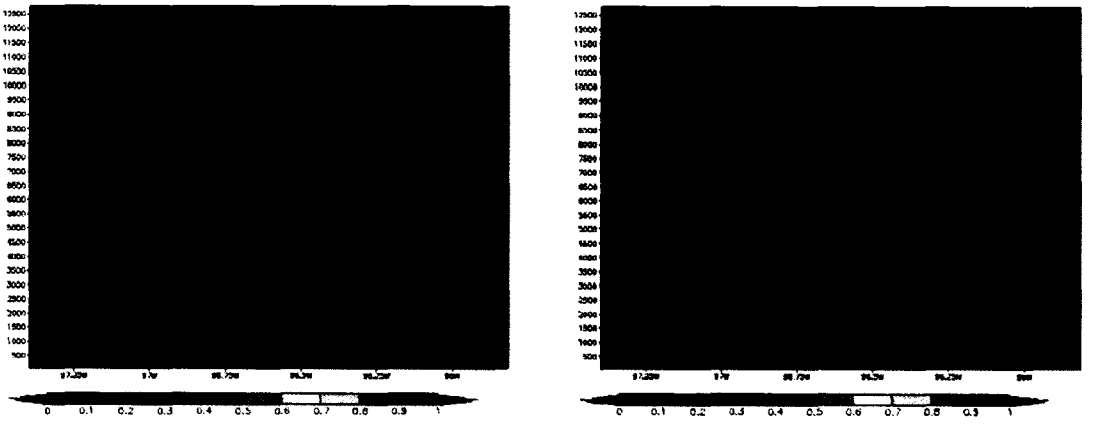

(a) (b)

Figure 4.76 Vertical Cross-section of graupel mixing ratio in g·kg^{-1}at 39.05 N at 1940 UTC for the southwestern bubble experiments for (a) no burn environment (b) with the burn scar.

Reproduced with permission of the copyright owner. Further reproduction prohibited without permission.

To further analyze the evolution of the graupel field in the two simulations, data at 1940 UTC is presented in Figure 4.76. The concentrations in both simulations decreased significantly, with the burn scar simulation having slightly higher concentrations (b) than the no burn simulation (a). The burn scar simulation again has a much broader coverage of graupel than the no burn simulation.

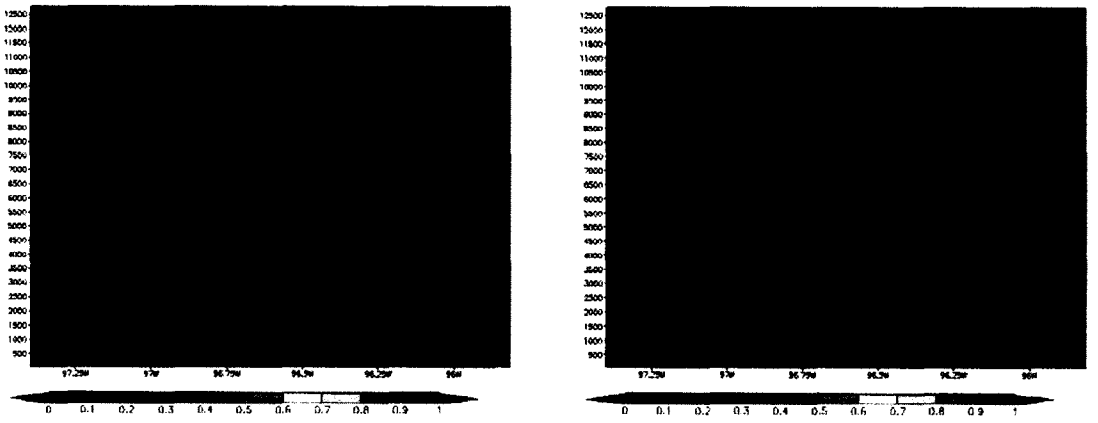

(a) (b)

Figure 4.77 Vertical Cross-section of graupel mixing ratio in g·kg^{-1}at 39.05 N at 1950 UTC for the southwestern bubble experiments for (a) no burn environment (b) with the burn scar.

By 1950 UTC, Figure 4.77 shows concentrations of graupel have decreased to a tenth of those seen with the highest concentrations. The coverage of graupel is much larger in the burn scar simulation compared to the no burn simulation.

Reproduced with permission of the copyright owner. Further reproduction prohibited without permission.

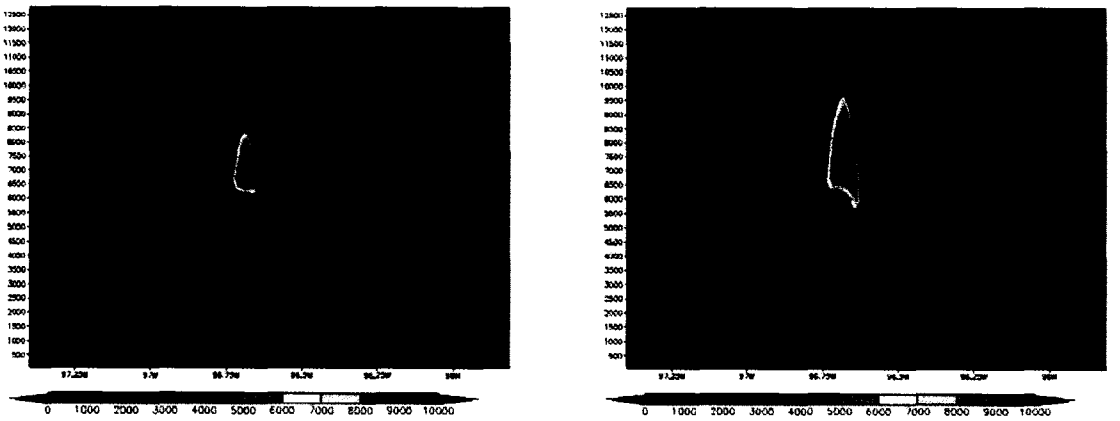

(a) (b)

Figure 4.78 Vertical Cross-section of graupel number concentration (m^{-3}) at 39.05 N at 1920 UTC for the southwestern bubble experiments for (a) no burn environment (b) with the burn scar.

Comparing the number concentration of graupel predicted within the bubble generated convection over both the burn scar and the uniform surface shows that similar concentrations were predicted at 1920 UTC in Figure 4.78, but the burn scar simulation (Figure 4.78(b)) showed a much larger area of graupel than the uniform environment (Figure 4.78(a)).

Reproduced with permission of the copyright owner. Further reproduction prohibited without permission.

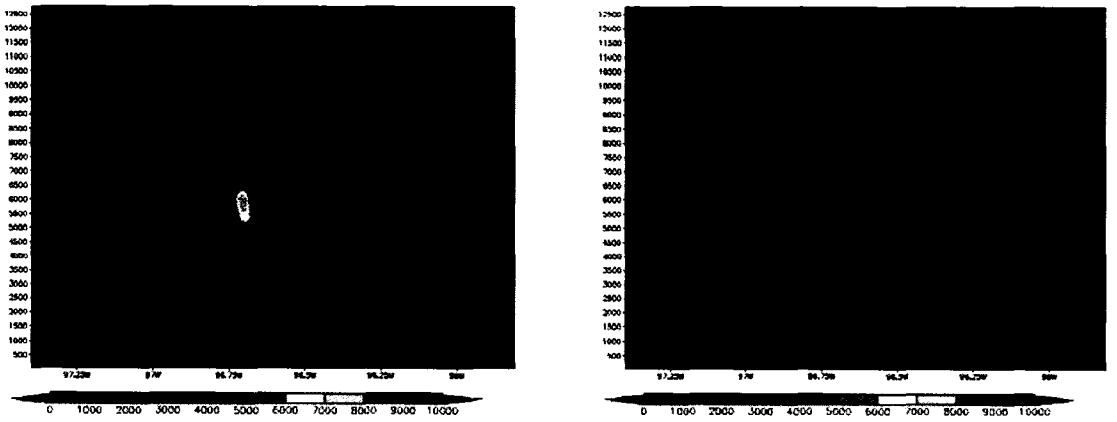

(a) (b)

Figure 4.79 Vertical Cross-section of graupel number concentration (m^{-3}) at 39.05 N at 1930 UTC for the southwestern bubble experiments for (a) no burn environment (b) with the burn scar.

Figure 4.79(a) shows the graupel number concentration at 1930 UTC for the no burn experiment. The maximum concentration shown is higher in this experiment (7000 m^{-3}) than in the burn scar experiment (5000 m^{-3}) as seen in Figure 4.79(b). However, the region of graupel number concentration higher than the amount required for cloud electrification by Takahashi et al. (1999) of 1 L^{-1} or 1000 m^{-3} is larger in the burn scar simulation than the no burn simulation.

Reproduced with permission of the copyright owner. Further reproduction prohibited without permission.

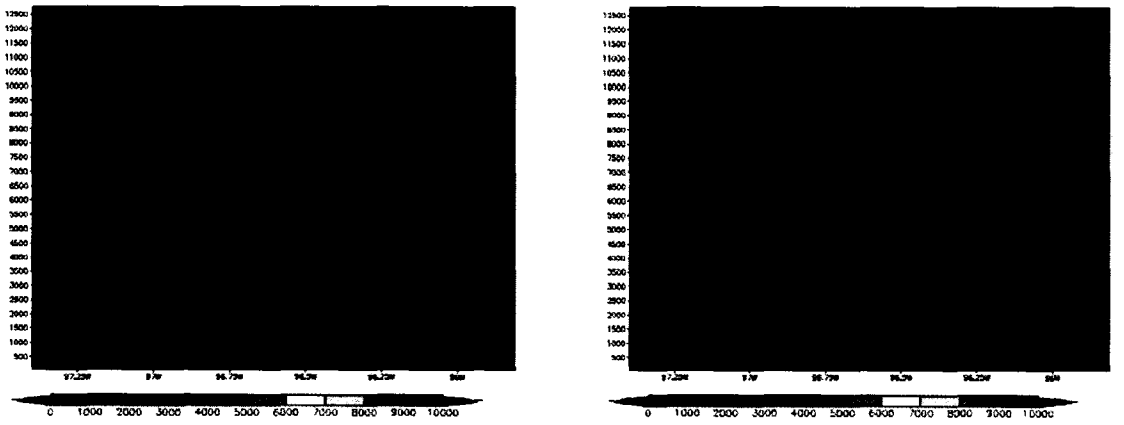

(a) (b)

Figure 4.80 Vertical Cross-section of graupel number concentration (m^{-3}) at 39.05 N at 1940 UTC for the southwestern bubble experiments for (a) no burn environment (b) with the burn scar.

By 1940 UTC, the number concentration of graupel over the entire domain for the no burn simulation is below the 1000 m^{-3} identified for cloud electrification as seen in Figure 4.80(a). Over the burn scar, the region with number concentration values above 1000 m^{-3} has shrunk to a small area indicated in Figure 4.80(b). Over the time analyzed from 1920 UTC through 1940 UTC, the burn scar simulation showed a larger region of graupel with number concentrations associated with cloud electrification by Takahashi et al. (1999).

Reproduced with permission of the copyright owner. Further reproduction prohibited without permission.

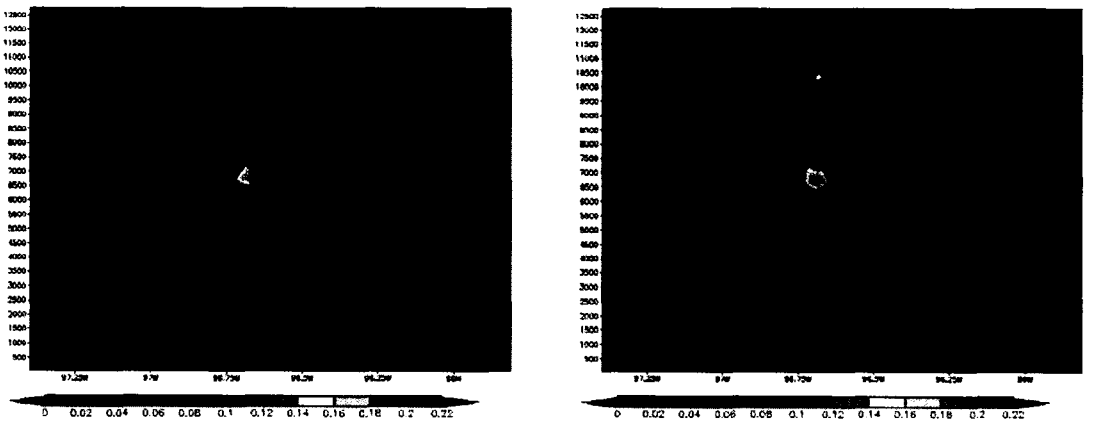

(a) (b)

Figure 4.81 Vertical Cross-section of pristine ice at 39.05 N at 1920 UTC for the southwestern bubble experiments for (a) no burn environment (b) with the burn scar.

Comparing the two simulations in term of the pristine ice field shows differences the in both concentration and distribution. Pristine ice field shows slightly higher concentrations in the simulation over the burn scar as seen in Figure 4.81 (b).

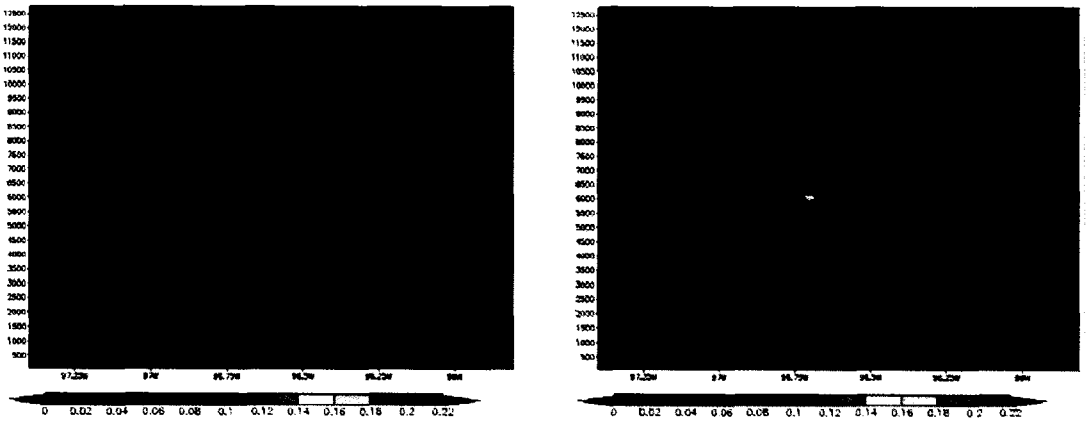

(a) (b)

Figure 4.82 Vertical Cross-section of pristine ice at 39.05 N at 1930 UTC for the southwestern bubble experiments for (a) no burn environment (b) with the burn scar.

Reproduced with permission of the copyright owner. Further reproduction prohibited without permission.

By 1930 UTC values of ice concentration have increased with values still slightly higher over the burn scar and seen in Figure 4.82.

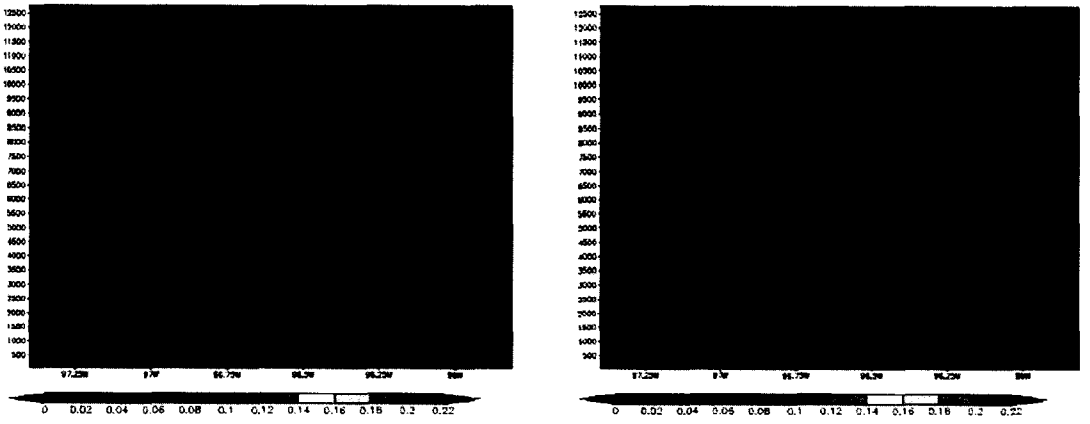

(a) (b)

Figure 4.83 Vertical Cross-section of pristine ice at 39.05 N at 1940 UTC for the southwestern bubble experiments for (a) no burn environment (b) with the burn scar.

In Figure 4.83, ice crystal concentrations have decreased significantly by 1940 UTC. The patterns are very similar in both simulations.

Reproduced with permission of the copyright owner. Further reproduction prohibited without permission.

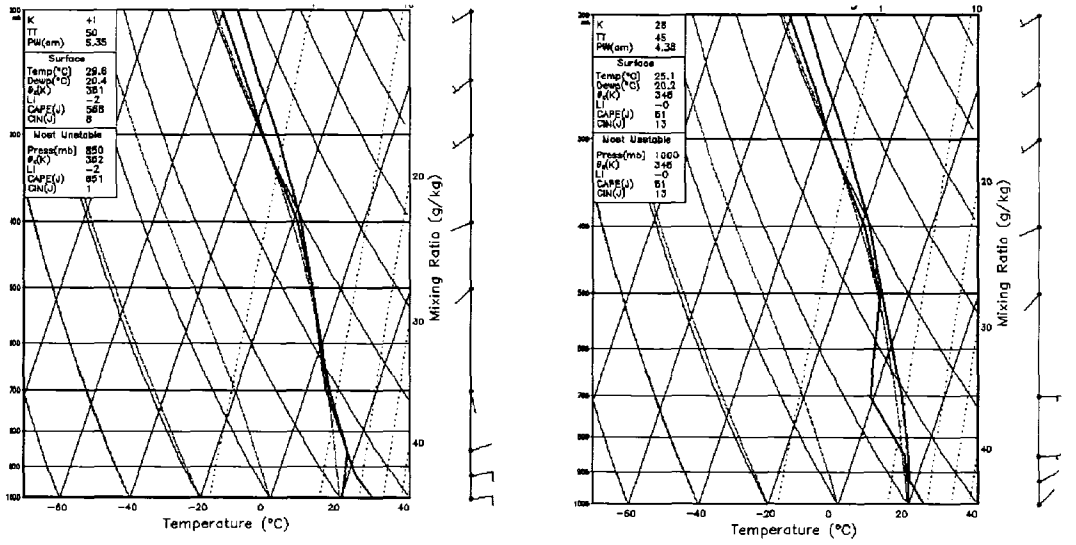

(a) (b)

Figure 4.84 Vertical sounding of the atmosphere taken at 1905 UTC over (a) the burn scar in the bubble and (b) the surrounding environment.

Vertical soundings were examined at two locations in the domain to compare the evolution of the atmosphere during the warm bubble simulation. Figure 4.84 shows the soundings at 1905 UTC, which were five minutes into the bubble simulation. The sounding through the bubble (Figure 4.84 (a)) is distinctively different due to the bubble itself. The temperature within the bubble was increased by 3°C and moisture was increased by 15% throughout the first 15 levels of the atmosphere. A thick layer of saturated air is seen between 870 hPa and 450 hPa, while the surrounding environment (Figure 4.84 (b)) has similar characteristics as those seen in Figure 4.38(b) from the original experiment. Resulting CAPE values show great contrast with a value of 651 $J \cdot kg^{-1}$ in the bubble and 51 $J \cdot kg^{-1}$ in the surrounding environment. The wind field in the lower levels of the atmosphere shows strengthening winds with a more easterly direction.

Reproduced with permission of the copyright owner. Further reproduction prohibited without permission.

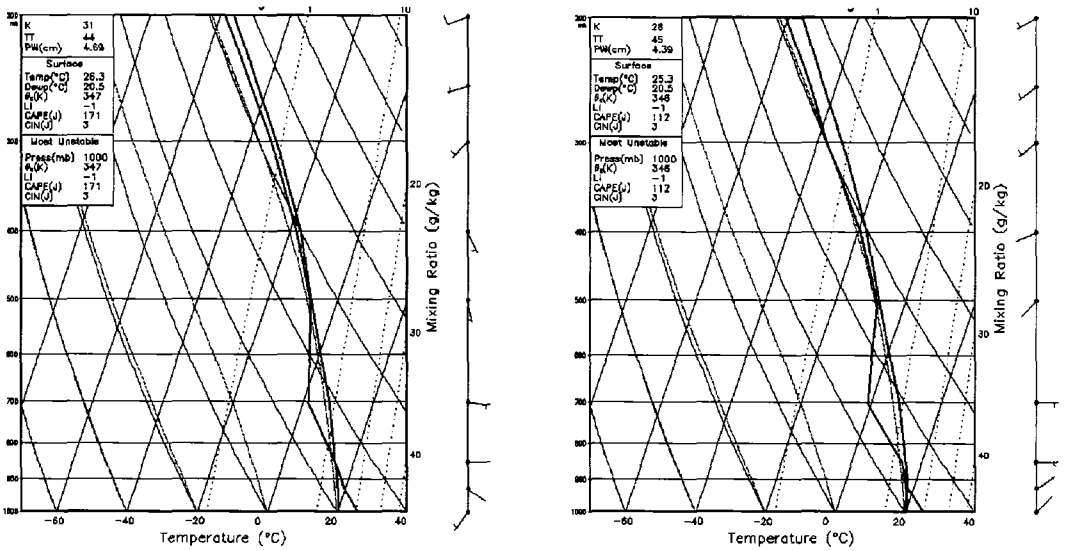

(a) (b)

Figure 4.85 Vertical sounding of the atmosphere taken at 1930 UTC over (a) the burn scar in the bubble and (b) the surrounding environment.

By 1930 UTC, as seen in Figure 4.85, the location through where the bubble was released, begins to return to characteristics of the surrounding environment. The levels between 800 hPa and 500 hPa have begun to dry. CAPE value differences have decreased as the value in the bubble decreased to 171 $J \cdot kg^{-1}$ and in the surrounding area CAPE increased to 112 $J \cdot kg^{-1}$. The wind field shows changes in the low-level winds over the burn scar compared to the surrounding environment.

Reproduced with permission of the copyright owner. Further reproduction prohibited without permission.

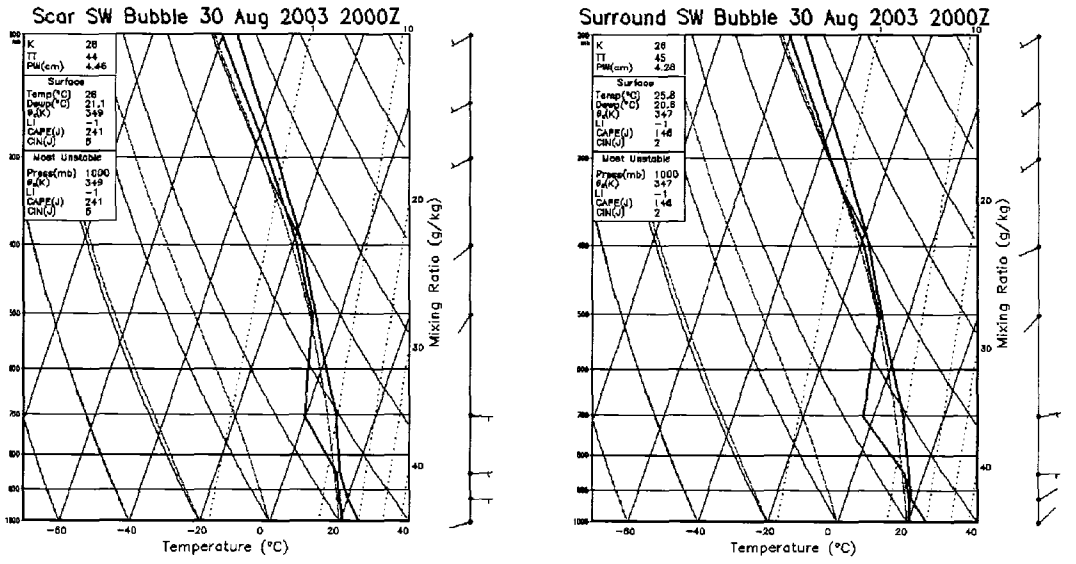

Figure 4.86 Vertical sounding of the atmosphere taken at 2000 UTC over (a) the burn scar in the bubble and (b) the surrounding environment.

At the end of this simulation, at 2000 UTC, the levels between 850 hPa and 500 hPa show more moisture over the burn scar than the surrounding environment. CAPE values have continued to increase over the surrounding environment to 146 $J \cdot kg^{-1}$ while within the bubble, values increased to 241 $J \cdot kg^{-1}$.

Distinct differences were seen in the bubble simulations. This indicates that the presence of the burn scar did affect both the dynamics and the microphysics of the cloud induced by the bubble. These effects will be investigated further in Chapter 6.

Reproduced with permission of the copyright owner. Further reproduction prohibited without permission.

Chapter 5

Sensitivity Tests

5.1 Introduction

The initial simulation of the fire scar surrounded by an unmodified environment leads to questions on the sensitivity of the experiment to different factors. Follow up simulations test the effects of soil moisture change in the region of the burn and the wind profile used to initialize the simulation.

5.2 Soil moisture – Uniform soil moisture experiment

In this experiment, the burn scar was given the same soil moisture as the surrounding environment. This test was meant to isolate the effect of soil moisture modification by the fire on the microclimate of the area. Results were compared with the experiment presented in the last chapter in which the soil moisture of the burn scar was reduced compared to the surrounding environment, shown in Chapter 4.

5.2.1 Surface air temperature

The first parameter examined from this experiment is surface air temperature. The results are compared with section 4.2.1 of the previous chapter.

Reproduced with permission of the copyright owner. Further reproduction prohibited without permission.

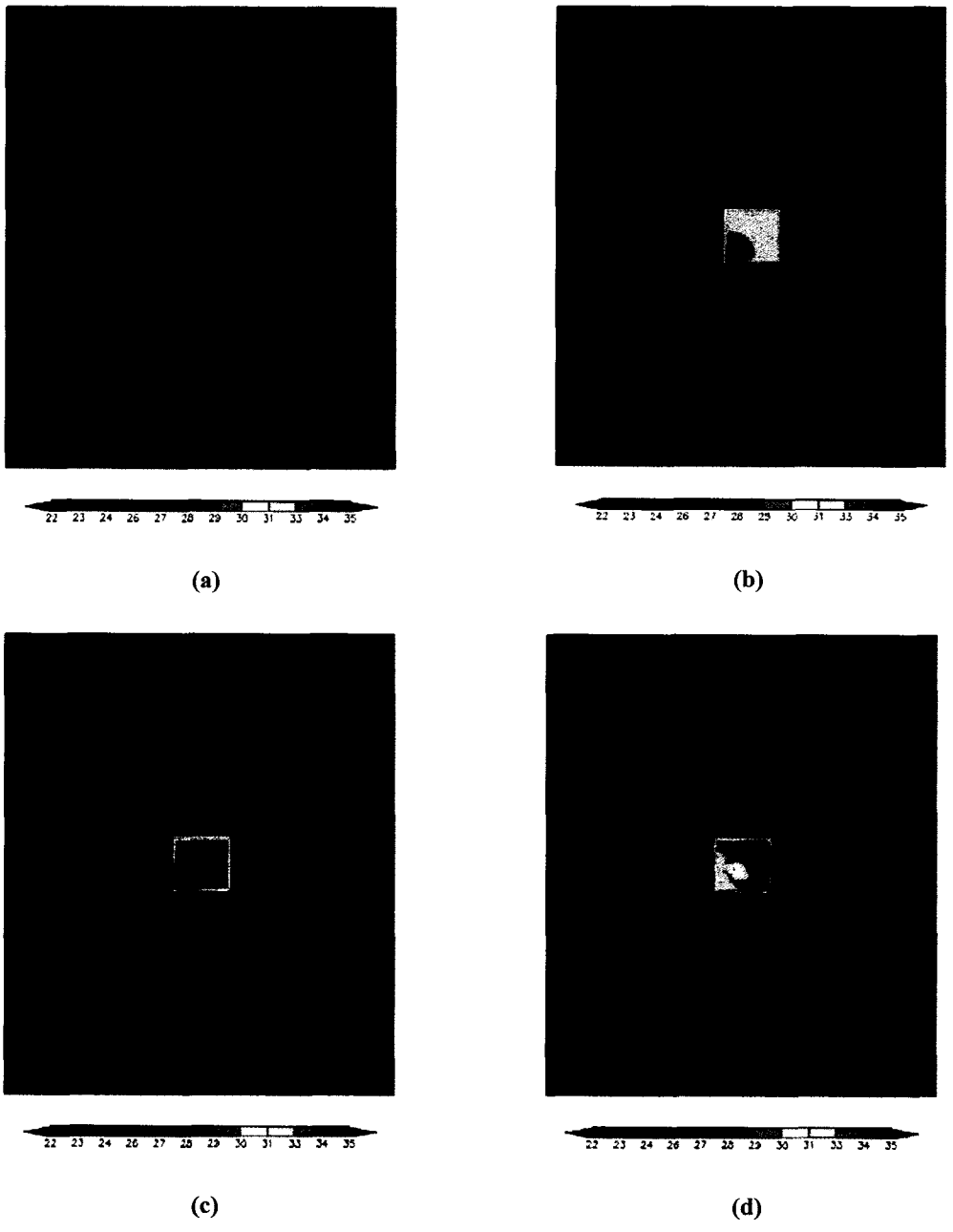

Figure 5.1 Surface temperature in degrees Celsius at (a) 1500 UTC, (b) 1800 UTC, (c) 1900 UTC, and (d) 2000 UTC for the uniform soil moisture experiment.

Figure 5.1 shows the surface temperature fields over a domain with uniform soil moisture. Comparing Figure 5.1(a) with Figure 4.1 shows little difference at 1500 UTC with the highest temperature just 0.3°C cooler over the burn scar in this experiment.

Reproduced with permission of the copyright owner. Further reproduction prohibited without permission.

Comparing Figure 5.1(b) with Figure 4.2 at 1800 UTC and Figure 5.1(c) with Figure 4.3 at 1900 UTC reveals nearly identical results in the surface temperature field between the two experiments. By 2000 UTC, the effects of the lower soil moisture over the burn scar become evident by evaluating the difference between Figure 5.1(d) and Figure 4.4. Higher temperatures were predicted over the drier burn scar in Figure 4.4 with temperatures in the upper 20s, low 30s over the southwestern portion of the burn scar. Figure 5.2 shows the surface temperature at 2100 UTC, which when compared to Figure 4.5, shows temperatures up to 1°C warmer over the burn region
with the lower soil moisture.

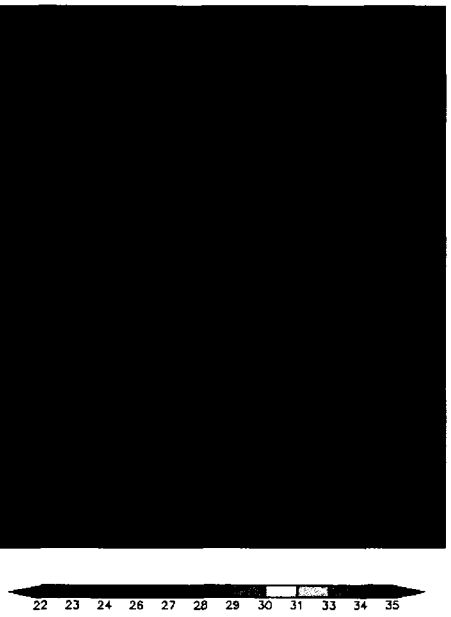

Figure 5.2 Surface temperature in degrees Celsius at 2100 UTC for the uniform soil moisture experiment.

5.2.2 Sensible heat flux

The effects of soil moisture on microclimate response to the burn scar can be further investigated by analyzing the sensible heat flux field induced by this burn scar

Reproduced with permission of the copyright owner. Further reproduction prohibited without permission.

with uniform soil moisture. Results in this section are compared with those from section 4.2.3 in the last chapter.

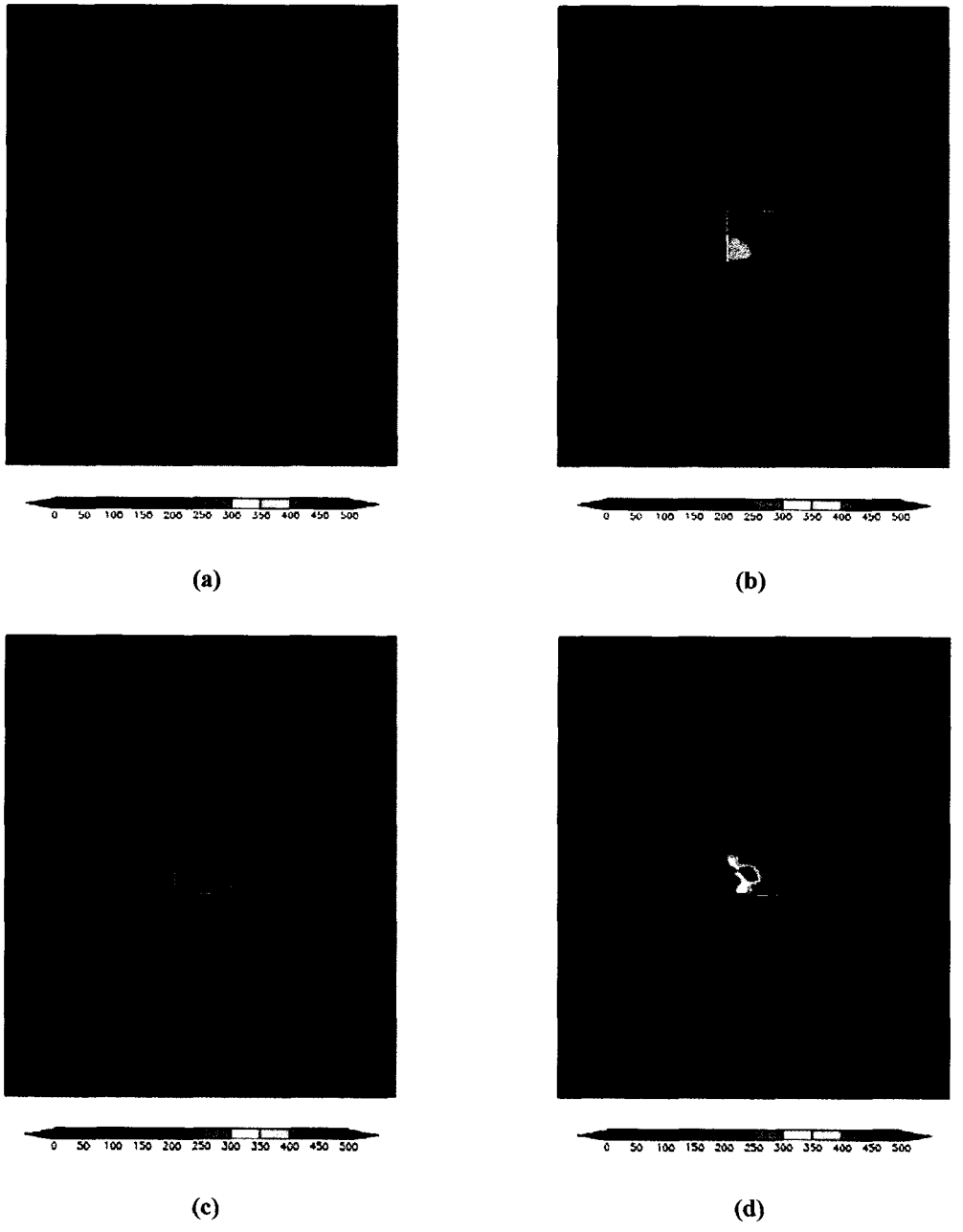

Figure 5.3 Sensible heat flux in $W \cdot m^{-2}$ at (a) 1500 UTC, (b) 1800 UTC, (c) 1900 UTC and (d) 2000 UTC for the uniform soil moisture experiment.

Reproduced with permission of the copyright owner. Further reproduction prohibited without permission.

Figure 5.3 shows the sensible heat flux from 1500 UTC to 2000 UTC. Comparing Figure 5.3(a) with Figure 4.12 shows that early in the simulation, the sensible heat flux was up to 30 $W \cdot m^{-2}$ higher than over the drier burn scar at 1500 UTC. Later in the simulation at 1800 UTC and1900 UTC, the values of sensible heat flux are nearly identical in the two experiments as shown by comparing Figure 5.3(b) with Figure 4.13 and Figure 5.3(c) with Figure 4.14. However, by 2000 UTC, differences of up to 150 $W \cdot m^{-2}$ are seen in the pattern of sensible heat flux over the burn scar with the higher soil moisture in Figure 5.3(d) compared to Figure 4.15. This trend continued at 2100 UTC as seen in Figure 5.4, where lower values were predicted in the experiment with the drier burn scar (Figure 4.16) than the current experiment with the uniform soil moisture. A more widespread region of values greater than 120 $W \cdot m^{-2}$ were predicted over the burn scar as illustrated in Figure 5.4.

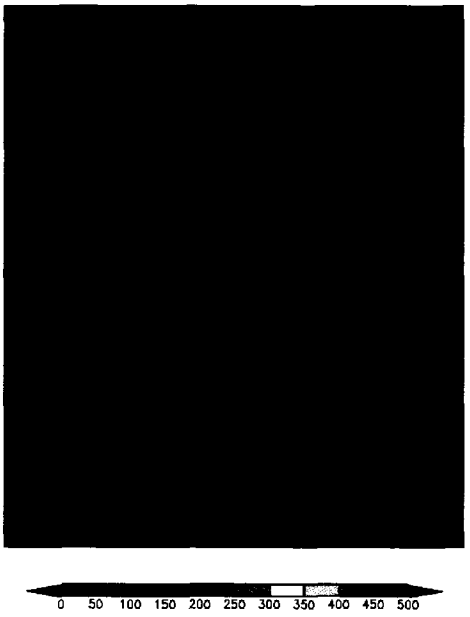

Figure 5.4 Sensible heat flux in $W \cdot m^{-2}$ at 2100 UTC for the uniform soil moisture experiment.

5.2.3 Latent heat flux

Reproduced with permission of the copyright owner. Further reproduction prohibited without permission.

The effects of soil moisture can be further examined in the latent heat flux field. The uniform soil moisture field in this experiment yields a different evolution of latent heat flux.

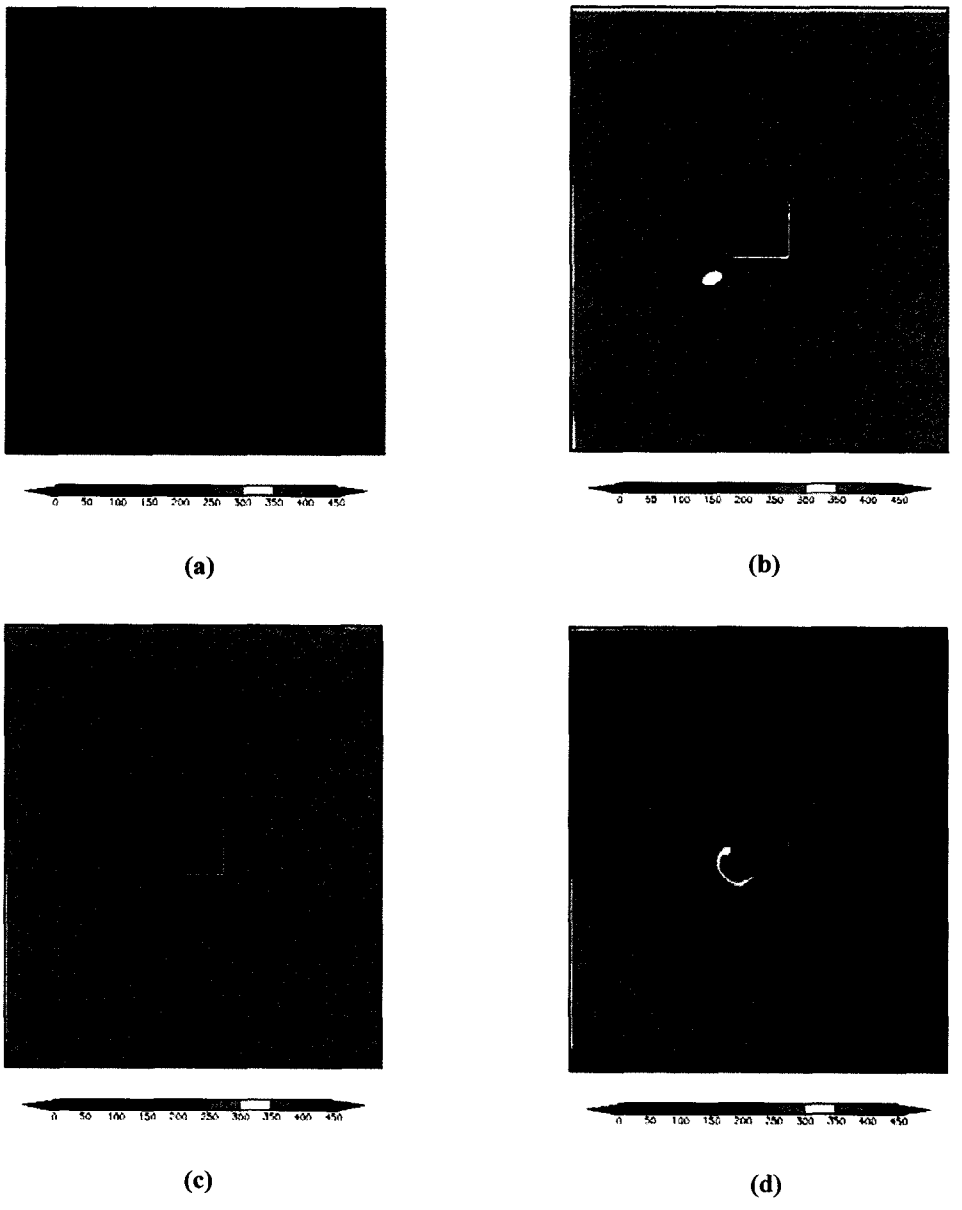

Figure 5.5 Latent heat flux in $W \cdot m^{-2}$ at (a) 1500 UTC, (b) 1800 UTC, (c) 1900 UTC and (d) 2000 UTC for the uniform soil moisture experiment.

Reproduced with permission of the copyright owner. Further reproduction prohibited without permission.

Figure 5.5 shows the latent heat flux evolution from 1500 UTC to 2000 UTC in $W \cdot m^{-2}$. Comparing Figure 5.5(a) to Figure 4.17 shows that the drier burn scar has latent heat flux values in the scar region of 50 $W \cdot m^{-2}$ compared to 30 $W \cdot m^{-2}$ in the uniform moisture experiment. Three hours later at 1800 UTC, both Figure 5.5 (b) for the uniform soil moisture field and Figure 4.18 for the original drier burn scar show values of 0 $W \cdot m^{-2}$. At 1900 UTC, both experiments continue to show similar latent heat flux fields as seen in Figure 5.5(c) and Figure 4.19. Moving forward an hour in the simulation to 2000 UTC, the drier burn scar experiment results in Figure 4.20 show a greater contrast in latent heat flux between the burn scar and the surrounding environment. Maximum values over the surrounding area reached 450 $W \cdot m^{-2}$ and values over the scar were below 50 $W \cdot m^{-2}$ in the original experiment with the drier burn scar. In the uniform soil moisture experiment shown in Figure 5.5(d), values over the burn scar were predicted to be near 50 $W \cdot m^{-2}$ with a small area near 0 $W \cdot m^{-2}$. Surrounding the burn scar the latent heat flux values were over 400 $W \cdot m^{-2}$. A region of lower values extended to the west and southwest of the burn scar were predicted in both experiments. This region is larger in the drier burn scar experiment than in the uniform soil moisture experiment.

Reproduced with permission of the copyright owner. Further reproduction prohibited without permission.

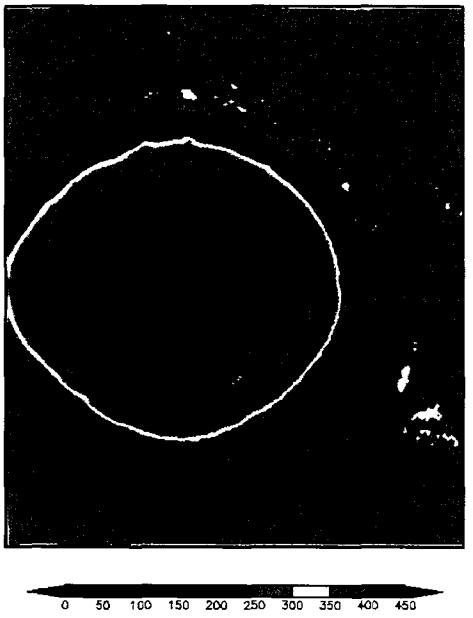

Figure 5.6 Latent heat flux in $W \cdot m^{-2}$ at (a) 2100 UTC for the uniform soil moisture experiment.

Figure 5.6 shows the latent heat flux at 2100 UTC. The flux field is similar to that of the drier burn scar seen in Figure 4.21. The details of the flux values differ slightly, but in general the magnitude and pattern are similar.

5.2.4 Vertical velocity

The vertical velocity field is examined to view the effects of soil moisture differences on the development of convection. The results from this uniform soil moisture experiment are compared with section 4.2.5 for the original experiment with the drier soil moisture in the last chapter.

Reproduced with permission of the copyright owner. Further reproduction prohibited without permission.

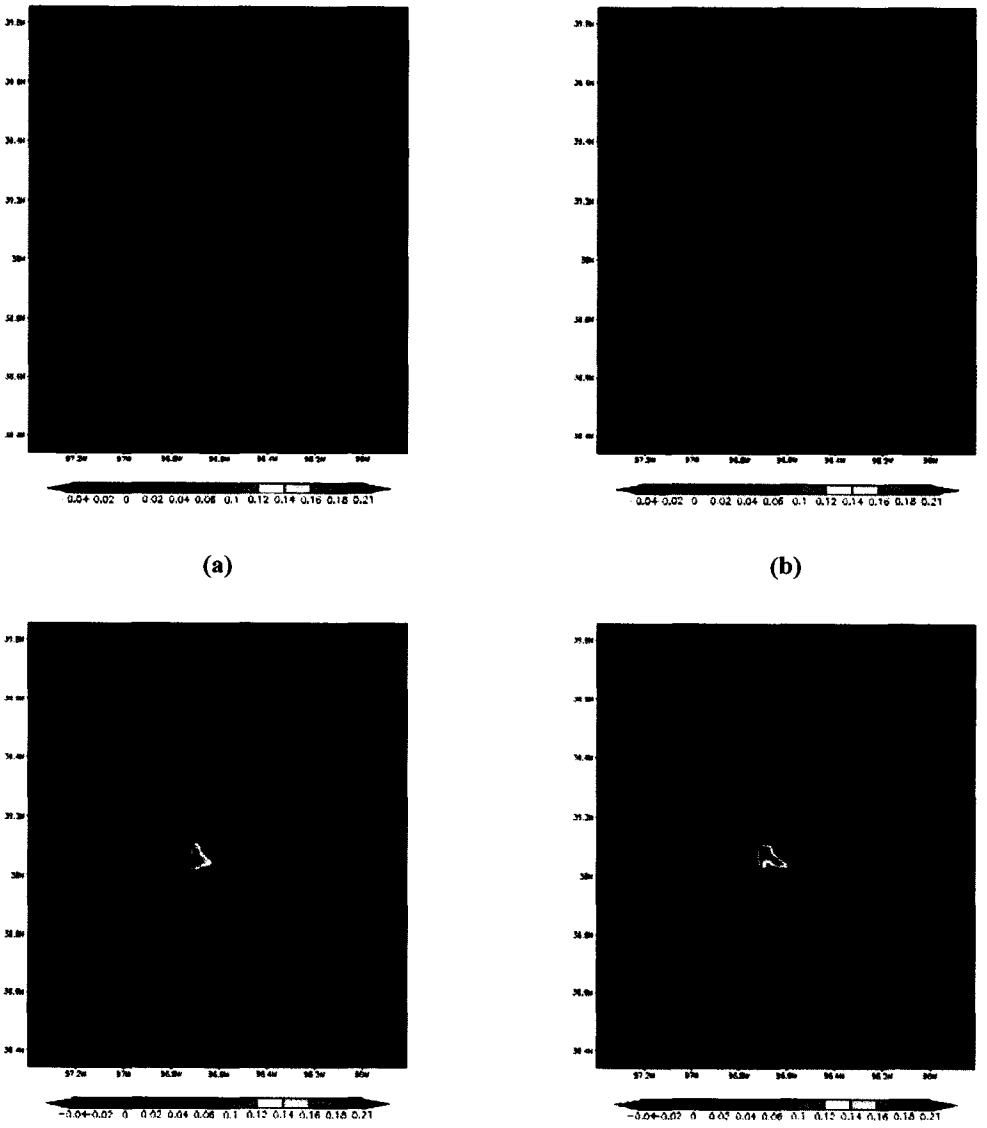

Figure 5.7 Vertical velocity in $m \cdot s^{-1}$ at 48 m (a) 1500 UTC, (b) 1800 UTC, (c) 1900 UTC and (d) 2000 UTC for the uniform soil moisture experiment.

Figure 5.7 shows the vertical velocity at the first vertical level in the model (48 m above the ground). At 1500 UTC, the strongest upward motion is seen in Figure 4.22 of the drier burn scar experiment with values of 0.018 $m \cdot s^{-1}$, compared to 0.012 $m \cdot s^{-1}$ seen in Figure 5.7(a). At 1800 UTC and 1900 UTC, little difference is seen in the vertical

Reproduced with permission of the copyright owner. Further reproduction prohibited without permission.

velocity at 48 m, which was analyzed by comparing Figure 5.7(b) with .Figure 4.24 and Figure 5.7(c) with Figure 4.27. Differences are seen at 2000 UTC when comparing Figure 5.7(d) with Figure 4.29. Stronger upward motion, with values of 0.21 $m \cdot s^{-1}$ in the uniform moisture field compared to 0.16 $m \cdot s^{-1}$ in the drier burn scar experiment. The region of upward motion in the current experiment is also more elongated across the burn scar.

Examining the cross-sections of vertical velocity shows the vertical extent of the motion induced by the burn scar. These results are compared with findings from the drier burn scar experiment, presented in section 4.2.5 in the previous chapter.

Reproduced with permission of the copyright owner. Further reproduction prohibited without permission.

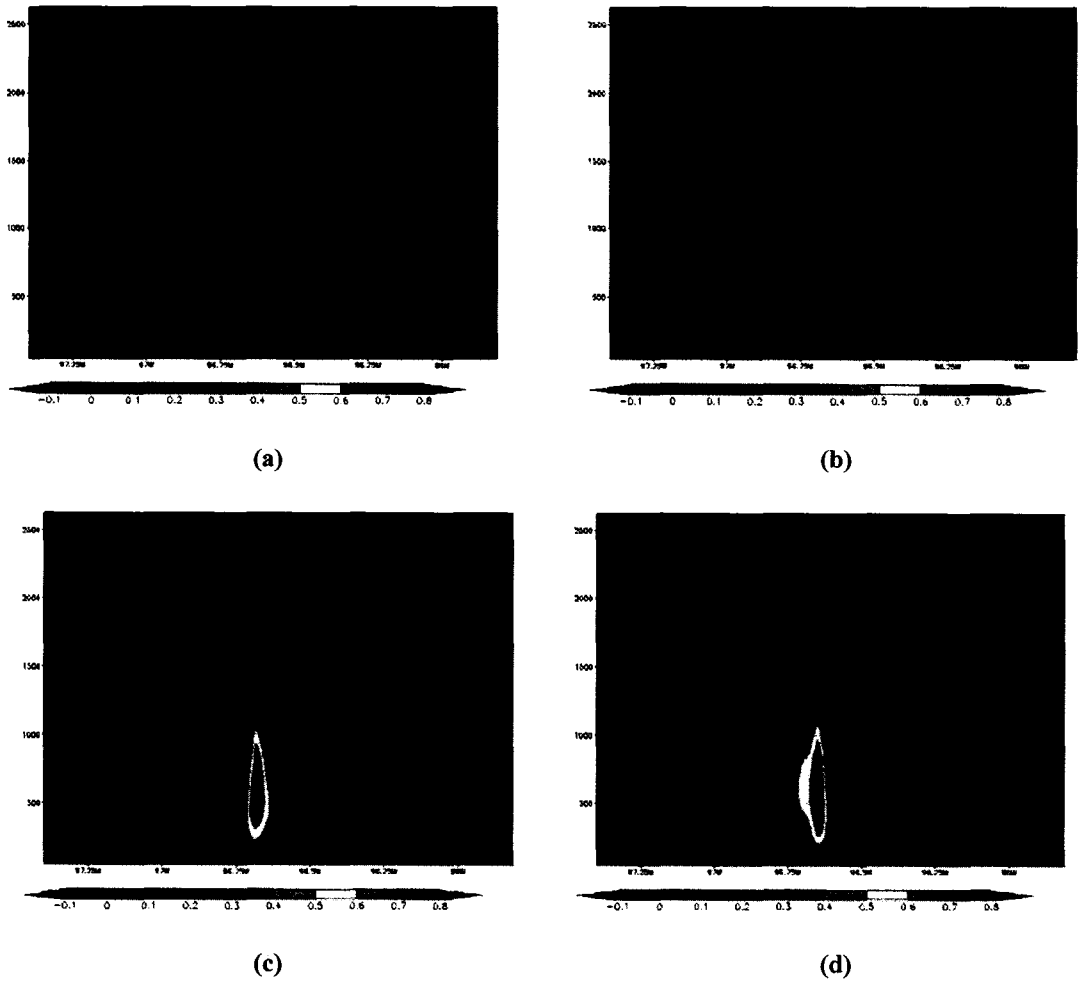

Figure 5.8 Cross section of vertical velocity in m s^{-1} taken at 39.05°N at (a) 1500 UTC, (b) 1800 UTC, (c) 1900 UTC, and (d) 2000 UTC for the uniform soil moisture experiment.

The cross-section of vertical velocity shows that this experiment with uniform soil moisture has weaker upward motion early in the simulation as seen at 1500 UTC in Figure 5.8(a) compared to Figure 4.23 and for 1800 UTC in Figure 5.8(b) compared to Figure 4.25. With time, the upward motion becomes stronger in the uniform soil moisture experiment than in the drier burn scar simulation as seen by comparing the 1900 UTC results of 0.8 m s^{-1} in Figure 5.8(c) with the 0.7 m·s^{-1} in Figure 4.28 and the 2000 UTC results in Figure 5.8 (d) of 0.8 m·s^{-1} with that of 0.5 m·s^{-1} in Figure 4.30.

Reproduced with permission of the copyright owner. Further reproduction prohibited without permission.

5.2.5 Cloud Water

The cloud water field is examined to determine the effects the differences in vertical velocity between the two simulations had on the resulting cloud fields.

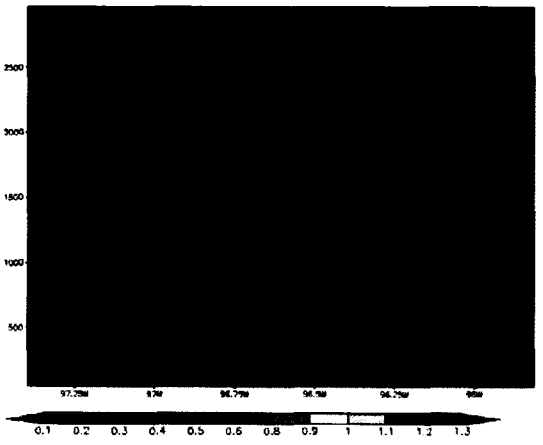

Figure 5.9 Vertical cross-section of cloud water taken at y=80 (39.05°N) in g·kg^{-1} at 1850 UTC for initial conditions of uniform soil moisture.

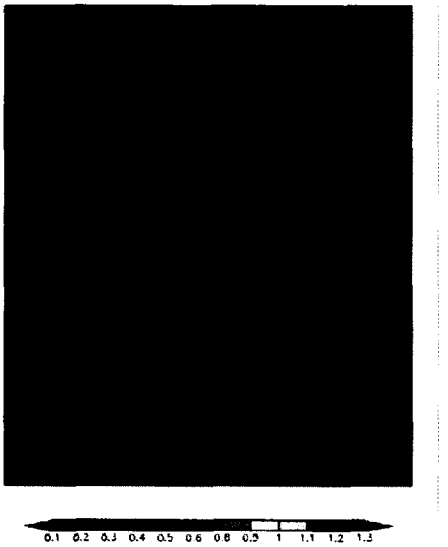

Figure 5.10 Cloud water at model level 8 (1044 m) in g·kg^{-1} at 1850 UTC for initial conditions of uniform soil moisture.

Figure 5.9 shows the vertical cross-section of cloud water at 1850 UTC. Cloud was predicted near 1044 m with concentrations of 0.22 g·kg^{-1}. A slice taken through this cloud is shown in Figure 5.10 and depicts the horizontal extent of cloud water at model level 8. The burn scar region is outlined in the graphic. Comparing Figure 5.9 with Figure 4.31 shows that the cloud over the drier burn scar develops with a higher, second layer of cloud already predicted by 1850 UTC.

Reproduced with permission of the copyright owner. Further reproduction prohibited without permission.

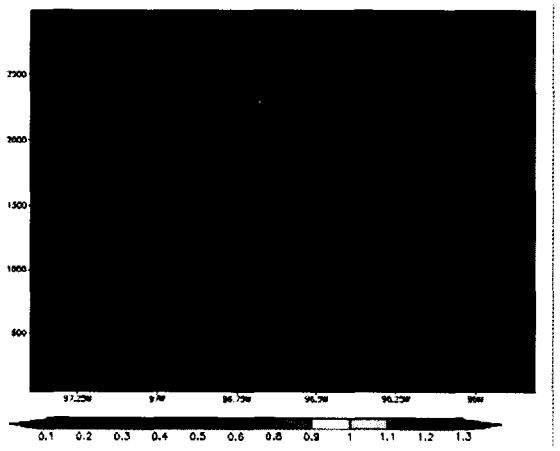

Figure 5.11 Vertical cross-section of cloud water taken at y=80 (39.05°N) in g·kg^{-1} at 1930 UTC for initial conditions of uniform soil moisture.

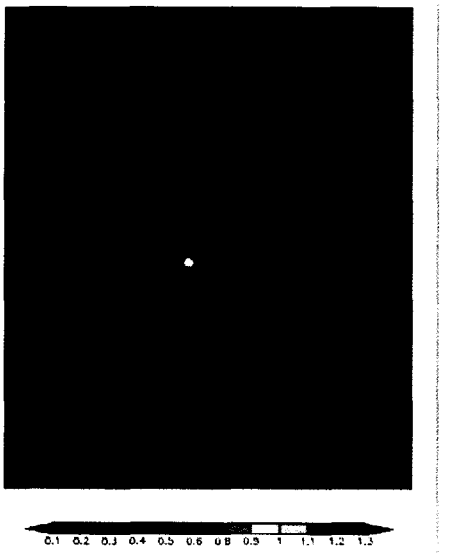

Figure 5.12 Cloud water at model level 13 (2292 m) in g·kg^{-1} at 1930 UTC for initial conditions of uniform soil moisture.

At 1930 UTC a higher level of cloud is now seen at 2300 m in the vertical cross-section of cloud water in Figure 5.11. A horizontal slice taken near 2300 meters, at the 13th vertical level of the simulation is depicted in Figure 5.12 and shows a widespread area of cloud at this level with values up to 0.9 g·kg^{-1}. Comparing these results to those depicted in Figure 4.33 and Figure 4.34 show that the drier burn scar has a greater horizontal extent of cloud. The relative location and concentrations of cloud water are similar.

Reproduced with permission of the copyright owner. Further reproduction prohibited without permission.

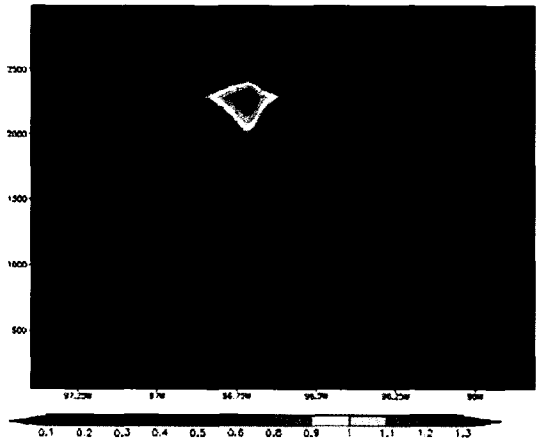

Figure 5.13 Vertical cross-section of cloud water taken at y=80 (39.05°N) in g·kg^{-1} at 2000 UTC for initial conditions of uniform soil moisture.

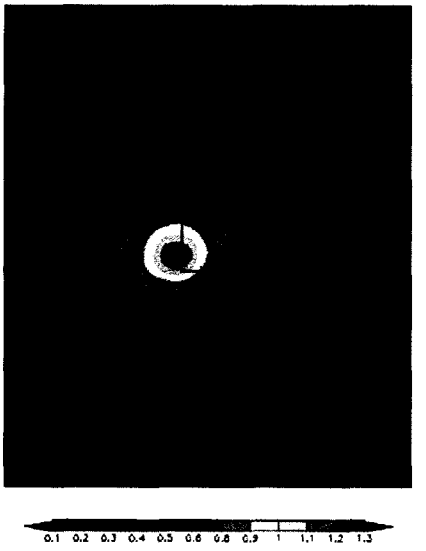

Figure 5.14 Cloud water at model level 13 (2292 m) in g·kg^{-1} at 2000 UTC for initial conditions of uniform soil moisture.

By 2000 UTC, the cloud area has expanded both in the upper layer and the lower layer as can be seen in Figure 5.13. Comparing with Figure 4.35 for the drier burn scar, the pattern looks similar with slightly higher values in the uniform soil moisture experiment. However, analysis of the slices taken at model level 13 in Figure 5.14 and Figure 4.36 show a much wider horizontal extent of cloud in the drier burn scar experiment, although again, the maximum concentrations of cloud water are slightly lower than found in the uniform soil moisture experiment.

5.2.6 Soundings

Soundings over the burn scar and the surrounding environment were examined to see how soil moisture differences in the burn scar affected the vertical structure of the atmosphere.

Reproduced with permission of the copyright owner. Further reproduction prohibited without permission.

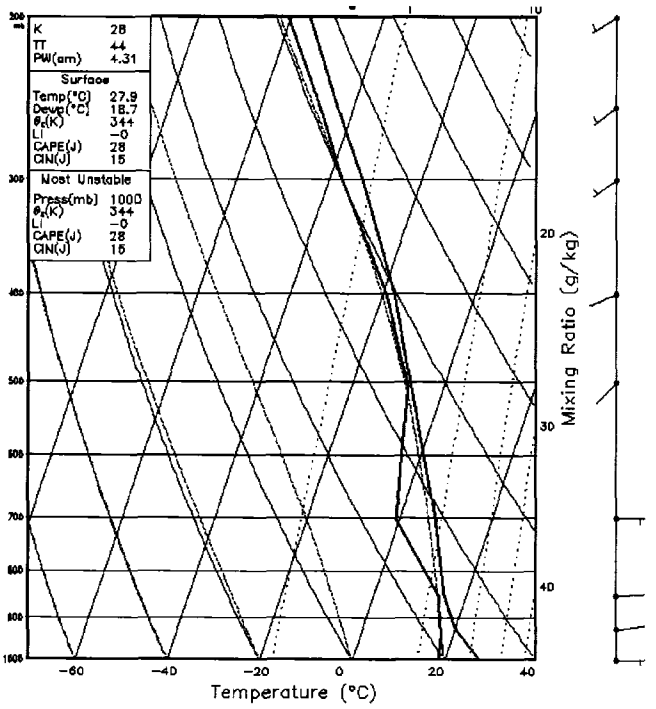

(a)

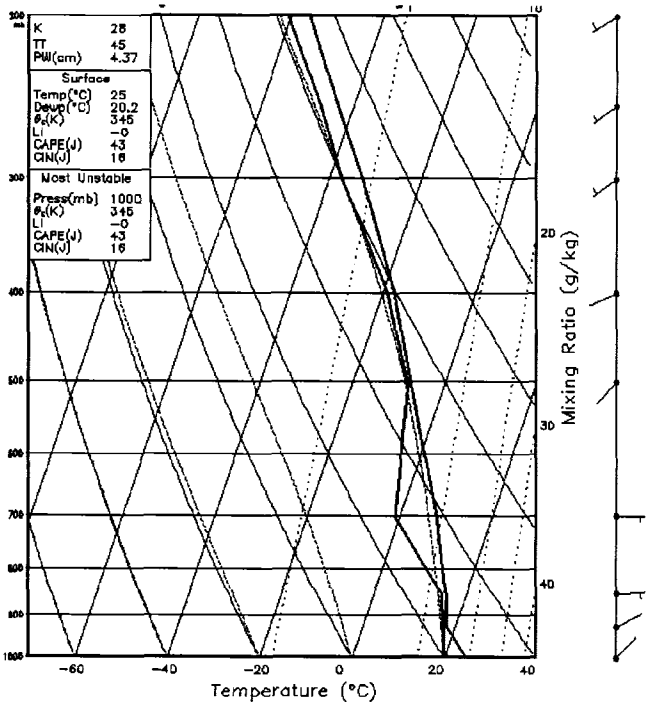

(b)

Figure 5.15 Vertical sounding of the atmosphere taken at 1900 UTC over (a) the burn scar and (b) the surrounding environment for the uniform soil moisture experiment.

Reproduced with permission of the copyright owner. Further reproduction prohibited without permission.

At 1900 UTC, Figure 5.15(a) shows a vertical sounding over the burn scar, while Figure 5.15(b) shows a sounding over the surrounding environment. The domain in this experiment has uniform soil moisture, so the main differences seen between the burn scar and the surrounding environment can be attributed to differential heating. The surface temperature over the burn scar is nearly 3°C warmer than that of the surrounding area. This difference is extended into the lower atmosphere which appears warmer and therefore drier (less humid). CAPE values show little difference with 43 $J \cdot kg^{-1}$ over the surrounding environment and slightly lower value of 28 $J \cdot kg^{-1}$ over the burn scar. Comparing Figure 5.15(a) with Figure 4.38(a), showing the sounding over the drier burn scar, yields little difference between the two, with the lower levels of the sounding over the drier burn scar showing drier conditions below 800 hPa.

5.3 Wind speed – Higher Wind Experiment

The sensitivity of the simulations to the wind field was tested by using the actual sounding data from 30 August 2003. As explained in Chapter 3, the wind field was damped by 75% in the original experiment, to better focus on the changes induced by the burn scar and to reduce advective effects of the strong winds in the actual sounding. In this experiment, the actual measured wind profile, as seen in Figure 5.16, was used to initialize the model.

Reproduced with permission of the copyright owner. Further reproduction prohibited without permission.

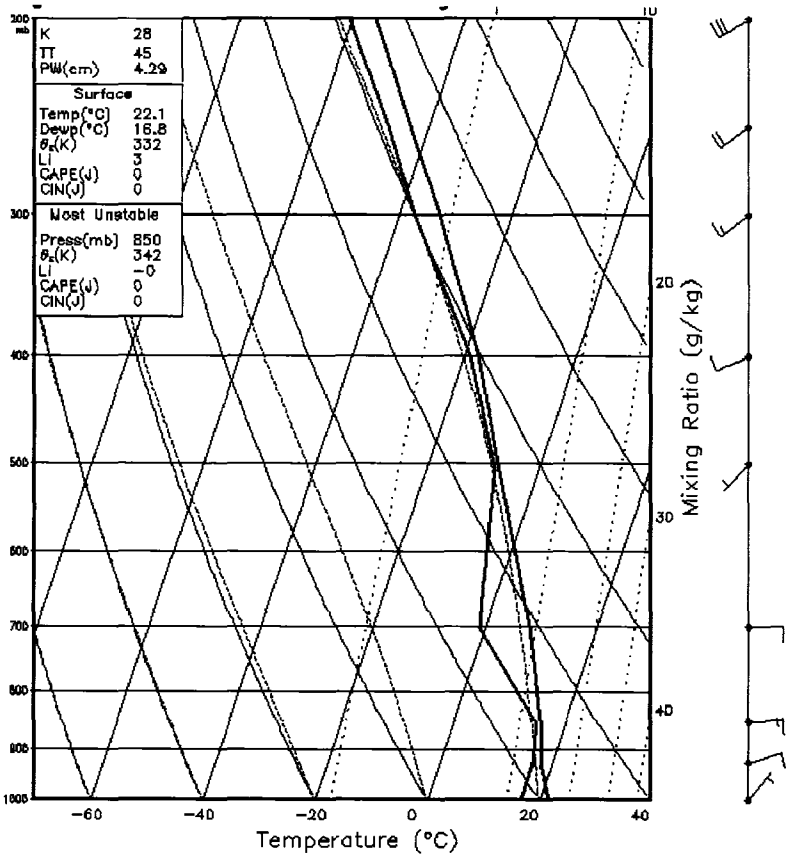

Figure 5.16 Actual sounding taken 1200 UTC 20 August 2003.

5.3.1 Surface temperature

Since the wind field has increased substantially throughout the atmosphere, advective effects are expected to modify the temperature field predicted in the original experiment and described in section 4.2.1 in the previous chapter.

Reproduced with permission of the copyright owner. Further reproduction prohibited without permission.

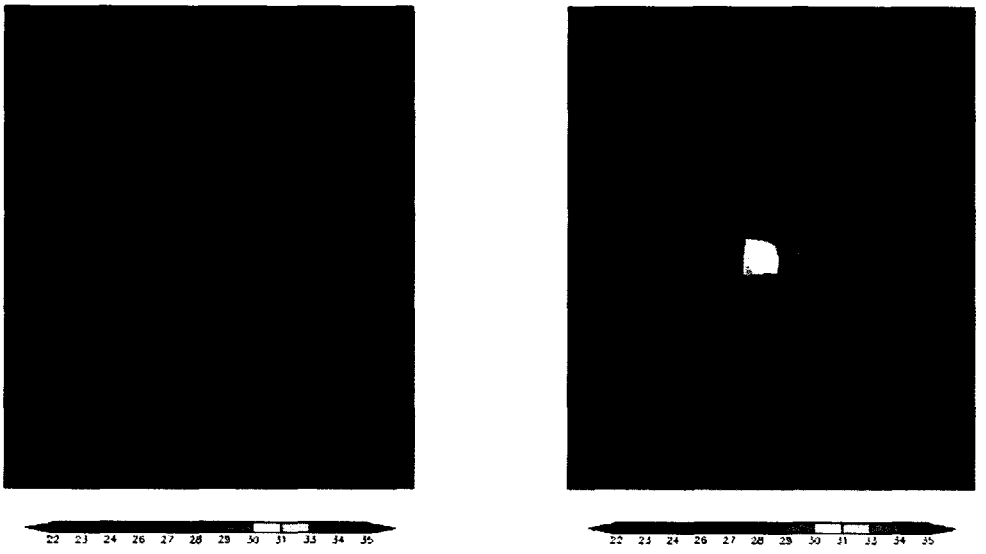

(a) (b)

Figure 5.17 Surface temperature in degrees Celsius at (a) 1500 UTC and (b) 1800 UTC for the higher wind experiment.

Surface temperature is depicted in Figure 5.17 at (a) 1500 UTC and (b) 1800 UTC. These results can be compared to those from Figure 4.1 and Figure 4.2. At 1500 UTC, in Figure 5.17(a), the higher surface winds appear to have resulted in slightly lower surface temperatures, by 1.5°F, over the burn scar, and warmer temperatures can be seen advecting over the surrounding environment to the southwest of the burn scar. By 1800 UTC, after further warming, Figure 5.17(b) shows temperatures 3-5°F cooler than seen in the lighter wind experiment depicted in Figure 4.2. In addition, the effects of advection of the warmer air over the burn scar to the surrounding environment extend farther to the southwest in Figure 5.17(b).

Reproduced with permission of the copyright owner. Further reproduction prohibited without permission.

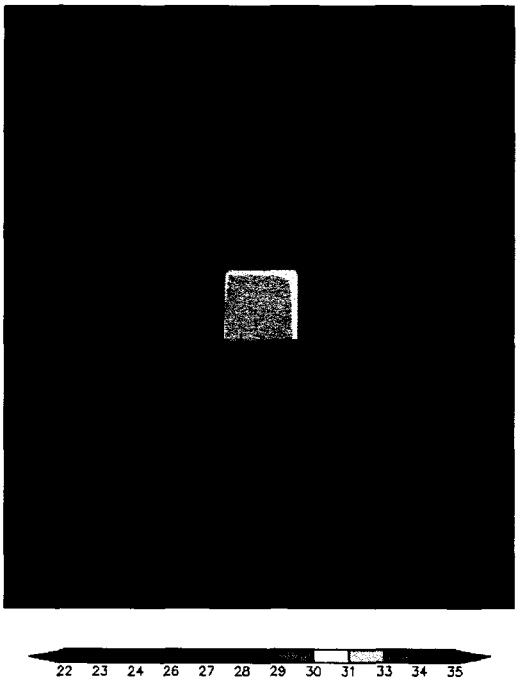

Figure 5.18 Surface temperature in degrees Celsius at 1900 UTC for the higher wind experiment.

Moving forward an hour to 1900 UTC, surface heating continues and the burn scar region has reached temperatures between 87°F and 89°F as seen in Figure 5.18. These values are 5-9°F lower than those predicted in Figure 4.3. In addition, the difference between the burn scar and the surrounding environment at 1900 UTC in the strong wind experiment is 11°F, compared to 17°F in Figure 4.3 from the original experiment. Also, the warmer values extending from the southwest corner of the scar imply that advected air from the burn scar has reached the western edge of the domain.

5.3.2 Surface wind and divergence

The surface wind and divergence fields are compared with those from the original experiment presented in section 4.2.2.

Reproduced with permission of the copyright owner. Further reproduction prohibited without permission.

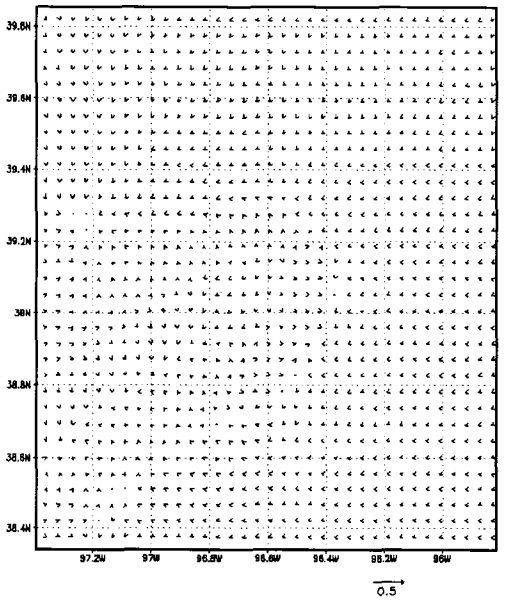

Figure 5.19 Winds vectors at 10 m at 1500 UTC for the higher wind experiment.

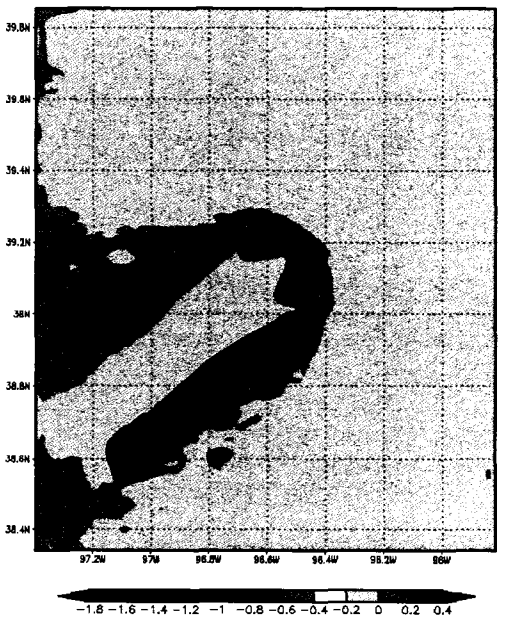

Figure 5.20 Surface divergence in s^{-1} (x1000) at 1500 UTC for the higher wind experiment.

Figure 5.19 depicts the wind anomaly vectors 30m above the surface at 1500 UTC. The strong northwesterly winds show little disturbance across the domain. Figure 5.20 shows the surface divergence in the wind field. Weak divergence with values on the order of 10^{-4} s^{-1} is seen along the northern and eastern boundaries of the burn scar. These values are approximately one third less than what was predicted in the original simulation shown in Figure 4.7. An area of convergence was predicted to the southwest of the burn scar with similar magnitude to that shown in Figure 4.7.

Reproduced with permission of the copyright owner. Further reproduction prohibited without permission.

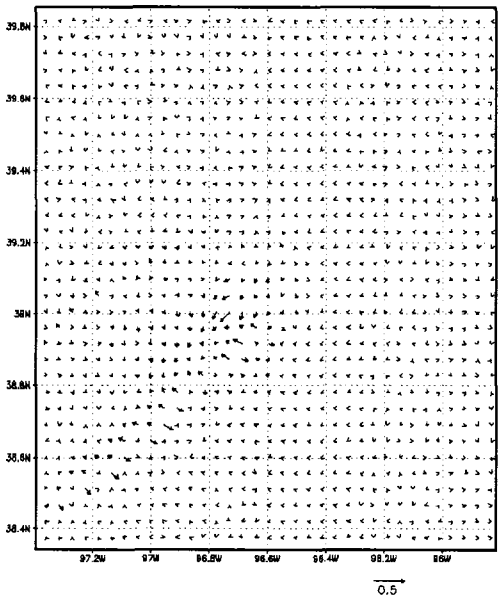

Figure 5.21 Winds vectors at 10 m at 1800 UTC for the higher wind experiment.

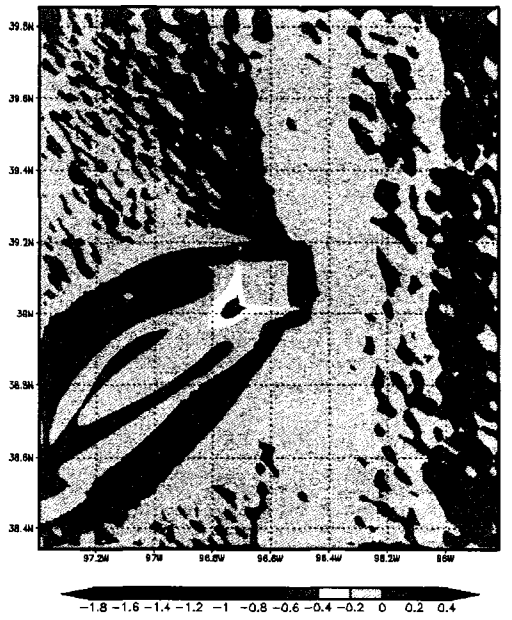

Figure 5.22 Surface divergence in s^{-1} (x1000) at 1800 UTC for the higher wind experiment.

By 1800 UTC, the surface wind anomaly vectors show disturbed flow extending well to the southwest of the burn scar region in

Figure 5.21, although the disturbance is not as strong as seen in Figure 4.8 due to the much stronger prevailing wind in this simulation. Figure 5.22 shows the main convergence regions have moved away from the burn scar and increased threefold over the 1500 UTC values to $3 \cdot 10^{-4}$ s^{-1} and now are a third stronger than the original simulation values shown in Figure 4.9. The area of convergence to the southwest of the scar has extended farther southwest and is twice as strong as the convergence values, but weaker than the convergence predicted in the original simulation shown in Figure 4.9, which stays closer to the burn scar region.

Reproduced with permission of the copyright owner. Further reproduction prohibited without permission.

5.3.3 Sensible heat flux

To evaluate the effects of the stronger wind flow on surface heating, the sensible heat flux was compared to results presented for the weaker wind simulation in section 4.2.3 in the previous chapter.

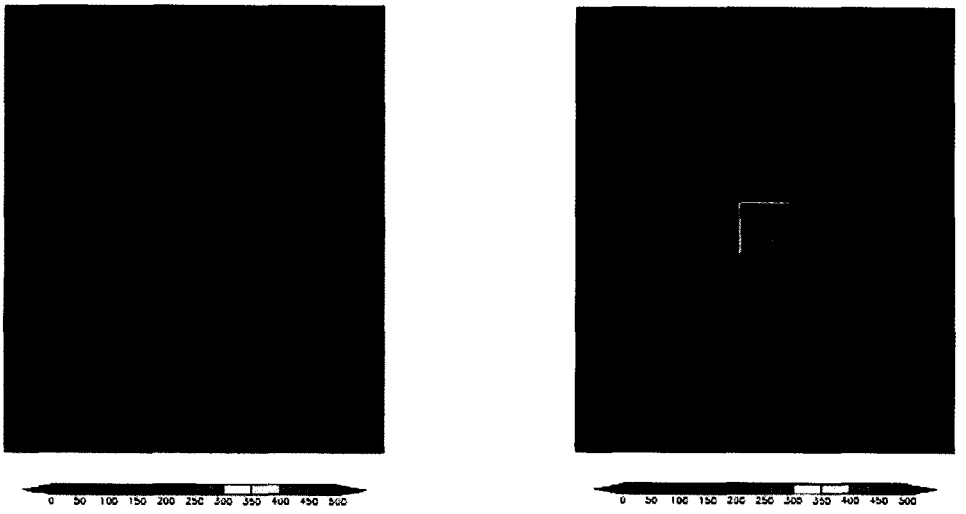

(a) (b)

Figure 5.23 Sensible heat flux in $W \cdot m^{-2}$ at (a) 1500 UTC and (b) 1800 UTC for the higher wind experiment.

Reproduced with permission of the copyright owner. Further reproduction prohibited without permission.

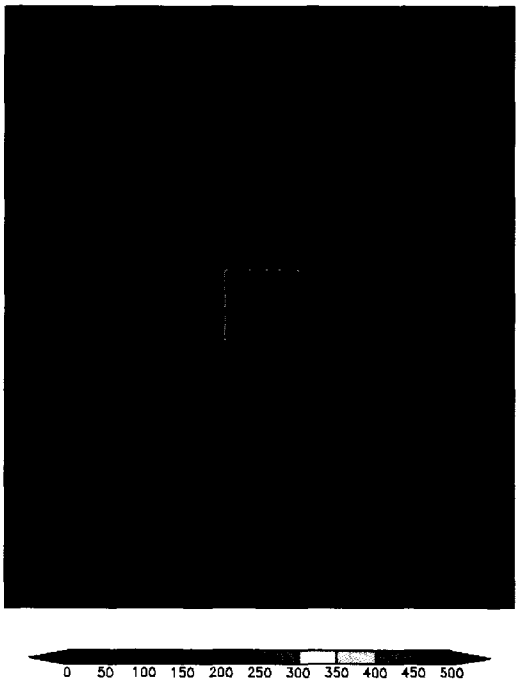

Figure 5.24 Sensible heat flux in $W \cdot m^{-2}$ at 1900 UTC for the higher wind experiment.

At 1500 UTC, the sensible heat flux over the burn scar in Figure 5.23(a) of 110 $W \cdot m^{-2}$ is more than twice as much as the 50 $W \cdot m^{-2}$ predicted in Figure 4.12 in the original experiment. Three hours later, at 1800 UTC, the sensible heat flux predicted in the current experiment, shown in Figure 5.23(b), was 50 $W \cdot m^{-2}$ higher than in Figure 4.13 where the highest value over the burn scar was 420 $W \cdot m^{-2}$. Values continue to be higher in the high wind simulation than in the original experiment at 1900 UTC as can be seen by comparing Figure 5.24 with Figure 4.14.

5.3.4 Latent heat flux

Latent heat flux predictions from this higher wind simulation are compared with results from the simulation in the last chapter presented in section 4.2.4.

Reproduced with permission of the copyright owner. Further reproduction prohibited without permission.

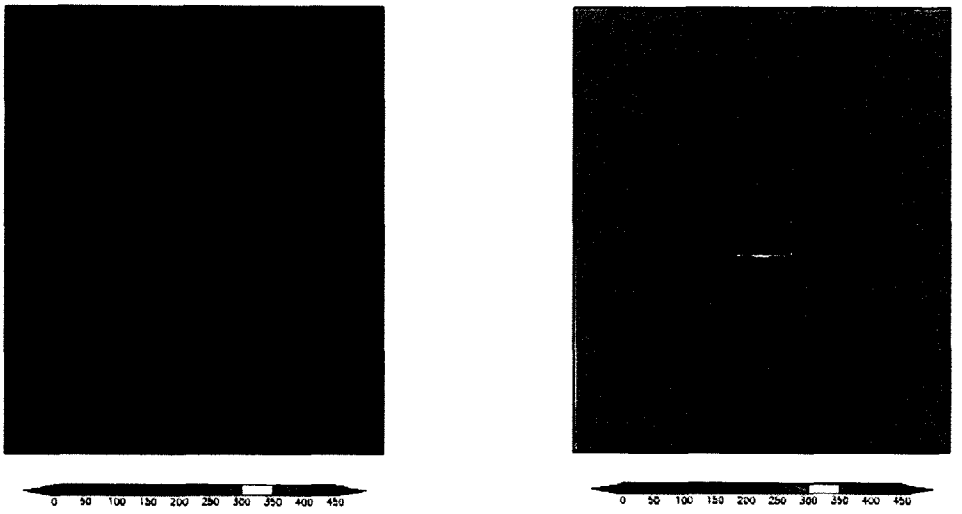

(a) (b)

Figure 5.25 Latent heat flux in $W \cdot m^{-2}$ at (a) 1500 UTC and (b) 1800 UTC for the higher wind experiment.

Figure 5.25 shows latent heat flux at 1500 UTC and 1800 UTC. Initially, little difference is evident between the results in the higher wind experiment in Figure 5.25(a) and those of the original experiment in Figure 4.17. The values are similar, with the higher wind experiment predicting higher values of latent heat flux downstream from the burn scar. By 1800 UTC, the latent heat flux is 50 $W \cdot m^{-2}$ higher in the higher wind experiment over both the burn scar and the surrounding environment in Figure 5.25(b) compared to Figure 4.18.

5.3.5 Vertical velocity

The vertical velocity field shows profound differences between the simulation with higher winds and that of the original burn scar described in the previous chapter. The results from the higher wind simulation were compared with those of section 4.2.5.

Reproduced with permission of the copyright owner. Further reproduction prohibited without permission.

The results in this section show many similarities to the surface divergence field presented in section 5.3.2.

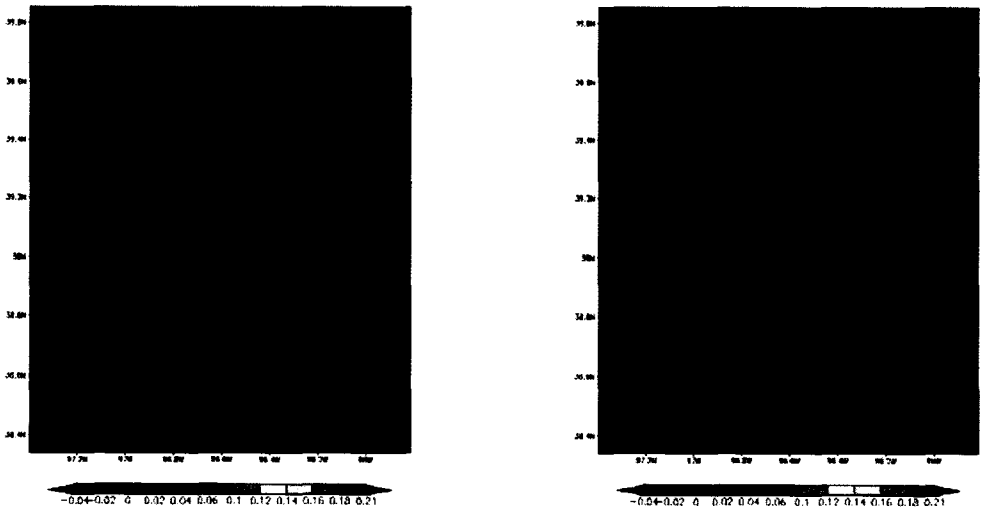

(a) (b)

Figure 5.26 Vertical velocity in $m \cdot s^{-1}$ at 48 m (a) 1500 UTC and (b) 1800 UTC for the higher wind experiment.

The influence of the stronger low level winds is apparent at 1500 UTC in Figure 5.26(a) where the orientation of the upward motion induced by the burn scar extends southwestward away from the burn scar boundary. Although the magnitude of the vertical motion is similar between the two experiments, the location of motion is very different from Figure 4.22 in which the upward and downward motion line up over the boundaries of the burn scar. Figure 5.26(b) shows the vertical motion at 1800 UTC. As was seen at 1500 UTC, the magnitude of the motion is similar to that seen in Figure 4.24, although the location shows even greater influence of the stronger horizontal motion with the region of upward motion to the southwest of the burn scar, while the main downward motion has moved away from the burn scar boundaries.

Reproduced with permission of the copyright owner. Further reproduction prohibited without permission.

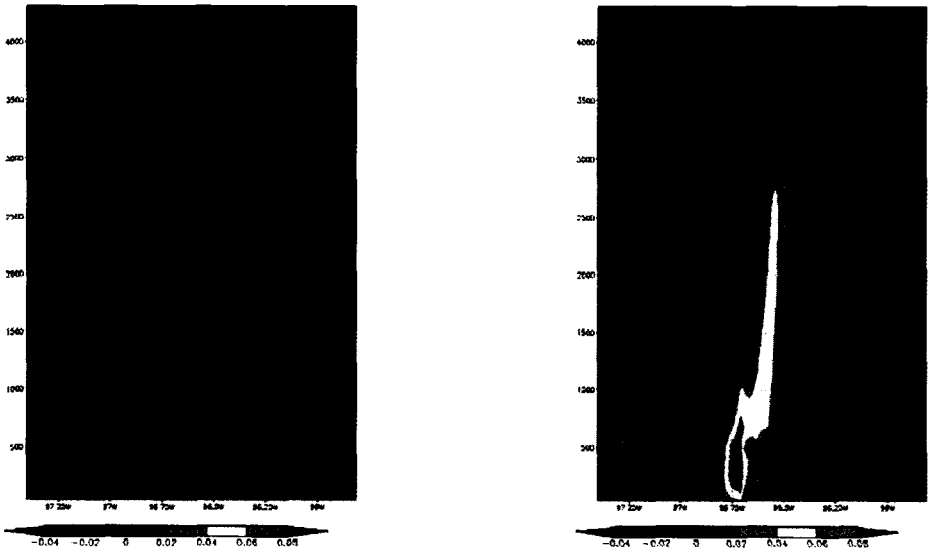

(a) (b)

Figure 5.27 Cross section of vertical velocity in m s^{-1} taken at 39.05°N at (a) 1500 UTC and (b) 1800 UTC for the higher wind experiment.

Figure 5.27 shows the vertical cross section of vertical velocity taken close to halfway along the north-south extent of the burn scar. In this higher wind simulation at 1500 UTC shown in Figure 5.27(a), the values of vertical velocity are similar to those predicted in the lighter wind simulation depicted in Figure 4.23. The most distinctive difference between the two simulations is the vertical extent of the larger values of vertical velocity which reach up to 3000 m in this high wind simulation as opposed to the vertical extent of 500 m seen in Figure 4.23.

Three hours later, at 1800 UTC, the simulation with the higher horizontal winds is shown in Figure 5.27(b) with the maximum upward motion of 0.07 $m \cdot s^{-1}$ and is substantially weaker than that predicted in the original simulation of 0.3 $m \cdot s^{-1}$ shown in Figure 4.25. As was seen at 1500 UTC, the vertical extent of the vertical velocity field is

Reproduced with permission of the copyright owner. Further reproduction prohibited without permission.

much greater for the higher wind simulation than in the lighter wind experiment. The concentrated regions of downward motion are elevated compared to the original experiment.

5.3.6 Soundings

Soundings over the burn scar and the surrounding environment were examined to see how the higher winds have affected the vertical structure of the atmosphere.

Reproduced with permission of the copyright owner. Further reproduction prohibited without permission.

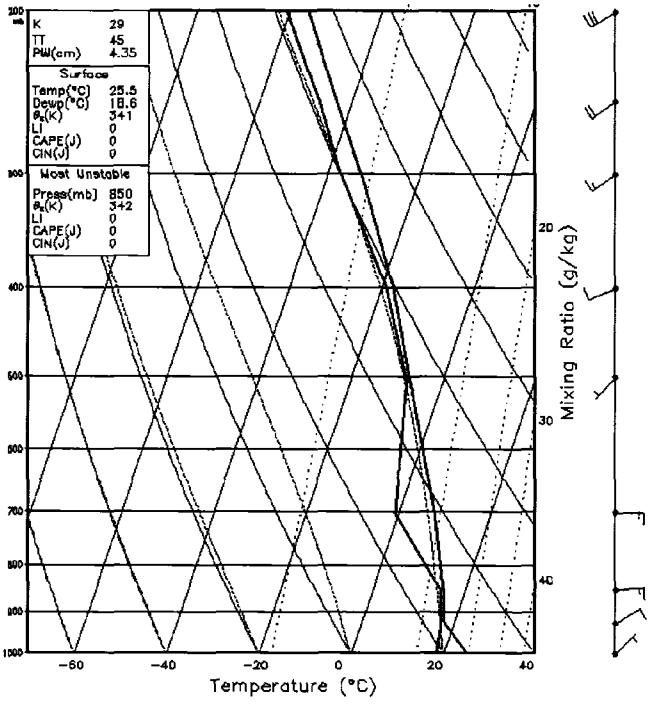

(a)

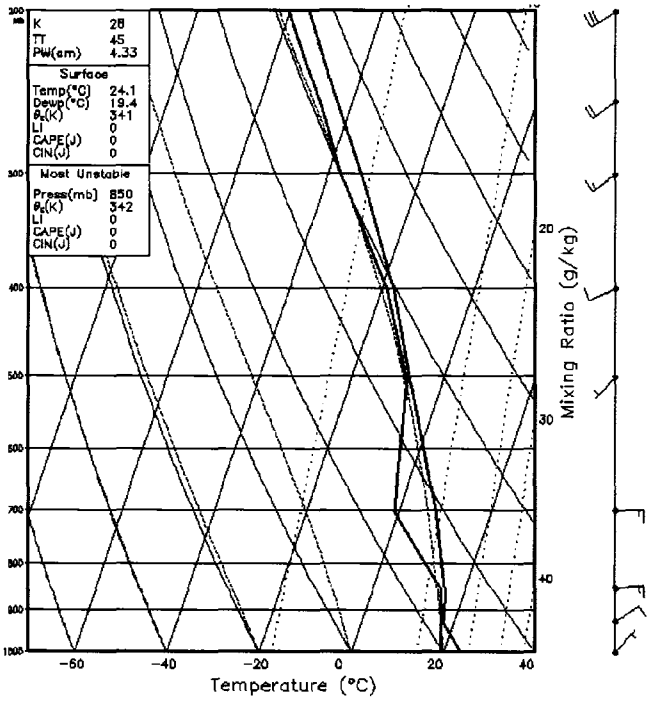

(b)

Figure 5.28 Vertical sounding of the atmosphere taken at 1800 UTC over (a) the burn scar and (b) the surrounding environment for the higher wind experiment.

Reproduced with permission of the copyright owner. Further reproduction prohibited without permission.

Figure 5.28 shows the soundings at 1800 UTC. The sounding over the burn scar (Figure 5.28(a)) shows a slightly warmer and drier surface, and thus a less stable surface layer. Otherwise, there is very little difference between the burn scar and the surrounding environment (Figure 5.28(b)) soundings. CAPE values over both locations are 0 $J \cdot kg^{-1}$.

The implications of these results are discussed in Chapter 6. Findings presented from these two simulations also provided ideas for future research presented in Chapter 7.

Reproduced with permission of the copyright owner. Further reproduction prohibited without permission.

Chapter 6

Discussion

6.1 Introduction

Each aspect of the findings of this project are highlighted in this chapter and described in terms of implications to forecasting for regions encompassing burn scars. This includes expected alterations in surface temperature and wind fields as well as influences of the burn scar on cloud fields, updrafts and precipitation patterns associated with convection, and the potential for electrification of the clouds.

6.2 Burn scar effects

The presence of a burn scar provided a significant perturbation to the surrounding environment. The microclimate of the domain was affected and convection was induced over the burn scar. Cloud developed due to the convection, and the results were sensitive to both the soil moisture of the burn scar and the initial wind speed over the domain.

6.3 Microclimate modification

The effects of the presence of the burn scar in the environment influences the microclimate near the burn scar early in the simulation. The burn scar showed greater heating that resulted in a higher temperature than the surrounding environment.

Reproduced with permission of the copyright owner. Further reproduction prohibited without permission.

During the initial simulation, a difference in surface temperature of 10°C developed between the burn scar and the surrounding environment at 1900 UTC (2 PM local time) as seen in Figure 4.3. This difference is higher than seen in the observational study of Amiro et al. (1999) where a 6°C temperature difference was observed between burn scars and unburned regions and the 5°C modeled by Chen et al. (2001), or the 3°C modeled by Mölders and Kramm (2007). The burn scar characteristics used in the simulation are uniform and depict a severe fire. In reality, the effects of a wildfire would be less uniform, as would the heating at the surface, which is why temperature changes over observed fire scars and those modeled by others were lower.

The sensible heat flux contrast between the burn scar and the surrounding environment shows a steady increase with time until the cloud shield created in the simulation covers the burn scar region and blocks solar heating. A 200% increase was seen over the burn scar in Figure 4.14. This is greater than the 10-20% observed by Amiro et al. (1999) over the first few years after the fire and the 5-25% predicted by Mölders and Kramm (2007). Again, the uniform severity of the burn scar simulated can be attributed to the magnitude of the increase compared to the surrounding environment. The blackening of the burn scar would decrease with time as vegetation begins to grow back in the area, thus increasing the albedo and moderating the sensible heat flux over the burn scar.

The simulated burn scar was given characteristics of a severe burn. Most of the vegetation was removed from the scar and the soil moisture was decreased, both of which act to decrease the predicted latent heat flux. Figure 4.20 shows that at 2000 UTC, the

Reproduced with permission of the copyright owner. Further reproduction prohibited without permission.

latent heat flux over the burn scar is near 50 $W \cdot m^{-2}$ while the surrounding environment with greater vegetation and soil moisture has a latent heat flux of 450 $W \cdot m^{-2}$.

6.4 Induced convection

Changes in the surface heat budget were sufficient to generate upward motion over the scar and to influence the wind flow pattern. The strength of the updraft was affected by the initial soil moisture of the burn area and the strength of the wind profile.

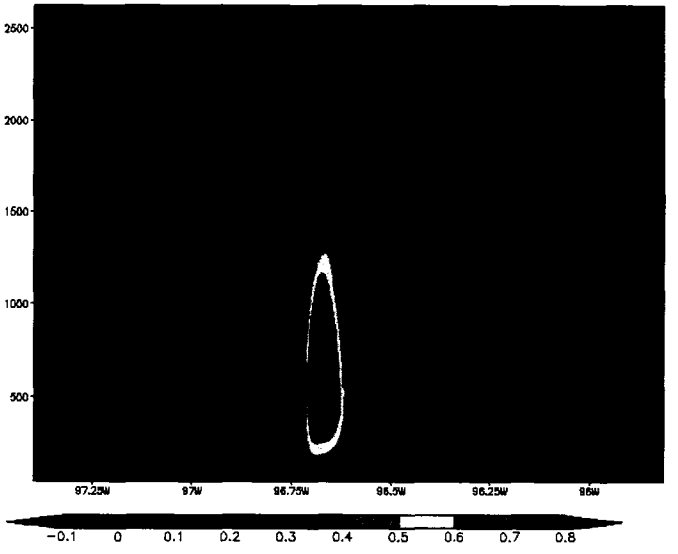

Figure 6.1 Cross section of vertical velocity in m s^{-1} taken at 39.05°N at 1910 UTC

Simulations showed the effects of the burn scar immediately after initialization of the model. The updraft achieved greatest strength of 1.0 $m \cdot s^{-1}$ near 1910 UTC at a height of 690 m (model level 6) as seen in Figure 6.1. Taking a horizontal slice at the height of 690 m shows the extent of the strongest region of upward motion. The vertical velocity field at 690 m is seen in Figure 6.2.

Reproduced with permission of the copyright owner. Further reproduction prohibited without permission.

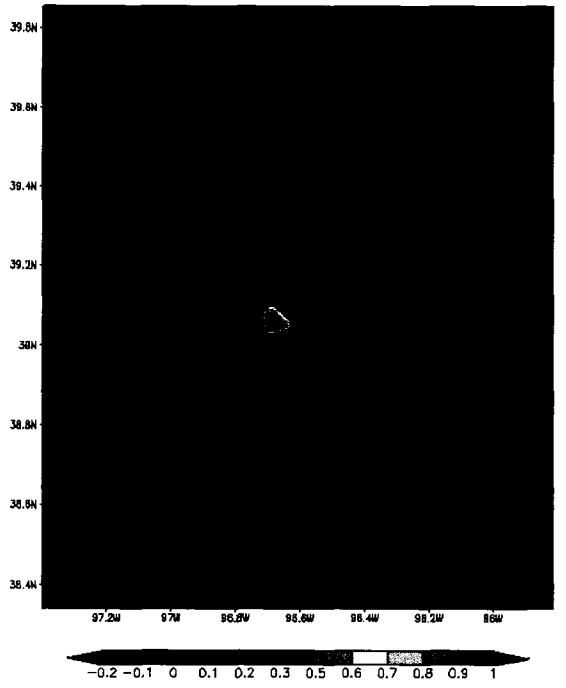

Figure 6.2 Vertical velocity at model level 6 (690 m) in $m \cdot s^{-1}$ at 1910 UTC.

Shortly after cloud began to form at 1850 UTC, gravity waves are evident in the vertical velocity field near the levels where cloud formed (as seen in figures 4.31 through 4.34 in Chapter 4) in the vicinity of the burn scar. The vertical velocity field in Figure 6.1 shows regions of alternating upward and downward vertical motion radiating from above the area of the main updraft that developed over the burn scar area.

Reproduced with permission of the copyright owner. Further reproduction prohibited without permission.

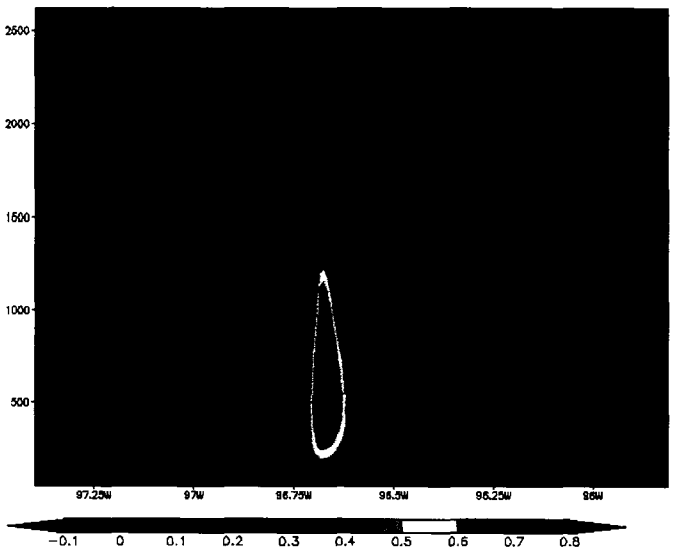

Figure 6.3 Cross section of vertical velocity in m s^{-1} at 39.05°N at 1920 UTC.

Over the next 30 minutes of simulation time, the vertical velocity field shown in Figure 6.3 through Figure 6.5 indicates the presence of gravity waves in the alternating upward and downward motion areas between 1000 m and 2500 m.

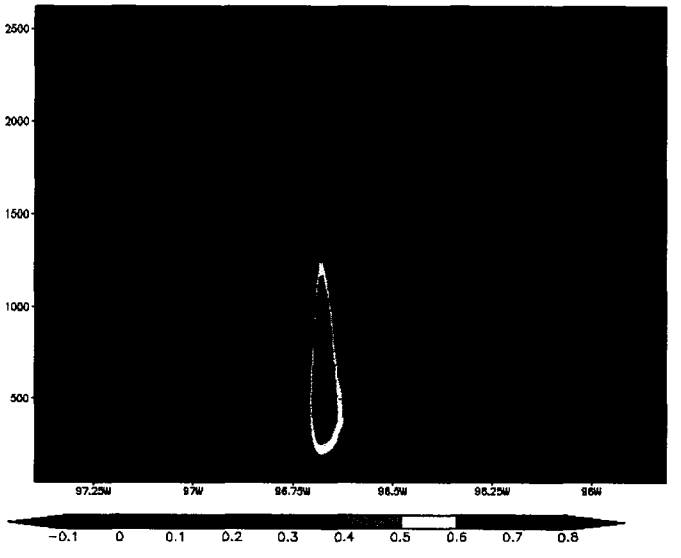

Figure 6.4 Cross section of vertical velocity in m s^{-1} taken at 39.05°N at 1930 UTC.

Reproduced with permission of the copyright owner. Further reproduction prohibited without permission.

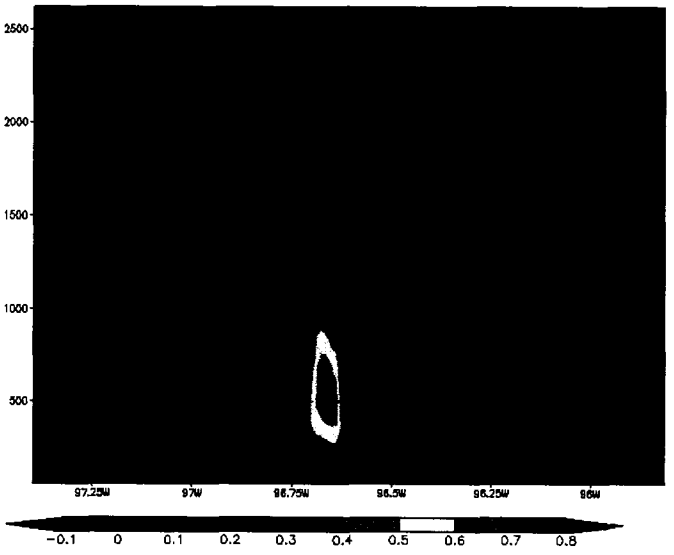

Figure 6.5 Cross section of vertical velocity in m s^{-1} taken at 39.05°N at 1940 UTC.

Reproduced with permission of the copyright owner. Further reproduction prohibited without permission.

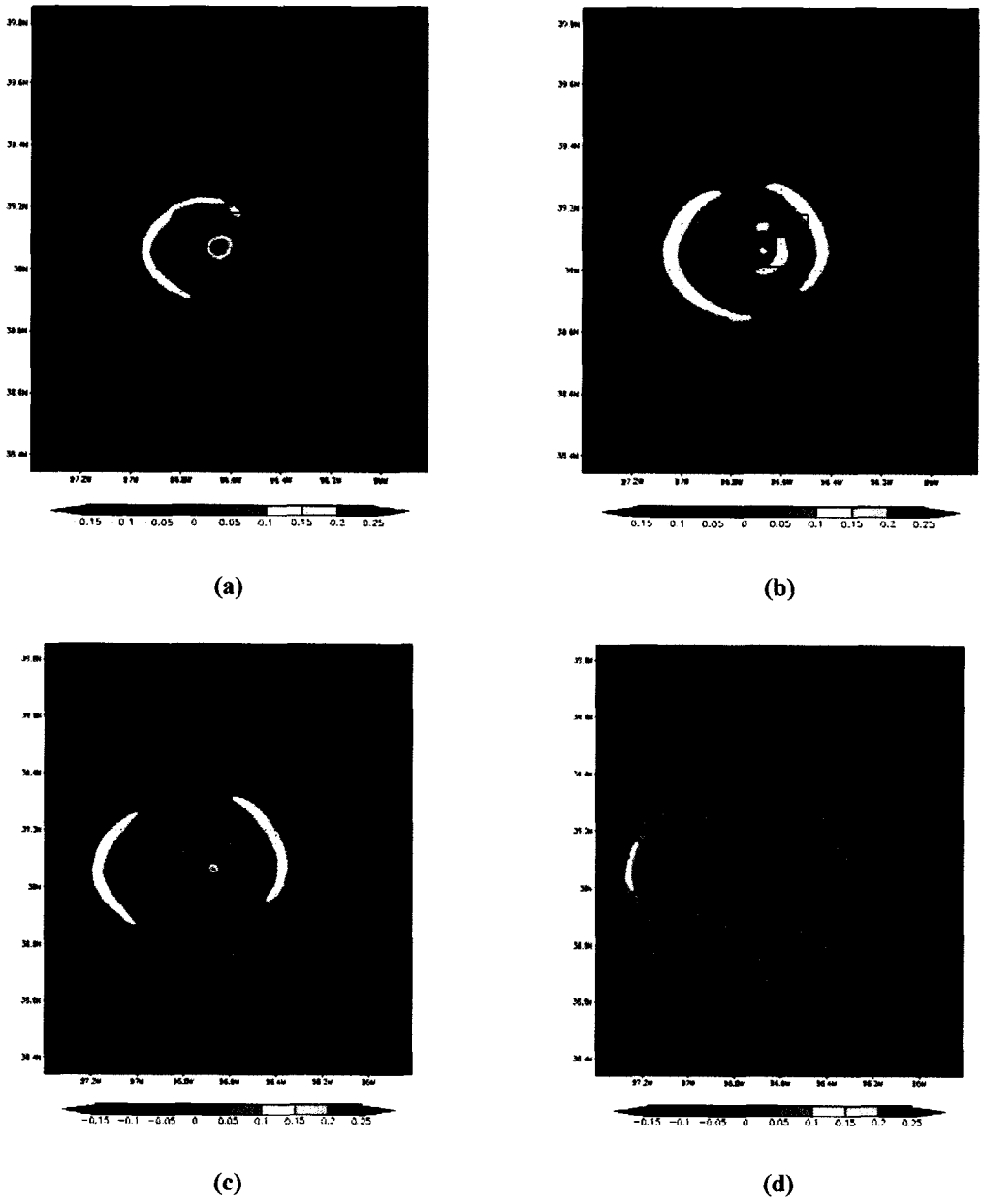

Figure 6.6 Vertical velocity at model level 12 (1990 m) in $m \cdot s^{-1}$ at (a) 1910 UTC, (b) 1920 UTC, (c) 1930 UTC, and (d) 1940 UTC.

Taking a horizontal slice along model level 12 (1990 m) of the vertical velocity field, displayed in Figure 6.6, shows the development of gravity waves over the horizontal domain due to the convection over the burn scar. Concentric regions of weak vertical motion radiating from the burn scar are apparent at 1910 UTC (Figure 6.6(a)),

Reproduced with permission of the copyright owner. Further reproduction prohibited without permission.

and expand in coverage over the next 30 minutes as seen in Figure 6.6 (b) through (d). Beres (2004) describes gravity waves induced by thermal forcing and the effects of wind flow on the pattern of vertical velocity associated with the induced gravity waves. In addition, Figure 6.6(d) shows that secondary cells of weak convection developed to the northwest and south of the initial region of upward motion. So, the burn scar not only induces convection over the scar region, but also induces perturbations in the atmosphere well away from the scar itself.

6.5 Cloud development

Cloud developed in the initial simulation was shown in section 4.2.6. Two levels of cloud developed in response to the upward motion generated over the burn scar. The lower level is centered near 1000 m and the upper level is centered near 2300 m. The first cloud level corresponds to the top of the region of the strongest gradient of upward motion seen in Figure 6.1, while the upper level of cloud is near the top of the same updraft associated with the burn scar as seen in the same figure.

Examining the evolution of the cloud field associated with the developing convection described in the previous section, Figure 6.7 shows the cloud field evolution at model level 13 (2292 m) for the times depicted for the vertical velocity field at model level 12 (1990 m) in Figure 6.6. Model level 12 shown in Figure 6.6 is near the base of the clouds shown in Figure 6.7.

Reproduced with permission of the copyright owner. Further reproduction prohibited without permission.

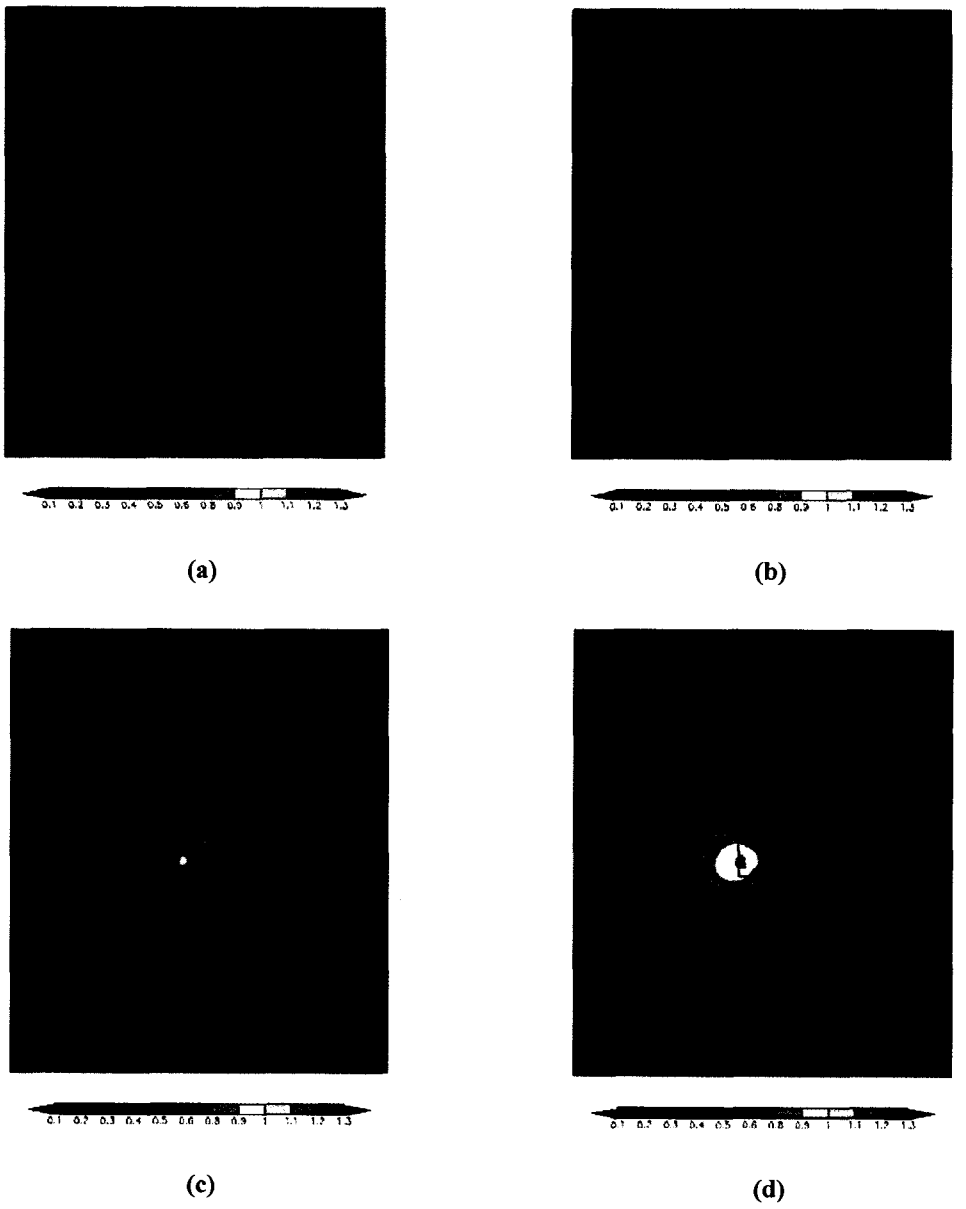

Figure 6.7 Cloud water at model level 13 (2292 m) in g·kg-1 at (a) 1910 UTC, (b) 1920 UTC, (c) 1930 UTC and (d) 1940 UTC. The burn scar location is outlined.

The cloud areas depicted in Figure 6.7 show great expansion over the 30 minutes included in the figure. The burn scar region outlined on each plot was completely covered by cloud during this period, showing that the updraft that developed over the scar provided sufficient lift to develop cloud, and the atmosphere was adequately stable to

Reproduced with permission of the copyright owner. Further reproduction prohibited without permission.

inhibit vertical development, and enhance the horizontal spreading of the cloud with time. The model sounding from 1900 UTC was presented in Figure 4.38 and shows drying near the level of the cloud tops (approximately 750 hPa) predicted in the simulation.

The cloud water fields presented in Figure 6.7 are relatively uniform with notches of lower concentrations developing with time to the northwest and south of the burn scar area. These regions correspond to areas of downward motion that develop in the vertical velocity field at model level 12 over the same time period as seen in Figure 6.6.

These thin layers of cloud that were predicted in the original simulation and discussed in this section show that the burn scar induced cloud, although these layers of cloud are relatively thin and would probably appear as stratocumulus to an observer. No precipitation was predicted from these clouds in this simulation, but the clouds were thick enough to influence the surface heat budget as was seen in Section 6.3.

The effects of cloud on the surface energy budget are apparent in the latent heat flux and sensible heat flux fields. Figure 4.14 shows the sensible heat flux at 1900 UTC in which a small region in the southwest portion of the burn scar has lower values than the surrounding area. This region is much smaller than the cloud area at 1850 UTC shown in Figure 4.32. By 2000 UTC, the sensible heat flux plot shown in Figure 4.15 demonstrates the effects of shading provided by the cloud shield that developed over the previous hour. The size of the effect of the cloud infers that there is a lag between the cloud formation and the influence on the sensible heat flux.

A similar, although not as widespread effect of the cloud field is seen in the latent heat flux field. At 2000 UTC, Figure 4.20 shows a region of lower values of latent heat flux to the west and south of the burn scar. The values over the burn scar itself show little

Reproduced with permission of the copyright owner. Further reproduction prohibited without permission.

change in value. The burn scar has lower soil moisture and more sparse vegetation than the surrounding environment, so little change would be expected in a region with such low initial values.

6.5.1 Effects of soil moisture

The sensitivity test discussed in the last chapter was run with no change in soil moisture, as opposed to the original simulation where the burn scar was made drier. Overall, the simulation with the more moist soil did show some differences, although subtle. The surface temperature and sensible heat flux showed little difference until the burn scar was covered in cloud for over an hour. Then higher values of surface temperature and sensible heat flux were seen over the burn scar with the higher soil moisture. The latent heat flux pattern shows some difference at 2000 UTC, with the contrast of soil moisture between the burn scar and the surrounding environment playing a larger role in determining the difference.

The strength of convection is greater initially in the simulation over the drier burn scar. With time, upward motion over the domain with uniform soil moisture increases and becomes significantly greater (0.8 m s^{-1} compared to 0.5 m s^{-1}) than over the drier burn scar by 2000 UTC. CAPE values were weak in both simulations with slightly weaker values over the burn scar in the uniform soil moisture simulation. The resulting cloud shows greater horizontal extent over the drier burn scar, but slightly greater concentrations in the more moist burn scar experiment with a thicker layer of cloud over the burn scar.

6.5.2 Effects of wind speed

Reproduced with permission of the copyright owner. Further reproduction prohibited without permission.

Using actual sounding winds had a large impact on microclimate changes. The stronger wind simulation showed decreased contrast in the surface temperature field between the burn scar and the surrounding environment with larger values from the burn scar being advected farther over the surrounding domain. The latent heat flux field showed an increase with the higher wind simulation, likely due to evaporation increasing due to the higher surface winds.

In the surface divergence field, values are weaker than seen in the original lighter wind simulation, and the patterns show greater displacement from the burn scar. As seen in the vertical velocity field, convection generated in the higher wind simulation is primarily over the surrounding environment rather than over the burn scar. Thus, enhancement of convection and any precipitation would occur over the less sensitive surrounding environment rather than over the burn scar itself.

The magnitude of vertical velocity evolves to be distinctly weaker in the high wind simulation. The vertical extent of upward and downward motion is greater in the high wind simulation than in the original simulation with the damped wind field.

6.6 Effects on Convective Cloud Development

Release of a warm, moist bubble was used to simulate a convective event interacting with the burn scar. The bubble, released over the region of greatest vertical velocity induced by the scar, produced an area of precipitation. In a related simulation, a bubble was also released in the same location over the undisturbed environment which also produced an area of precipitation. The details of both precipitation events were analyzed and show the distinct effects of the burn scar on both the dynamics and microphysics of the resulting convective cloud.

Reproduced with permission of the copyright owner. Further reproduction prohibited without permission.

The contrasts in the burn scar region and the surrounding environment induced convective development near the southwestern corner of the burn scar. This convection provided enough lift to develop a cloud over the region.

Contrast in surface characteristics have been associated with a number of different mesoscale circulations as discussed in Chapter 2. In this experiment, rather than distinct mesoscale circulations, a concentrated updraft region was accompanied by more diffuse downward motion. As the simulation progressed, gravity waves began developing in response to the disturbance initiated by the differential heating associated with the burn scar. The development of gravity waves due to thermal forcing has been described by Beres (2004).

6.6.1 Cloud Dynamics

The strength of the updraft associated with the convective cloud induced by the bubble was stronger and reached higher in the atmosphere in the burn scar simulation compared to the undisturbed surface simulation. This showed that the presence of the burn scar generated stronger convection. Clouds tops were higher over the burn scar, as were the cloud bases.

6.6.2 Cloud Microphysics

In general, the burn scar simulation resulted in greater mixing ratio values of cloud water, rain, graupel, and ice. The stronger convection associated with this simulation may have contributed to the higher concentration of the different water species

Reproduced with permission of the copyright owner. Further reproduction prohibited without permission.

seen over the burn scar. The details of the predicted graupel fields are presented in the next section.

Electrification Potential

The effects of a burn scar on electrification potential were evaluated using the two simulations in which a warm, moist bubble was released to simulate convection. The microphysical characteristics of the bubble experiment with the burn scar described in section 4.3.1 and the one without the burn scar presented in section 4.3.2 were both evaluated to determine the potential for lightning development and to distinguish which simulation had greater potential for lightning development.

Noninductive charging mechanism has been used to explain the development of charge separation in clouds leading to lightning discharge (Takahashi, 1978). Graupel plays an important role in this process and the presence of graupel affects charging within the cloud (Takahashi et al., 1999).

As mentioned previously, Takahashi et al. (1999) concluded that graupel number concentrations greater than 1 L^{-1} (1000 m^{-3}) were associated with the development of lightning. They also found the greatest charging took place near -20°C.

In Chapter 4, both the mixing ratio and number concentration of graupel were examined to evaluate the effect of the burn scar on the potential charging of a storm. In section 4.3.2, the graupel field predicted in the burn and no burn simulations were examined side by side to evaluate the effect of the burn scar. Figures 4.77 through 4.79 show the graupel number concentrations for the time in which the values were significant for cloud electrification. These figures showed that the burn scar simulation predicted a larger area of graupel with significant concentrations to facilitate charging and initiate

Reproduced with permission of the copyright owner. Further reproduction prohibited without permission.

lightning. Also, the burn scar simulation produced graupel at higher levels of the cloud, closer to the -20°C level, implying that even greater charging would occur in the cloud over the burn scar.

Therefore, greater and more widespread lightning activity could be induced by the burn scar. Knowles (1993) hypothesized that increased convection over a burn scar would result in greater lightning activity and the potential for increased fire activity. Fire ignition depends on an ignition mechanism, the presence of fuels susceptible to burning and the amount of precipitation that accompanies the lightning in the storm. The presence of fuels to burn would depend on the location of the developing storm to the burn scar. In this simulation, the main convection is in the southwest corner of the burn scar, which has little vegetation left to burn. However, fuels in the surrounding environment could be affected by the developing storm and subjected to lightning ignition. In storms with heavy precipitation and lightning, there is greater likelihood that the accompanying precipitation will extinguish the fire ignited by the lightning before significant spread can occur. The effects of the burn scar on precipitation amount and distribution is discussed in the next section.

Mölders and Kramm (2007) found a lowering in graupel mixing ratio, but a longer time period that graupel was present in the clouds in the simulations with the presence of burn scars. Areas of increased graupel mixing ratio were predicted away from the burn scar regions in the domain.

6.6.3 Precipitation Patterns

Precipitation was not generated in the simulations with only the burn scar as a forcing mechanism. Subsequent simulations with the introduction of a warm, moist

Reproduced with permission of the copyright owner. Further reproduction prohibited without permission.

bubble to induce convection did produce measurable amounts of precipitation. The bubble experiments were conducted both over the domain with the burn scar and that with an undisturbed environment. In both cases, precipitation developed within the convection induced by the bubble. The burn scar simulation had higher values and more widespread coverage of precipitation than the simulation over the undisturbed environment. The burn scar simulation also showed a 17% increase in precipitation due to the presence of the scar. Also, timing of the precipitation was very similar, but the amount of rain that fell over the burn scar was greater than over the undisturbed environment, therefore the intensity of the precipitation was greater over the burn scar. Other model studies have also predicted increased precipitation in the presence of fire scars. These studies include (Knowles, 1993; Chen et al., 2001; Mölders and Kramm, 2007).

Extending these results to the flooding potential of the area is a matter of looking at how the burn scar both affects the amount of precipitation that falls and how the modification of the vegetation and the surface by the fire change the response of the burn scar region to a precipitation event. As has just been discussed, and increase of 17% in the amount of precipitation was seen in the burn scar simulation. The simulated precipitation event also had greater intensity than seen in the unmodified environment experiment. As discussed in Chapter 2, DeBano (2000) described how decreased vegetation and the development of hydrophobic soil conditions increase the amount of surface runoff in response to precipitation events and thus the potential for flooding and erosion. The results of this study support that the burn scar, already more susceptible to

Reproduced with permission of the copyright owner. Further reproduction prohibited without permission.

flooding and erosion, can also enhance the amount of precipitation over this sensitive area.

As discussed in the previous section, microphysical changes in the resulting cloud over the burn scar had increased graupel number concentrations, implying the cloud has the potential to develop greater changing that would result in greater lightning activity. While increased lightning activity might result in ignition of new fires, the increased precipitation seen from the same storm could inhibit both ignitions by lightning and spread of those fires that did ignite.

Reproduced with permission of the copyright owner. Further reproduction prohibited without permission.

Chapter 7

Conclusions and Recommendations for Future Research

7.1 Introduction

This work investigated the effects of a hypothetical wildfire burn scar on the microclimate of the scar and its surrounding environment. In addition to the effects of the scar itself in the domain, further investigation was extended to effects of the burn scar presence on the development of convection due to outside forcing. In the case of this investigation, a warm, moist bubble was released over the burn scar region to simulate convection.

7.2 The major findings of this study are:

Effects on microclimate

The parameters examined show that the burn scar area in the simulation experienced greater surface heating. As shown in Chapter 4, both the sensible heat flux field and the surface temperature analysis indicated a significant increase over the burn scar region compared to the surrounding environment.

Effects on convective development

The heterogeneous heating over the domain resulted in development of a relatively strong updraft (up to 1 $m \cdot s^{-1}$) over the scar. Two layers of cloud developed in response to the updraft. The clouds that developed over the burn scar did not produce

Reproduced with permission of the copyright owner. Further reproduction prohibited without permission.

precipitation. However, the release of a warm, moist bubble in the region of the strongest vertical velocity showed enhancement of both convection and precipitation. The presence of the burn scar therefore enhanced precipitation from a storm developing over the scar.

Cloud electrification

The presence of a burn scar affected the number concentration of graupel in the storm and thus increased the potential for lightning development from the cloud induced by the warm moist bubble. Increased lightning activity could result in new lightning ignited fires in the vicinity of the convection.

Sensitivity to soil moisture

Only subtle changes were predicted in the surface energy budget terms between the uniform soil moisture experiment and the original experiment with a drier burn scar. Resulting cloud had greater depth over the more moist burn scar, but more widespread horizontal extent over the drier burn scar.

Sensitivity to winds

The simulation was very sensitive to wind speed. The contrast in surface temperature between the burn scar and surrounding environment decreased with the higher initialized winds. However, the latent heat flux increased with the stronger winds. The vertical velocity field that developed in response to burn scar in the higher wind simulation was weaker, and displaced away from the scar itself.

7.3 Future Research

Reproduced with permission of the copyright owner. Further reproduction prohibited without permission.

This project has great potential for expansion to many different aspects of mesoscale meteorology and hydrology.

- **Stability**. The sounding used in this study was relatively stable. While this sounding was selected to help isolate the effects of changes in surface forcing, future studies could explore the effects of the burn scar on more convectively unstable atmospheric conditions.
- **Burn scar heterogeneity**. To isolate impacts of burn scar, this study examined homogeneous severe burn characteristics. Wildfire burn scars typically exhibit variations in soil and vegetation alteration by the fire. Future studies could investigate the non-uniform burn characteristics of a specific fire. These characteristics could include variations in burn severity, vegetation reduction, and burn shape.
- **Induced convection characteristics**. This study used one warm bubble to simulate the development of externally forced convection. Random convection could be investigated by releasing random bubbles over the domain and examining the strength of the individual cells as well as the effect of the burn scar on convective organization.
- **Age of burn scar**. Observational studies have reported that the strength of microclimate differences over burn scars decreases with time as the burn scar characteristics age and vegetation begins to grow in the scar area. Future studies could simulate burn scar aging to test the changes in magnitude of burn scar effects on microclimate and precipitation with time.

Reproduced with permission of the copyright owner. Further reproduction prohibited without permission.

- **Particulate ejected by wildfire.** Other opportunities exist to study more immediate effects of wildfire on the atmosphere and cloud and precipitation development as particulate matter is ejected into the atmosphere by the fire.
- **Dry sounding.** In some ways, the investigation of the microclimate of the burn scar region was inhibited by the cloud that formed over the scar. While the development of cloud was a major part of the study, the shading of the cloud limited the examination of the effects of heating of the burn scar on the microclimate. Additional studies could be made with drier soundings in which strong solar heating occurred.
- **Soil moisture changes.** Future research could concentrate on larger contrasts in soil moisture and evaluating the effects on the surface energy budget. Soil moisture contrast changes could also be combined with further experiments in convective development and testing drier soundings.
- **Hydrologic response.** An extension of this work could be to couple the output from RAMS as input to a hydrologic model to investigate the resulting effects seen in precipitation amount and coverage on the surface hydrology of the basin and potentially the effects on the magnitude of flooding due to the presence of the burn scar.

Reproduced with permission of the copyright owner. Further reproduction prohibited without permission.

Chapter 8

References

Amiro, B. D., J. I. MacPherson, and R. L. Desjardins, 1999: BOREAS flight measurements of forest-fire effects on carbon dioxide and energy fluxes. *Agric. For. Meteorol.*, **96,** 199–208.

Anthes, R. A., 1984: Enhancement of convective precipitation by mesoscale variations in vegetative covering in semiarid regions, *J. Clim. Appl. Meteorol.*, **23,** 541–554.

Avissar, R., and Y. Liu, 1996: Three-dimensional numerical study of shallow convective clouds and precipitation induced by land surface forcing, *J. Geophys. Res.*, **101,** 7499–7518.

Avissar, R., and T. Schmidt, 1998: An evaluation of the scale at which ground-surface heat flux patchiness affects the convective boundary layer using large-eddy simulations, *J. Atmos. Sci.*, **55,** 2666–2689.

Beres, J. H., 2004: Gravity wave generation by three-dimensional thermal forcing. *J. Atmos. Sci.*, **61,** 1805–1815.

Reproduced with permission of the copyright owner. Further reproduction prohibited without permission.

Cannon, S. H., E. R. Bigio, and E. Mine, 2001: A process for fire-related debris flow initiation, Cerro Grande fire, New Mexico. *Hydrol. Processes,* **15,** 3011–3023.

Campbell G. S., J. D. Jungbauer, Jr, K. L. Bristow, R. D. Hungerford, 1995: Soil temperature and water content beneath a surface fire. *Soil. Sci.,* **159**, 363–374.

Certini, G., 2005: Effects of fire on properties of forest soils: a review. *Oecologia,* **143**, 1–10.

Chambers, S. D., J. Beringer, J. T. Randerson, and F. S. Chapin III, 2005: Fire effects on net radiation and energy partitioning: Contrasting responses of tundra and boreal forest ecosystems, *J. Geophys. Res.,* **110**, 106.

Chambers, S. D., and F. S. Chapin III, 2003: Fire effects on surface-atmosphere energy exchange in Alaskan black spruce ecosystems: Implications for feedbacks to regional climate, *J. Geophys. Res.,* **108,** 8145.

Chandler, C., P. Cheney, P. Thomas, L. Trabaud, D. Williams, 1983: *Fire in forestry, Forest fire behaviour and effects, Vol. 1,* Wiley, New York (450pp.).

Reproduced with permission of the copyright owner. Further reproduction prohibited without permission.

Chen, F., T. T. Warner, and K. Manning, 2001: Sensitivity of orographic moist convection to landscape variability: A study of the Buffalo Creek, Colorado, flash flood case of 1996. *J. Atmos. Sci.*, **58,** 3204–3223.

Chen, F., and R. Avissar, 1994: Impact of land-surface moisture variabilities on local shallow convective cumulus and precipitation in large-scale models, *J. Appl. Meteorol.*, *33*, 1382–1394,

Cotton, W. R., R. A. Pielke Sr., R. L. Walko, G. E. Liston, C. J. Tremback, H. Jiang, R. L. McAnelly, J. Y. Harrington, M. E. Nicholls, G. G. Carriol, and J. P. McFadden, 2003: RAMS 2001: Current status and future directions. *Meteorol. Atmos. Phys.*, **82**, 5–29

DeBano, L.F., 2000: The role of fire and soil heating on water repellence in wildland environments: a review. *J. Hydrol.* **231**,195– 206

Harrington, J.Y., 1997: The effects of radiative and microphysical processes on simulated warm and transition season Arctic stratus. Ph. D. Dissertation. Atmospheric Science Paper No 637, Colorado State University, Department of Atmospheric Science, Fort Collins, CO 80523, 289 pp.

Hill, G. E., 1974: Factors controlling the size and spacing of cumulus clouds as revealed by numerical experiments. *J. Atmos. Sci.*, **31,** 646-673.

Reproduced with permission of the copyright owner. Further reproduction prohibited without permission.

Holton, J. R., 1992: An *Introduction to Dynamic Meteorology, 3rd Edition.* Academic Press, San Diego, CA, 511 pp.

Johansen, M. P., T. E. Hakonson, and D. D. Breshears, 2001: Post-fire runoff and erosion from rainfall simulation: contrasting forests with shrublands and grasslands. Hydrol. Processes, 15, 2953–2965.

Kansas State University, Konza Prairie Long Term Ecological Research Program website (http://www.k-state.edu/konza/location.htm)

Klemp, J. B. and R. B. Wilhelmson, 1978: The simulation of three-dimensional convective storm dynamics. *J. Atmos. Sci.*, **35**, 1070–1096.

Knowles, J. B., 1993: The influence of forest fire induced albedo differences on the generation of mesoscale circulations. M.S. Thesis. Department of Atmospheric Science, Colorado State University, 86 pp.

Lilly, D. K., 1962: On the numerical simulation of buoyant convection. *Tellus*, **14**, 148–172.

Reproduced with permission of the copyright owner. Further reproduction prohibited without permission.

Liu, H., J. T. Randerson, J. Lindfors, and F. S. Chapin III, 2005: Changes in the surface energy budget after fire in boreal ecosystems of interior Alaska: An annual perspective. *J. Geophys. Res.,* **110,** 101-110.

Mahfouf, J.-F., E. Richard, and P. Mascart, 1987: The influence of soil and vegetation on the development of mesoscale circulations. *J. Clim. Appl. Meteorol.*, **26,** 1483–1495.

Mahrer, Y., and R. A. Pielke, Sr., 1978: The meteorological effect of the changes in surface albedo and moisture. *Isr. Meteorol. Res., Pap*, **2,** 55-70.

Marshall, C. H., R. A. Pielke, Sr., L. T. Steyaert, D. A. Willard, 2004: The impact of anthropogenic land-cover change on the Florida peninsula sea breezes and warm season sensible weather. *Mon. Wea. Rev.,* **132,** 28-52.

Mölders, N., and G. Kramm, 2007: Influence of wildfire induced land-cover changes on clouds and precipitation in Interior Alaska – A case study. *Atmos. Res.,* **84,** 142-168.

Oke, T. R., 1987: *Boundary layer climates, 2nd Edition.* Routledge, London, 435 pp.

Reproduced with permission of the copyright owner. Further reproduction prohibited without permission.

Ookouchi, Y., M. Segal, R. C. Kessler, and R. A. Pielke, 1984: Evaluation of soil moisture effects on the generation and modification of mesoscale circulations. *Mon. Wea. Rev.*, **112,** 2281–2292.

Pielke, R.A. Sr., J. Adegoke, A. Beltran-Przekurat, C.A. Hiemstra, J. Lin, U.S. Nair, D. Niyogi, and T.E. Nobis, 2006: An overview of regional land use and land cover impacts on rainfall. *Tellus B*, submitted.

Pielke, R. A., 2002 Pielke, R. A., Sr. *Mesoscale meteorological modeling, 2nd Edition*, Academic Press, San Diego, CA, 676 pp.

Pielke, R. A., 2001: Influence of the spatial distribution of vegetation and soils on the prediction of cumulus convective rainfall. *Reviews of Geophysics*, **39**, 151–177.

Pielke, R. A., W. R. Cotton, R. L. Walko, C. J. Tremback, W. A. Lyons, L. D. Grasso, M. E. Nicholls, M. D. Moran, D. A. Wesley, T. J. Lee, and J. H. Copeland, 1992: A comprehensive meteorological modeling system – RAMS. *Meteor. Atmos. Phys.*, **49,** 69-91.

Rozoff, C. M., 2002: Personal communication.

Rozoff, C. M., W. R. Cotton, and J. O. Adegoke, 2003: Simulation of St. Louis, Missouri, land use impacts on thunderstorms. *J. Appl. Met.*, **42**, 716-738.

Reproduced with permission of the copyright owner. Further reproduction prohibited without permission.

Saleeby, S. M. and W. R. Cotton, 2004: A large-droplet mode and prognostic number concentration of cloud droplets in the Colorado State University Regional Atmospheric Modeling System (RAMS). Part I: Module descriptions and supercell test simulations. *J. Appl. Met.*, **43**, 182-195.

Schreiber, W. E., 1986: Case studies of thunderstorms initiated by radar-observed convergence lines. *Mon. Wea. Rev.*, **114,** 2256-2266.

Segal M., J. F. W. Purdom, J. L. Song, R. A. Pielke, Sr., Y. Mahrer, 1986: Evaluation of cloud shading effects on the generation and modification of mesoscale circulations. *Mon. Wea. Rev.*, **114**, 1201-1212

Segal, M., and R. W. Arritt, 1992: Non-classical mesoscale circulations caused by surface sensible heat-flux gradients, *Bull. Am. Meteorol. Soc.*, **73,** 1593–1604.

Segal, M., R. Avissar, M. C. McCumber, and R. A. Pielke, 1988: Evaluation of vegetation effects on the generation and modification of mesoscale circulations, *J. Atmos. Sci.*, **45,** 2268–2292.

Smagorinsky, J., 1963: General circulation experiments with the primitive equations. Part I: The basic experiment. *Mon. Wea. Rev.*, **91,** 99–164.

Reproduced with permission of the copyright owner. Further reproduction prohibited without permission.

Stull, R. B., 1988: *An introduction to boundary layer meteorology.* Kluwer Academic Publishers, Dordrecht, The Netherlands, 666 pp.

Takahashi, T., 1978: Riming electrification as a charge generation mechanism in thunderstorms. *J. Atmos. Sci.,* **35,** 1536–1548.

Takahashi, T. T. Tajiri, and Y. Sonoi, 1999: Charges on graupel and snow crystals and the electrical structure of winter thunderstorms. *J. Atmos. Sci.*, **56**, 1561–1578.

Tzivion S., G. Feingold, Z. Levin, 1987: An efficient numerical solution to the stochastic collection equation. *J. Atmos. Sci.*, **44**, 3139–3149.

Ulery, A. L., and R. C. Graham, 1993: Forest fire effects on soil color and texture. *Soil. Sci. Soc. Am. J.,* **57**, 135–140.

Underwood, S. J., and M. D. Schultz, 2004: Patterns of cloud-to-ground lightning and convective rainfall associated with postwildfire flash floods and debris flows in complex terrain of the western United States. *J. Hydromet.*, **5,** 989-1003.

van den Heever, S. C., 2001: The impact of several hail parameters on simulated supercell storms. Ph. D. Dissertation. Atmospheric Science Paper No 711, Colorado State University, Department of Atmospheric Science, Fort Collins, CO 80523, 265 pp.

Reproduced with permission of the copyright owner. Further reproduction prohibited without permission.

Vidale, P. L., R .A. Pielke, A. Barr, and L. T. Steyaert, 1997. Case study modeling of turbulent and mesoscale fluxes over the BOREAS region. *J. Geophys. Res.*, **102**, 29167-29188.

Walko R. L., L. E. Band, J. Baron, T. G. F. Kittel, R. Lammers, T. J. Lee, D. Ojima, R. A. Pielke, Sr, C. Taylor, C. Tague, C. J. Tremback, P. L. Vidale, 2000: Coupled atmosphere-biophysics-hydrology models for environmental modeling. *J. Appl. Meteor.* **39**, 931–944.

Wilson, J. W., and W. E. Schreiber, 1986: Initiation of convective storms at radar-observed boundary layer convergence lines. *Mon. Wea. Rev.*, **114,** 2515-2536.

Yates, D. N., T. T. Warner, E. A. Brandes, J. Sun, C. K. Mueller, and G. H. Leavesley, 2000: Prediction of a flash flood in complex terrain: A comparison of flood discharge simulations using rainfall input from radar, a dynamic model, and an automated-algorithmic system. *J. Hydrol. Eng.*, **6,** 265–274.

Reproduced with permission of the copyright owner. Further reproduction prohibited without permission.